NASA Contractor Report 3899

Calculation of Steady and Unsteady Airfoil Flow Fields Via the Navier-Stokes Equations

Stephen J. Shamroth

CONTRACT NAS1-15214
AUGUST 1985

NASA

NASA Contractor Report 3899

Calculation of Steady and Unsteady Airfoil Flow Fields Via the Navier-Stokes Equations

Stephen J. Shamroth
Scientific Research Associates, Inc.
Glastonbury, Connecticut

Prepared for
Langley Research Center
under Contract NAS1-15214

NASA
National Aeronautics
and Space Administration

Scientific and Technical
Information Branch

1985

TABLE OF CONTENTS

LIST OF SYMBOLS

a_1, a_2	-	Grid generation parameters
C_1, C_2, C_μ	-	Turbulence model parameters
C_p	-	Specific heat
D	-	Sublayer damping factor
k	-	Turbulence energy
ℓ	-	Mixing length
p	-	Pressure
R	-	Gas constant
u, v	-	Velocity components
x, y	-	Cartesian coordinates
α	-	Incidence angle
δ	-	Boundary layer thickness
ε	-	Turbulence dissipation
μ	-	Viscosity
ν	-	Kinematic viscosity
ξ, η	-	Computational coordinates
ρ	-	Density
τ	-	Time
τ_{ij}	-	Shear Stress
ω	-	Frequency

INTRODUCTION

Recent advances in both computer hardware and numerical techniques have led to a significant broadening of the practical choices available for analyzing a wide variety of viscous flow problems. Prior to recent computational advances, most predictive techniques were confined to inviscid flow analyses possibly combined with boundary layer corrections. More recently efforts have focused upon more complex flows which were not necessarily suited to boundary layer type analyses. One important problem of this type is the two-dimensional isolated airfoil flow field problem.

The two-dimensional isolated airfoil flow field presents a problem which has long been of practical interest. The accurate knowledge of airfoil lift, drag and moment coefficients under a range of steady and unsteady operating conditions is required in assessing the airfoil performance. In the general case the airfoil flow field presents complex phenomena even when three dimensional effects are neglected. This problem contains viscous regions which are laminar, transitional and turbulent, may exhibit extremely strong favorable and adverse pressure gradients, may contain multiple regions of large separation as well as shed vortices and exhibit important unsteady flow characteristics. A particularly complex airfoil flow field occurs in the helicopter rotor which may periodically undergo dynamic stall. Dynamic stall differs from its static counterpart in two major ways. First of all, the maximum lift obtainable under dynamic conditions is greater than that under static conditions. Secondly, though under static conditions lift and moment are uniquely related to incidence, under dynamic stall conditions the flow depends upon the time history of motion and the lift and moment coefficients have hysteresis loops associated with them. As the helicopter blade travels through the rotor disc, the blade experiences a varying incidence angle. Over most of the disc the blade will be unstalled (i.e., the flow will not contain any large separated regions leading to a decrease in blade lift or a generation of large blade moment coefficients); however, over a portion of the disc large regions of separated flow may appear and over these regions the blade performance will deteriorate. This time history dependence of the problem makes dynamic stall prediction a particularly difficult task. Typical experimental investigations of this complex phenomenon are discussed in Refs. 1-8.

In regard to predictive procedures for airfoils in both steady and unsteady flow, airfoils at low incidence are expected to have small viscous displacement effects. In these cases accurate predictions of airfoil pressure distributions can be obtained from an inviscid flow calculation without consideration of viscous boundary layer effects. If a boundary layer growth prediction is desired, the inviscid analysis can be combined in a non-interactive mode with a boundary layer analysis (e.g. Refs. 9 and 10) to predict both the pressure distribution and boundary layer development. The non-interactive inviscid flow-boundary layer calculation can give accurate predictions as long as viscous displacement effects are small and can even be used when limited regions of local separated flow are present (Ref. 11). However, for those cases in which viscous displacement effects significantly alter the inviscid pressure distribution, an alternate procedure is required.

For the airfoil flow field problem significant viscous displacement effects are most pronounced in flows having regions of significant separation. In the presence of significant separation, the observed pressure distribution will differ considerably from that predicted from inviscid flow considerations. The actual pressure distribution corresponds to that around a body equivalent in shape to the airfoil plus a displacement correction (for viscous displacement effects), and in the presence of large separated regions the displacement correction is not small. In such cases an anlysis which is more complete than a purely inviscid analysis is required. One possibility for solving the separated airfoil flow field problem is the boundary layer strong interaction approach. In this approach an inviscid analysis and a boundary layer type analysis are solved so that the viscous displacement effects resulting from boundary layer growth influence the inviscid pressure distribution. Although this approach can give good results for some cases, it does have certain drawbacks. Usually, the approach requires an iteration between the two solutions and in the case of subsonic flow the iteration is a global one; e.g., the inviscid analysis is solved for a given displacement surface. The inviscid pressure distribution is then imposed upon the boundary layer equations and these equations are solved to predict the boundary layer development including a new displacement surface and the process is repeated until convergence occurs. This iteration process may be

difficult to converge under some circumstances, for example when large regions of separation occur or when the flow is transonic. Furthermore, assumptions may be required to treat the boundary layer equations in separated regions and normal pressure gradients must be assumed negligible in the viscous flow region. The approximations required in separated regions and the neglect of transverse pressure gradients in the regions where viscous effects are important may lead to serious inaccuracies for flow containing significant regions of separation. The drawbacks associated with boundary layer strong interaction techniques have led some investigators to seek an alternate means of predicting airfoil flow fields which solve the entire flow via a single set of viscous flow equations.

Two general types of analyses which solve the viscous flow equations throughout the entire region of interest are in current use. These are the so-called 'thin-shear layer' analysis and the Navier-Stokes analysis. The thin shear layer equations are an approximate form of the Navier-Stokes equations which contain all pressure and convective terms, but retain only some viscous terms. The viscous terms retained are those appropriate for a thin shear layer flow in which the shear layer is aligned with one of the computational coordinate directions. Use of the thin shear layer equations allows simultaneous calculation of pressure distribution and viscous and heat transfer effects without resorting to an interaction analysis and as such may be a valid approach for certain flow cases. However, since only part of the stress tensor is retained, the equations omit important terms for flows in which the streamlines vary significantly from computational coordinate lines such as in the case of flow separation. Although the thin shear layer equations are solved in less CPU time than are the Navier-Stokes equations, the saving is usually not more than twenty per cent. Therefore, thin shear layer equations do not have any major computer run time advantage over the full Navier-Stokes solution. Since one major item of interest in the present study focuses upon airfoils with significant regions of flow separation, only Navier-Stokes analyses shall be considered in the present discussions.

The initial airfoil analyses based upon the Navier-Stokes equations considered incompressible laminar flow. Early examples are those of Mehta and Lavan (Ref. 12) and Lugt and Haussling (Ref. 13). Mehta and Lavan solved

a stream function vorticity formulation of the laminar incompressible Navier-Stokes equations to predict flow about an impulsively started airfoil and Lugt and Haussling utilized an incompressible stream function-vorticity approach to investigate flow about an abruptly started elliptical cylinder. More recent incompressible stream function-vorticity analyses have focused upon various aspects of the airfoil flow field problem. For example, Mehta (Ref. 14) used a numerical scheme considerably more efficient than that of Ref. 12 to solve incompressible laminar flow about an airfoil oscillating through incidence regimes in which stall occurs. Wu and Sampath (Ref. 15) and Wu, Sampath and Sankar (Ref. 16) applied the Wu-Thompson integro-differential formulation (Ref. 17) to both the impulsively started airfoil and the oscillating airfoil problem. In a similar vein Kinney and Cielak (Refs. 18 and 19) have investigated unsteady airfoil flow fields and Lugt and Haussling (Ref. 20) have investigated the time scale required to establish the Joukowski condition in incompressible flow. Finally, Thompson and his coworkers (e.g. Ref. 21) have calculated the flow about a variety of airfoil shapes and Hodge and Stone (Ref. 22) have investigated stalled airfoils using an incompressible primitive variable approach.

Other investigations have considered compressible airfoil flow fields. Verhoff (Ref. 23) applied MacCormack's fully explicit method (Ref. 24) to the airfoil problem; however, since the procedure is fully explicit, a small time step is necessary to maintain numerical stability as a result of the locally refined mesh in the boundary layer and long computer run times result. In this regard conditionally stable schemes such as fully explicit schemes are not an optimum choice when mesh refinement is required for boundary layer definition; in these schemes the maximum allowable time step size is limited by the spatial step size leading to large run times. The time-step limitation problem, which is severe even in laminar flows, is magnified considerably in turbulent flows where a much finer spatial resolution is required in the boundary layer. On the other hand, unconditionally stable schemes (in a linear sense) such as some of the implicit schemes do not suffer from this characteristic. Both Deiwert's (Ref. 25) and Levy's (Ref. 26) analyses are based upon MacCormack's hybrid implicit-explicit-characteristics scheme (Ref. 27). By virtue of an enlarged stability bound this new procedure is more efficient than the original MacCormack procedure

(Ref. 24) for airfoil calculations; however, it does present formidable coding problems. Implicit schemes, although more complicated to code than explicit schemes, do not present the formidable coding problems associated with the hybrid scheme. An implicit solution of the full Navier-Stokes equations has been developed by Gibeling, Shamroth and Eiseman (Ref. 28) who applied the Briley-McDonald (Ref. 29) numerical technique to the airfoil flow field. A similar approach has since been used by Sankar and Tassa (Ref. 30) to study an oscillating airfoil in a compressible low Reynolds number fluid. El Refaee, Wu and Likoudis (Ref. 31) have extended the integral approach of Wu and his associates (Refs. 15 and 16) to compressible flow. In another approach Steger (Ref. 32) used the thin shear layer equations in conjunction with the coordinate generation procedure of Thompson, Thames and Mastin (Ref. 33) to predict laminar flow about an airfoil.

As expected most of the Navier-Stokes airfoil analyses were applied to laminar flow before turbulent flow calculations were attempted. In extending these analyses to the turbulent regime, several factors must be considered. Since turbulent flow requires considerably more resolution in the viscous wall boundary layer region than does laminar flow, a turbulent calculation requires very high near wall resolution and this high near wall resolution makes explicit procedures with their associated stability limits impractical. A second point concerns turbulence modelling. In general the airfoil flow field presents a very difficult turbulence modelling problem. The flow field contains regions of laminar, transitional and turbulent flow as well as significant separation regions. In cases where the flow is unsteady, shed vortices may be present. In general a turbulence energy model which includes a transition capability is required to analyze turbulent airfoil flow fields. However, useful information can also be gained by using a simpler model such as a mixing length model throughout.

An early application to the airfoil turbulent flow problem was carried out by Shamroth and Gibeling (Ref. 34). The method was applied in Ref. 34 to airfoils at modest incidence. In addition it was applied to airfoils in stall by Shamroth and Gibeling (Ref. 35) and airfoils pitching at low incidence by Shamroth (Ref. 36). Other turbulent analyses are those of Tassa and Sankar (Ref. 37) and Sankar and Tang (Ref. 38) who studied a turbulent airfoil undergoing dynamic stall using an algebraic mixing length model.

The present report describes a work effort aimed at the turbulent airfoil flow field and contains results for a variety of steady and unsteady flow situations. Some of these have been previously reported in the open literature (Refs. 35 and 36), however, since the calculations presented in Refs. 35 and 36 were supported under the present contract, the results are repeated here.

ANALYSIS

The Coordinate System

The presence of bounding surfaces of a computational domain which do not fall upon coordinate lines presents significant difficulties for numerical techniques which solve the Navier-Stokes equations. If a bounding surface (such as the airfoil surface) does not coincide with a coordinate line, serious numerical errors may arise in the application of boundary conditions and considerable effort may be required to reduce these errors to an acceptable level. Although this problem arises in both viscous and inviscid flows, it is more severe in viscous flows where no-slip conditions on solid walls can combine with boundary condition truncation error to produce numerical solutions which are both qualitatively and quantitatively in error. Thus coordinate systems are sought in which each no-slip surface of the specific problem falls on a coordinate line. Such a system is termed a body-fitted coordinate system. Several approaches are available to form a body-fitted coordinate system. Among the coordinate system candidates are conformal coordinate systems such as that used by Mehta (Ref. 14), systems based upon solution of a Poisson equation such as those developed by Thompson and his coworkers (e.g., Ref. 33) or Haussling (Ref. 39) and a constructive system.

The approach used in the present effort is a constructive approach in which the required airfoil is by defintion a coordinate line and in which grid point placement is specified by the user. The procedure was developed originally for the isolated airfoil problem by Gibeling, Shamroth and Eiseman (Ref. 28) and explained in general terms by Eiseman (Ref. 40). The coordinate system generated by the constructive process has several advantages. The system allows packing of grid points in regions where high grid resolution is required. In general, the high resolution regions are required near the airfoil surface (where the boundary layer is found) and in the vicinity of the airfoil leading edge where rapid streamwise changes are present. In addition, although the grid has a branch cut emanating from the airfoil trailing edge, metric data are continuous across the branch cut. Furthermore, although the grid is nonorthogonal, the amount of nonorthogonality is not large. Finally, as applied to the airfoil problem

the metric data remain smooth from grid point to grid point. A computer generated plot of the airfoil coordinate system is given in Fig. 1 where for clarity not all lines are shown. The actual grid used has very high resolution near the surface where the transverse grid spacing is of the order of 10^{-5} chords and near the leading edge where the streamwise grid spacing is of the order of 10^{-3} chords.

The coordinate system consists of a set of two families of curves; the ξ = constant curves such as line HI in Fig. 1 and the η = constant curves such as ABCD or A'ED' in Fig. 1. The coordinate system is constructed by first forming the inner loop A'ED' which includes the airfoil. The airfoil may be either specified by an analytic equation or by discrete data points. If an equation is used, then construction of the inner loop is straight-forward. If the airfoil is specified by discrete data points, then, in general, the points required on the inner loop will not coincide with any point used for airfoil specification. In this case, a curve fit is used to obtain the required inner loop points. The curve fit used is based upon a local parabolic fit. For any given point required on the inner loop, a parabola is fit through three adjacent specifying points, two on the right and one on the left. A second parabola is then fit through the two points on the left and one on the right. The location of the required point is obtained via a weighted average of these curve fits with the weighting factor being determined by the distance from the required point to the center specifying point of each parabola. Alternatively the airfoil may be fit in a piecewise manner through a least squares polynominal constrained to maintain continuous first and second derivatives at joining points.

This is followed by constructing an outer loop ABCD which consists of line segments AB and CD at a specified distance from the airfoil chord line and a frontal curve BC. Both the inner and outer loops are then represented by parametric curves

$$x = x(s), \qquad y = y(s) \tag{1}$$

where the parameter varies from zero to unity. The present coordinate generation process utilizes a multi-part transformation. First x and y are expressed as a function of s', the physical distance along the curve. Then

s' is related to s via a hyperbolic tangent parameterization centered about the leading edge for the inner loop and a cubic polynomial representation for the outer loop. The inner loop transformation parametric representation is chosen so as to have rapid variation in the airfoil leading edge region. Both the inner loop hyperbolic tangent transformation and the outer loop cubic transformation are applied between s'/2 and 0 and between s'/2 and s' on each loop. This ensures that corresponding points on the branch cut will be equi-distant in s from the branch cut end points, points A' and D'. This property is required if corresponding branch cut points are to fall on the same pseudo-radial line.

Having specified loop 1, the inner loop, and loop 4, the outer loop, the construction process now specifies loop 2 and loop 3. Both loop 2 and loop 3 are located between loop 1 and loop 4 with loop 2 being a normal distance Δ_2 from loop 1 and with loop 3 being a normal distance Δ_3 from loop 4. Loops 2 and 3 have parameters $\ddot{S}_2$ and $\ddot{S}_3$ associated with them and the method of determination of these parameters is discussed subsequently. Before discussing this point it is necessary to introduce a pseudo-radial parameter r and a position vector $\vec{P}$ associated with each loop. The radial parameter is defined at the downstream boundary (line A'A) as the distance from the loop in question to the inner loop divided by the distance from the outer loop to the inner loop. Thus $r_1 = 0$, $r_2 = \Delta_2/R_{MAX}$, $r_3 = (R_{MAX} - \Delta_3)/R_{MAX}$ and $r_4 = 1$ where R_{MAX} is the distance from the inner loop to the outer loop. The position vector $\vec{P}_i(t)$ is a vector whose components are the x and y coordinates of the i^{th} loop (i = 1, 2, 3, 4) when the parameter $\ddot{S}_i = t$ where t is a number between 0 and 1. With the definition of these quantities it is possible to introduce the general position vector $\vec{P}(r,t)$ where

$$\vec{P}(r,t) = (1-r)^2(1-a_1 r)\vec{P}_1(t) + (a_1+2)(1-r)^2 r\vec{P}_2(t) + r^2\left[1-a_2(1-r)\right]\vec{P}_4(t) + (a_2+2)r^2(1-r)\vec{P}_3(t) \tag{2}$$

$$a_1 = \frac{2}{3r_2 - 1} \qquad a_2 = \frac{2}{3(1-r_2)-1} \tag{3}$$

It should be noted that at r = 0, $\vec{P}(0,t) = \vec{P}_1(t)$ and at r = 1, $\vec{P}(1,t) = \vec{P}_4(t)$. Further since at r = 0,

$$\frac{\partial \vec{P}}{\partial r}(0,t) = \left[\vec{P}_2(t) - \vec{P}_1(t)\right](a_1 + 2) \tag{4}$$

and at r = 1

$$\frac{\partial \vec{P}}{\partial r}(1,t) = \left[\vec{P}_4(t) - \vec{P}_3(t)\right](a_2 + 2) \tag{5}$$

specification of the derivatives at the inner and outer boundaries determines the parametric representation of intermediate loops 2 and 3. Since $\partial\vec{P}/\partial r$ implies $\partial x/\partial r$ and $\partial y/\partial r$, specification of $\partial\vec{P}/\partial r$ at the boundaries controls the angle which the pseudo-radial coordinate line forms with the boundary line. Thus, the four loop method allows specification of the boundary point locations and coordinate angles at these boundaries.

After loops 2 and 3 are parameterized to satisfy the coordinate angle at the boundary points, the grid is constructed as follows. If the grid is to contain M pseudo-radial lines (such as line HI of Fig. 1) and N psuedo-azimuthal lines (such as line QPR), the values of the pseudo-radial coordinate are

$$r(i) = i/(N-1) \quad i = 0,1,2,\ldots,N-1$$

and the values of the pseudo-azimuthal coordinate are

$$t(j) = j/(M-1) \quad j = 0,1,2,\ldots,M-1$$

Then the position vector for each point in the grid is given by Eq. (1).

The preceding has assumed a uniform spacing in the radial direction. If radial grid point concentration is desired, it is simply necessary to assume a radial distribution function. The present analysis assumed a distribution function

$$R = \left[1 - \frac{\tanh D(1-r)}{\tanh D}\right] \tag{6}$$

which concentrates points in the wall region. Grid points then were chosen at r(i) = (i)/(N-1) and the analysis proceeded as outlined. Once the grid point locations are obtained, the required metric data can be calculated by numerical differentiation.

Mean Flow Equations

A solution of the compressible, time-dependent Navier-Stokes equations in conjunction with a suitable turbulence model would serve to predict the flow field for both laminar and turbulent flows. The form of the equations expressed in the more common coordinate systems can be found in standard fluid dynamic texts and the equations themselves have been derived in general tensor form by McVittie (Ref. 41) for inviscid flow and by Walkden (Ref. 42) for viscous flow.

One possible approach for solving the equations in general nonorthogonal form is the strong conservation approach such as that used by Thomas and Lombard (Ref. 43). A second possible approach solves a set of equations in which the metric coefficients do not appear within derivatives (quasilinear form). In both cases the independent spatial variables are transformed from the Cartesian coordinates (x,y) to a new set of coordinates (ξ,η) where

$$\xi = \xi(x,y,t)$$

$$\eta = \eta(x,y,t)$$

$$\tau = t \tag{7}$$

The strong conservation form of the equations then becomes

$$\frac{\partial W/D}{\partial \tau} + \frac{\partial}{\partial \xi}\left[\frac{W\xi_t}{D} + \frac{F\xi_x}{D} + \frac{G\xi_y}{D}\right] + \frac{\partial}{\partial \eta}\left[\frac{W\eta_t}{D} + \frac{F\eta_x}{D} + \frac{G\eta_y}{D}\right] = \frac{1}{Re}\left[\frac{\partial}{\partial \xi}\left(\frac{F_1\xi_x}{D} + \frac{G_1\xi_y}{D}\right) + \frac{\partial}{\partial \eta}\left(\frac{F_1\eta_x}{D} + \frac{G_1\eta_y}{D}\right)\right] \tag{8}$$

where $$D = \xi_x \eta_y - \xi_y \eta_x$$

$$W = \begin{pmatrix} \rho \\ \rho u \\ \rho v \end{pmatrix}, \quad F = \begin{pmatrix} \rho u \\ \rho u^2 + p \\ \rho uv \end{pmatrix}, \quad G = \begin{pmatrix} \rho v \\ \rho uv \\ \rho v^2 + p \end{pmatrix} \quad F_1 = \begin{pmatrix} 0 \\ \tau_{xx} \\ \tau_{xy} \end{pmatrix} \quad G_1 = \begin{pmatrix} 0 \\ \tau_{xy} \\ \tau_{yy} \end{pmatrix} \tag{9}$$

The quasilinear form of the equations is expressed as

$$\frac{\partial W}{\partial \tau} + \xi_t \frac{\partial W}{\partial \xi} + \xi_x \frac{\partial F}{\partial \xi} + \xi_y \frac{\partial G}{\partial \xi} + \eta_t \frac{\partial W}{\partial \eta} + \eta_x \frac{\partial F}{\partial \eta} + \eta_y \frac{\partial G}{\partial \eta}$$
$$= \frac{1}{Re} \left[\xi_x \frac{\partial F_1}{\partial \xi} + \eta_x \frac{\partial F_1}{\partial \eta} + \xi_y \frac{\partial G_1}{\partial \xi} + \eta_y \frac{\partial G_1}{\partial \eta} \right] \tag{10}$$

The problem of proper equation form in non-Cartesian spatial variables has been discussed by several investigators (e.g., Refs. 34, 43 and 44). If the strong conservation form of the equations is to be used, then care must be taken to evaluate the metric data by a method which is consistent with a control volume approach (Ref. 43). Usually this requires numerical evaluation of the metric data <u>even</u> if an analytic functional relationship for the transformation is available. The analytic representation of the metric data, ξ_x, ξ_y, etc., when combined with the strong conservation form of the equations leads to significant error for as straightforward a calculation as low Reynolds number flow about a circular cylinder (Ref. 34). The present effort utilizes the quasilinear form of the equations since this form is much less sensitive to the form of metric evaluation and gives good results for both numerical and analytic evaluations of the metric data. Furthermore, as shown in Refs. 45-47, the quasilinear equations have been used with good results for transonic flow in a cascade environment.

A final item related to the choice of equations is the choice of dependent variables. In the present approach the density and velocity components are used as dependent variables. The energy equation is replaced

by an assumption of constant total temperature thus leading to a relation between pressure, density and velocity.

$$p = \rho R\left(T^{\circ} - \frac{u^2 + w^2}{2C_p}\right) \tag{11}$$

where R is the gas constant, T° is total temperature and C_p is specific heat.

It should be noted that the energy equation can be solved with the momenta and continuity equations at the cost of adding an additional governing equation which increases computer run time. Calculations of this type in transonic cascades which include comparison with heat transfer data have been made by Weinberg, Yang, Shamroth and McDonald (Ref. 48). For steady airfoil flow fields this assumption is reasonable. For unsteady flow, it represents an approximation as can be noted from examination of the unsteady total temperature equation. However, as discussed in Ref. 49, for the cases considered here this assumption should still be valid.

The Turbulence Model

Since the present effort is concerned with high Reynolds number turbulent flows, it is necessary to specify a turbulence model. The results presented were obtained primarily with a mixing length model. The mixing length model assumes the existence of a mixing length, ℓ, and then relates an eddy viscosity, μ_T, to the mixing length by

$$\mu_T = \rho \ell^2 \left[\left(\frac{\partial u_i}{\partial x_j} + \frac{\partial u_j}{\partial x_i}\right)\frac{\partial u_i}{\partial x_j}\right]^{1/2} \tag{12}$$

For flow regions upstream of the leading edge where the flow is attached the mixing length is determined by the usual boundary layer formulation

$$\ell = \kappa y D \qquad \ell \leq \ell_{max} \tag{13}$$

where κ is the von-Karman constant, D is a sublayer damping factor and ℓ_{max} is taken 0.09 δ where δ is the boundary layer thickness. The damping factor, D, which has for the most part been utilized is the van Driest damping factor

$$D = (1 - e^{-y^+/27}) \tag{14}$$

where y^+ is the dimensionless coordinate normal to the wall, yu_τ/ν.

When the mixing length formulation is used in a boundary layer environment, δ is usually taken as the location where $u/u_e = 0.99$. However, this definition assumes the existence of an outer portion of the flow where u_e is independent of distance from the wall and assumes that the location where u_e becomes independent of distance from the wall marks the end of the viscous region. In an airfoil Navier-Stokes calculation no such clear flow division occurs as u approaches the upstream velocity, u_∞, as distance from the wall increases. Therefore, the boundary layer thickness, δ, is set by first determining u_{max}, the maximum velocity at each given streamwise station and then setting δ by

$$\delta = 2.0y_{(u/u_{max} = k_1)} \tag{15}$$

i.e., δ is taken as twice the distance from the wall to the location where $u/u_{max} = k_1$. Two values of k_1 were used; these were 0.80 and 0.90. If the flow is separated, then a minimum mixing length is set by

$$\ell_{min} = 0.1\,hD \tag{16}$$

where h is the local height of the separated region. In the wake the mixing length is made proportional to the wake thickness, δ, and a linear growth of δ with distance is assumed based upon classical free jet boundary growth (e.g., Ref. 50). With this assumption

$$\delta = (\delta_{ps} + \delta_{ss}) + 0.2\,(X - X_{TE}) \tag{17}$$

where δ_{PS} and δ_{SS} are the pressure and suction surface trailing edge boundary layer thicknesses and X_{TE} is the trailing edge location.

The mixing length, ℓ, is taken as 0.2δ. The viscosity is smoothed between regions obtained using the wall formulation for ℓ and the wake formulation for ℓ. Having obtained the turbulent viscosity, μ_T, the turbulent stress, $\overline{-\rho u_i' u_j'}$ is given by

$$-\overline{\rho u_i' u_j'} = \mu_T\left[\left(\frac{\partial u_i}{\partial x_j} + \frac{\partial u_j}{\partial x_i}\right) - \frac{2}{3}\frac{\partial u_k}{\partial x_k}\delta_{ij}\right] \tag{18}$$

Although the mixing length model does not include a transition model, transition can be simulated by specifying a location upstream of which the flow is laminar. This corresponds to forced transition. Even if no forced transition is assumed, the flow in the leading edge region will be laminar as the boundary layer thickness becomes very small in this region.

A second turbulence model which was implemented for a case of an NACA 0012 airfoil at 6° incidence was the two-equation k-ε model. This model is well known (e.g. Refs. 51-54), and has been used by several investigators (e.g., Ref. 48). In brief, the model is based upon a turbulence energy equation

$$\frac{\partial \rho k}{\partial t} + \frac{\partial \rho u k}{\partial x} + \frac{\partial \rho u k}{\partial y} = \frac{\partial}{\partial x_k}\left[\left(\mu + \frac{\mu_T}{\sigma_k}\right)\frac{\partial k}{\partial x_k}\right]$$
$$+ \mu_T\left(\frac{\partial u_i}{\partial x_k} + \frac{\partial u_k}{\partial x_i}\right)\frac{\partial u_i}{\partial x_k} - \rho\epsilon - 2\mu\frac{\partial k^{1/2}}{\partial x_j}\frac{\partial k^{1/2}}{\partial x_j} \tag{19}$$

and a turbulence dissipation equation

$$\frac{\partial \rho \epsilon}{\partial t} + \frac{\partial \rho u \epsilon}{\partial x} + \frac{\partial \rho v \epsilon}{\partial y} = \frac{\partial}{\partial x_j}\left[\left(\mu + \frac{\mu_T}{\sigma_\epsilon}\right)\frac{\partial \epsilon}{\partial x_j}\right]$$
$$+ C_1\frac{\epsilon}{k}\mu_T\left(\frac{\partial u_i}{\partial x_k} + \frac{\partial u_k}{\partial x_i}\right)\frac{\partial u_i}{\partial x_k} - C_2\frac{\epsilon^2\rho}{k} - 2\mu\mu_T\left[\left(\frac{\partial^2 u_i}{\partial x_k \partial x_\ell}\right)\right]^2 \tag{20}$$

The turbulence viscosity is then obtained via the Prandtl-Kolmogorov relation

$$\mu_T = \rho C_\mu k^2/\epsilon \; f(y/\delta) \tag{21}$$

where C_μ is a turbulence structural coefficient and $f(y/\delta)$ is a factor used to ensure small turbulent viscosities at locations far from the airfoil. The function $f(y/\delta)$ is taken as

$$f(y/\delta) = 1.0 \qquad y \le \delta$$

$$f(y/\delta) = e^{-b(y/\delta - 1.0)} \qquad y > \delta \tag{22}$$

where b is a constant.

In the present analysis the following values were assumed

$$\sigma_\epsilon = 1.3$$

$$\sigma_k = 1.0 \tag{23}$$

$$C_1 = 1.55$$

and C_μ and C_2 were made functions of turbulence Reynolds number, $R_T = \rho k^2/\mu\varepsilon$,

$$C_\mu = 0.09 \exp\left[-2.5(1. + R_T/50.)\right] \tag{24}$$

$$C_2 = 2.0\left\{1.0 - 0.3\left[\exp(-R_T^2)\right]\right\} \tag{25}$$

Numerical Procedure

The numerical procedure used to solve the governing equations is a consistently split linearized block implicit (LBI) scheme originally developed by Briley and McDonald (Ref. 29). A conceptually similar scheme has been developed for two-dimensional MHD problems by Lindemuth and Killeen (Ref. 55). The procedure is discussed in detail in Refs. 29 and 56. The method can be briefly outlined as follows: the governing equations are replaced by an implicit time difference approximation, optionally a backward difference or Crank-Nicolson scheme. Terms involving nonlinearities at the implicit time level are linearized by Taylor expansion in time about the solution at the known time level, and spatial difference approximations are introduced. The result is a system of multidimensional coupled (but linear) difference equations for the dependent variables at the unknown or implicit

time level. To solve these difference equations, the Douglas-Gunn (Ref. 57) procedure for generating alternating direction implicit (ADI) schemes as perturbations of fundamental implicit difference schemes is introduced in its natural extension to systems of partial differential equations. This technique leads to systems of coupled linear difference equations having narrow block-banded matrix structures which can be solved efficiently by standard block-elimination methods.

The method centers around the use of a formal linearization technique adapted for the integration of initial-value problems. The linearization technique, which requires an implicit solution procedure, permits the solution of coupled nonlinear equations in one space dimension (to the requisite degree of accuracy) by a one-step noniterative scheme. Since no iteration is required to compute the solution for a single time step, and since only moderate effort is required for solution of the implicit difference equations, the method is computationally efficient; this efficiency is retained for multidimensional problems by using what might be termed block ADI techniques. The method is also economical in terms of computer storage, and in its present form requires only two time levels of storage for each dependent variable. Furthermore, the block ADI technique reduces multidimensional problems to sequences of calculations which are one-dimensional in the sense that easily solved narrow block-banded matrices associated with one-dimensional rows of grid points are produced. A more detailed discussion of the solution procedure is discussed by Briley, Buggeln and McDonald (Ref. 58) and is given in the Appendix.

Boundary Conditions

An important component of the airfoil analysis concerns specification of boundary conditions. The present analysis requires boundary conditions to be set along the lines, $\xi = \xi_{min}$, $\xi = \xi_{max}$, $\eta = \eta_{min}$ and $\eta = \eta_{max}$. With the coordinate system sketched in Fig. 1, $\xi = \xi_{min}$ (line AA') and $\xi = \xi_{max}$ (line DD') are downstream boundaries. In the early work done under this effort derivatives were set to zero at this boundary and function conditions specified on the remainder of the outer boundary. On the airfoil surface no-slip conditions are used in conjunction with an inviscid momentum equation (which for no motion and no heat transfer reduced to zero density

gradient) as boundary conditions and either the turbulence energy or its derivative was specified at the surface when turbulence energy was included as a variable. More recently the boundary conditions were modified based upon a suggestion by Briley and McDonald (Ref. 59). Following this suggestion, static pressure is specified along with velocity derivatives along the downstream boundaries (lines AA' and DD') and along the aft portion of the outer boundary (line segments AB and CD). Total pressure, angle of incidence and the density derivative are specified along the outer boundary segment BC. This approach was used successfully (Refs. 45-48, 60) in a Navier-Stokes solution to the cascade problem and has been incorporated into the airfoil analysis.

In addition, calculations have been made with the full transverse momentum equation rather than the normal pressure gradient equal to zero as a wall boundary condition. Little difference was noted in the solution although the full transverse momentum equation boundary condition occasionally showed some tendency toward numerical instability and may require smaller time-steps. Finally, calculations have been made in which tunnel wall boundary conditions are simulated by specifying the flow direction and a full slip condition along AB and CD.

Artificial Dissipation

One major problem to be overcome in calculating high Reynolds number flows using the Navier-Stokes equations is the appearance of spatial oscillations associated with the so-called central difference problem. When spatial derivatives are represented by central differences, high Reynolds number flows can exhibit a saw tooth type oscillation unless some mechanism is added to the equations to suppress their appearance. This dissipation mechanism can be added implicitly to the equations via the spatial difference molecule (e.g., one-sided differencing) or explicitly through addition of a specific term. The present author favors this latter approach for two reasons. First, if a specific artificial dissipation term is added to the equations, it is clear precisely what approximation is being made. Secondly, if a specific term is added to suppress oscillations, the amount of artificial dissipation added to the equations can be easily controlled in

magnitude and location so as to add the minimum amount necessary to suppress spatial oscillations.

The results presented herein basically utilize two levels of artificial dissipation. During initial phases of the present study a term of the form $\nu_{art}\ \partial^2\phi/\partial z^2$ was added to the governing equation where $\phi = \rho, u, v$ for the continuity, x-momentum and y-momentum equations respectively and ν_{art} is determined by

$$\frac{U_z \Delta Z}{\nu + (\nu_{art})_z} \leq \frac{1}{\sigma_z} \tag{26}$$

In the above equation ΔZ is the distance between grid points in a given coordinate direction, U_Z is the velocity in this direction, σ_Z is the artificial dissipation parameter for this direction and ν is the kinematic viscosity. The equation determines ν_{art} with ν_{art} taken as the smallest non-negative value which will satisfy the expression. It should be noted that in two space dimensions each equation contains two artificial dissipation terms, one in each coordinate direction. For example, the streamwise momentum equation expressed in Cartesian coordinates would contain the artificial dissipation terms

$$(\nu_{art})_x \frac{\partial^2 u}{\partial x^2} + (\nu_{art})_y \frac{\partial^2 u}{\partial y^2} \tag{27}$$

The parameter σ_z was taken as 0.5.

During the time period of the present contract effort, various methods of adding artificial dissipation were investigated in Ref. 46 and these were evaluated in the context of a one-dimensional model problem. The model problem used was one-dimensional flow with heat transfer. Flow was subsonic at the upstream boundary, accelerated via heat sources until a Mach number of unity was reached and then accelerated by heat sinks. The exit back pressure was raised to cause a shock to appear in the supersonic region. This basic one-dimensional problem contained many relevant features including strong accelerations and, therefore, it served as a good test case for evaluating various forms of artificial dissipation which could be used. Several different types of artificial dissipation terms were considered, and it was concluded that for the present numerical method, a second order

artificial dissipation approach such as represented by Eqs. (26) and (27) is suitable. However, instead of the parameter, σ, being 0.5 it should be set at approximately 0.05. At this value, sufficient artificial dissipation is added to the equations to suppress spurious oscillations, but the amount added does not significantly change the physical solution. Furthermore, as shown in Refs. 47-48, the solutions obtained with $\sigma = 0.050$ change only little when σ is lowered to 0.025. Other confirmations of this approach were given in Refs. 61 and 62 as well as in this present effort. Based upon these studies, it has been concluded that $\sigma < 0.1$ gives accurate representation for most two-dimensional flows.

An alternate method of including artificial viscosity is the so-called conservation form in which dissipation terms of the type

$$\frac{\partial}{\partial x}\left\{(\nu_{art})_x \frac{\partial u}{\partial x}\right\} + \frac{\partial}{\partial y}\left\{(\nu_{art})_y \frac{\partial u}{\partial y}\right\} \tag{28}$$

are added to the equations. This form confines the integrated effect of the terms over the computational domain to the computational boundaries since

$$\iint_A \frac{\partial}{\partial x}\left\{(\nu_{art})_x \frac{\partial u}{\partial x}\right\} dx\, dy =$$

$$\int_s \left(\nu_{art_x} \frac{\partial u}{\partial x}\right) dy = \int_s \left(\nu_{art_x}\right) \frac{\partial u}{\partial x} \frac{\partial y}{\partial s}\, ds \tag{29}$$

where A is the area of the computational domain and S is the boundary line. If the artificial viscosity and its derivative are set to zero on the boundary, global conservation is obtained. However, local conservation obviously is not. Calculations have been run with this latter form of artificial dissipation and for the cases run no significant differences appear in the predicted flow fields due to artificial dissipation of the form given in (28) as opposed to that given in equation (27).

Convergence and Run Times

When a steady flow is sought via a time marching technique, the question arises as to when convergence is obtained. In considering this question, several factors must be taken into account. First of all, not all flows

reach a steady state. For example, airfoils at high incidence which shed vortices or airfoil flows in which a shock wave is present may never become truly steady. In the former case, vortices are shed in some quasi-periodic manner and the unsteadiness has a large time scale. In the latter case, the shock position may move leading to an unsteadiness with a small time scale. Obviously, in these cases no steady flow solution is guaranteed. Secondly, the numerical technique used may hinder complete convergence. For example, in the present approach the turbulent viscosity is lagged by one step in time and this interaction between the viscosity evaluation and the mean flow calculation may hinder or even prevent complete convergence.

During the early part of the present effort when steady state solutions were sought, the calculated results were monitored to assess convergence. In particular, the surface pressure distribution, the location of separation points and the velocity field in the vicinity of the airfoil were monitored and when they ceased to vary significantly for significant time scales, the calculation was terminated. During latter parts of the effort, an additional criterion was added. This was based upon the evaluation of the residual for each equation. The residual of each equation is obtained by setting the time-derivative term to zero, and placing all remaining terms on the right-hand side of the equation. The sum of all terms on the right hand side of the equation defines the residual. Obviously, when the residual is zero the equations satisfy a steady state solution. Both the maximum residual throughout the domain for each equation and the average residual within the domain for each equation were monitored. These usually could be decreased by between two to four orders of magnitude during the run when steady solutions were sought.

However, even the presence of residuals requires interpretation. As previously discussed, these could be indicative of flow unsteadiness. Also, relatively large residuals occur at the airfoil cusp trailing edge. In general, calculations for which steady solutions are sought are initiated from a very simple initial flow field. The initial flow field has constant pressure throughout and a velocity field identical to that at upstream infinity with a simple boundary layer correction. For steady flows converged solutions are usually obtained within 70 time steps.

In regard to run time, the current code is a general research type code which was created with flexibility in mind. Therefore, items such as the

equations solved, boundary conditions specified, dependent variable choice, form of artificial dissipation, etc. can be changed with only a small amount of effort. Obviously, the price of flexibility is increased computer run time. In the present code the run time for a 141 x 39 grid is approximately 15 cpu secs per time step on a CYBER 203. The code used is not fully optimized for scalar operation and has no vectorization. It is estimated that the run time could be reduced to 7 sec per time step with further scalar optimization without compromising existing generality and an additional factor of ten could be obtained through vectorization.

RESULTS

Results obtained under this contract effort include both steady and unsteady airfoil calculations under a variety of flow conditions. Early results appear in Ref. 34. Results obtained since Ref. 34 are presented in the present section.

Low Mach Number - High Incidence NACA 0012 Airfoil

The low Mach number - high incidence calculation was made for an NACA 0012 airfoil immersed in a free stream having a Reynolds number of 10^6 and a Mach number of 0.148. The calculation was run prior to the artificial dissipation study (Refs. 47 and 48) and consequently a dissipation parameter, σ, equal to 0.5 was used. Since the flow was subsonic, the results are expected to be qualitatively correct with more numerical dissipation than actually required; the major discrepancy is expected to be in the leading edge suction peak region. Results of this case which have been presented in Ref. 35 are reproduced in a condensed form here.

The calculation was run on a 'C' type grid having 81 pseudo-radial lines and 39 pseudo-azimuthal lines. The grid was highly non-uniform with the first point off the airfoil a distance of 0.2×10^{-4} chords away from the airfoil. In contrast, the last point was placed four chords away from the airfoil with a radial spacing of 0.5 chords. Similarly, the streamwise (pseudo-azimuthal) grid was concentrated in the vicinity of the airfoil leading edge with the minimum spacing being approximately 0.4×10^{-2} chords. The calculation was initiated from a converged solution for the airfoil at 6 degrees incidence. The incidence was then changed to 19 degrees via the equation

$$\alpha = \alpha_0 + \frac{\Delta\alpha}{2}\left[1.0 - \cos\omega(t - t_0)\right] \qquad t_0 < t < (t_0 + \pi)/\omega \qquad (30)$$

where

$$\alpha_0 = 6°, \quad \Delta\alpha = 13°, \quad \omega = 5, \quad t_0 = 1.20 \tag{31}$$

For $t>(t_0+\Pi)/\omega$, the incidence was held constant at

$$\alpha = \alpha_0 + \Delta\alpha \tag{32}$$

It should be noted that the dimensionless frequency, $k = \omega c/2U_\infty = 2.5$, represents a very high value for airfoil calculations with the 13° ramp amplitude.

The results of the calculation during the ramping period are presented in Figs. 2 and 3. Figure 2 shows the pressure coefficient distribution at various incidence angles. At six degrees the pressure distribution is typical of that found for a steady airfoil; the suction peak has been smeared and diminished due to insufficient streamwise resolution and the relatively large amount of artificial dissipation as discussed previously. As the incidence changes from 6 to 9 degrees the rapid motion, particularly in the trailing edge region, causes high pressure to appear on the lower side of the airfoil and low pressures to appear on the upper side. It should be noted that the velocity of the airfoil trailing edge relative to the inertial frame reaches a maximum value of 0.4 U_∞ and, therefore, large deviations from the steady solution are to be expected. The situation becomes more pronounced at 12.5 degrees; however, by 14 degrees a tendency to return to the usual static airfoil pressure distribution appears. Finally, at the last incidence angle, 19 degrees, ($t = 1.93$), the basic pressure distribution is approaching the type expected for a steady airfoil with no evidence of stall. The location of the separation points is presented in Fig. 3. At the initiation of the ramp motion no separated flow was present; however, separation appeared soon after the ramp motion began and the trailing edge separation point moves continuously upstream as shown in the figure. During this process the separated region remains very thin and has only a minimum viscous displacement effect upon the outer nominally inviscid flow.

After cessation of the motion, the flow continues to develop and the pressure distribution undergoes radical changes as shown in Figs. 4-6. The major changes occur in the airfoil leading edge region where the suction peak

appearing on the airfoil upper surface continues to drop in magnitude from a value of approximately 6.8 at t = 1.83 (just after the cessation of airfoil motion) to a value of approximately 1.2 at t = 5.38. A unit increment in t represents the time required for a particle moving at free stream velocity to transverse a distance of one chord. The drop in the suction peak and the accompanying decrease in airfoil lift exhibited in Figs. 4-6 are consistent with the development of airfoil stall. The calculation also predicts a minor movement of the airfoil front stagnation point towards the geometric leading edge. In addition to the loss of lift, the analysis predicts a pressure perturbation to initiate at t ≈ 3.7 (see Fig. 5) and then move downstream at a speed of approximately 35% free stream velocity. Although quantitative comparisons between this prediction and data are not available, the predicted flow seems physically realistic.

Upon reaching 19 degrees, the motion ceased and the airfoil flow field was allowed to develop at 19°. A comparison of the calculated results and the measured data of Young, Meyers and Hoad (Ref. 63) for an airfoil at 19.4° incidence is presented in Fig. 7. Figure 7 compares the predicted and measured values of the zero velocity line. Below this line, the flow is directed toward the leading edge and above this line the flow is directed toward the trailing edge. The predicted values are shown as a function of time. During the ramping process, the separated region present was too thin to be shown on the scale of Fig. 7 and the results shown are at times well past the cessation of the ramping motion at t ≈ 1.9. The results presented in Fig. 7 show the growth of the backflow velocity zone with time, and at the latter times shown the backflow zone position has converged over most of the airofil as continued growth is confined to regions in the vicinity of the airfoil trailing edge. As can be seen, the comparison between the calculated zone location and that measured by Young, Meyers and Hoad is very good.

A vector plot of the velocity field as measured by Young, Meyers and Hoad is shown in Fig. 8. These results show a large separated region to be present over the airfoil upper surface with separation initiating in the immediate vicinity of the airfoil leading edge. A vortex appears to be centered at roughly the eighty percent chord location. The data (not shown on this figure) indicated that the wake closure point was located well downstream of the airfoil trailing edge and above the airfoil suction surface.

Another feature is the appearance of a very strong shear layer in the airfoil trailing edge vicinity where the suction surface and pressure surface flow fields meet. Finally, the calculated results, Figs. 9 and 10, indicate that flow is entrained into the recirculation region from two sources. One source is the flow region above the recirculation zone. The second source is the flow which originates on the airfoil pressure surface, then passes into the mixing layer which forms at the airfoil trailing edge and finally is entrained into the recirculation region from below.

Predicted velocity vector fields are shown in Figs. 9 and 10. These figures represent the flow field at times t_1 and $t_1+\Delta t$ where Δt is the time required for a free stream particle to move a distance of one chord length. The analysis predicts the formation of a large separation region which initiates very near the airfoil leading edge; the calculated flow field is in qualitative agreement with the data shown in Fig. 8. Other similarities between data and calculation can be found in the vortex formation and in the strong shear layer which appears at the airfoil trailing edge. In addition, the calculated flow field was characterized by significant flow unsteadiness in the leading edge region which limited the permissible maximum time step. This characteristic of unsteady leading edge flow also appeared in the experimental study.

In regard to other features, the analysis showed the vortex to be moving downsteam at a velocity of approximately 0.3 U_∞; however, no regular shedding pattern was observed in the experiment. Some comments on this are in order. First of all, the calculation was not run long enough to determine if a regular shedding will result although the first vortex being formed definitely appears to be in the process of shedding. Secondly, although the experiment did not detect any regular shedding pattern, it is possible that an irregular shedding did occur.

Calculated vorticity contours at the two times are shown in Figs. 11 and 12. The vorticity contours presented correspond to normalized values of -100, -25, -10, -5, 0, 5, 10, 25, 100. In both figures, the vorticity on the airfoil pressure surface is confined to the boundary layer whereas that on the suction surfaces occurs in two locations. One region of vorticity is located in the wall layer close to the airfoil surface; the second region is a 'tongue-like' region extending from the vicinity of the airfoil leading

edge into the 'free stream'. This contour line represented by the value 5 is a region of a local maximum vorticity. As can be seen by comparing Figs. 11 and 12, the tongue-like region of vorticity appears to break off and be convected downstream as a local concentrated region (See Fig. 12). This may be interpreted as the initiation of a shed vortex. A third area of high vorticity concentration occurs at the airfoil trailing edge where the sharp mixing layer is present.

A closer examination of the predicted flow field shows the emergence of an inner counter-clockwise rotating separation zone which occurs under the main suction surface separation zone. As can be seen in Figs. 8-10, the major separated region is a large region of clockwise rotation. However, a detailed vector plot of the mid-chord portion of the suction surface presented in Fig. 13 shows a secondary separation region of counter-clockwise rotation completely embedded within the primary separated zone. The stagnation point location, the flow separation at the stagnation point, the acceleration about the leading edge and the initiation of flow separation are all shown clearly. A detail of the leading edge region is shown in Fig. 14. Static pressure contours are presented in Ref. 35.

0.5 Mach Number - High Incidence NACA 0012 Airfoil

A calculation similar to the low Mach number - high incidence case discussed previously was made for an NACA 0012 airfoil immersed in a free stream of Reynolds number 1.4×10^6 and Mach number of 0.5. The calculation was initiated from 6 degrees incidence with a cosine ramp motion, Eqs. (30-32), bringing the airfoil to 19 degrees incidence. In general, the results for the 19°, $M_\infty = .5$ case were similar to the results obtained for the 19°, $M_\infty = .15$ case discussed previously. The flow did not become steady during the calculation as a large separation zone appeared over the suction surface. A velocity vector plot showing the flow field at a time $2\ T_{ref}$ past the cessation of airfoil motion is shown in Fig. 15; T_{ref} is the time for a free stream particle to move a distance of one chord. Several features of the flow are clearly evident in this figure. The flow approaches the airfoil leading edge and branches with part of it passing over the suction surface and part passing over the pressure surface. A detail of the leading edge region is shown in Fig. 16. Figures 15 and 16 clearly show the flow branching and the acceleration about the airfoil leading edge. The flow on the pressure surface remains well-behaved with a thin boundary layer developing on the airfoil surface. The situation on the suction surface is much different with separation occurring almost at the airfoil leading edge and a large separation zone being formed over the suction surface. The separation zone and accompanying vortex is also shown clearly in Fig. 17 which gives vorticity contours, the vorticity being defined as $\nabla \times \vec{V}$. The vorticity pattern is generally similar to that obtained for the $M_\infty = .15$ calculation with the maximum core value in the present case being approximately twice that of the previous case. Static pressure contours are presented in Fig. 18.

Flow About an Airfoil Oscillating in Pitch at Low Incidence

The first oscillating airfoil case considered was flow about an NACA 0012 airfoil immersed in a free stream at a Reynolds number based upon airfoil chord of 0.26×10^7, and a Mach number of 0.20. The case was run as

an initial demonstration case for an oscillating airfoil prior to attacking the dynamic stall problem. The airfoil was assumed to oscillate in pitch about its quarter chord point with the incidence given by

$$\alpha = \alpha_0 + \frac{\Delta\alpha}{2}\left[1.0 - \cos\omega(t - t_0)\right] \tag{33}$$

The reduced frequency, $\kappa = \omega c/2U_\infty$, was taken to be 0.12. The calculation was run with the dissipation parameter, σ, set equal to 0.5 and was initiated from a steady solution at zero degree incidence and then followed the incidence variation given by Eq. (33).

The predicted lift versus incidence curve is presented along with the steady and unsteady data of Grey and Liiva (Ref. 64) in Fig. 19. Considering first the experimental data, the unsteady curve shows a hysteresis loop. Furthermore, the general slope of the curve is less than that of the steady data and the unsteady lift at zero incidence is higher than that of the steady data (which is zero). The prediction shows the same general characterstics. The calculation was initiated at zero degrees incidence from a steady calculation and followed the theoretical quasi-steady lift-incidence curve until $\alpha \approx 4°$. After reaching 4°, the lift predicted is less than the inviscid value and this is primarily a result of the under prediction of the suction peak resulting from the specification of $\sigma = 0.5$ where σ is the artificial dissipation parameter. The dissipation factor was taken as $\sigma = 0.5$ since this calculation was made prior to the dissipation parameter study of Refs. 45 and 46. Upon reaching the maximum incidence, $\alpha = 10.5°$, the curve forms a hysteresis loop as incidence decreases. This loop is somewhat more pronounced than that measured. After reaching the minimum value of $\alpha = 0°$, the lift increases with incidence and at the last time calculated the loop is closing. Although the thickness of the predicted hysteresis loop is somewhat greater than that of the measured loop, the average slopes agree. In addition, both prediction and data show significant lift at zero incidence; this is in contrast to the quasi-steady calculation. A detailed examination of the flow field prediction shows the major contribution to the finite thickness lift loop results from the suction

surface boundary layer thickness for $\dot{\alpha} < 0$ being greater than that for $\dot{\alpha} > 0$ at the same value of α. This result represents a lag in the boundary layer reaction of the pressure gradient which modifies the mid-chord and trailing pressure distribution. The mid-chord and trailing edge effect is somewhat modified by differences in the leading edge where the suction peak for $\dot{\alpha} < 0$ is more pronounced than that for $\dot{\alpha} > 0$. It should be noted that the loop calculation is a very sensitive one and its formation results from relatively small pressure changes on both the pressure and suction surfaces. Further, this interpretation should be regarded as approximate due to the value of artificial dissipation used. Velocity vector plots are given in Figs. 20-22. These figures clearly show the general flow pattern which includes the approach to the leading edge stagnation point, acceleration around the leading edge and the boundary layer and wake development. A comparison of Figs. 20 and 22 shows that during the upstroke ($\dot{\alpha} > 0$) the flow along the aft portion of the airfoil tends to align with the pressure (lower) surface. Furthermore, the differences in the suction surface boundary layer thickness and wake position are evident. Vector plots in the vicinity of the leading edge are shown in Figs. 23-25. It should be noted that the flow patterns upstream of the airfoil in Figs. 23 and 25 are significantly different with the flow for $\dot{\alpha} < 0$ (Fig. 25) showing considerably more turning in the region upstream of the leading edge region. Further discussion of this case is presented in Ref. 36.

NACA 4412 Airfoil

The next calculation to be discussed is flow about an NACA 4412 airfoil at high incidence. The calculation models the experiment of Coles and Wadcock (Ref. 65) which considered flow about an NACA 4412 airfoil at Reynolds number based upon chord of 1.5×10^6 and Mach number of approximately .07. The airfoil was placed in a wind tunnel and oriented at geometric incidence of 13.7 degrees to the free stream. Data taken included static pressure measurements on the airfoil surface as well as velocity profile measurements at selected boundary layer and wake locations. Details of the experiment can be found in the cited AIAA Journal article (Ref. 65).

The NACA 4412 calculation differed from those previously presented in two ways. First, the calculation was run with slip tunnel wall boundary conditions as discussed in the boundary condition section of this report and the calculation was run in a 141 x 39 mesh as opposed to the 81 x 39 mesh previously used. Finally, the calculation was run using an artificial dissipation parameter, σ, of 0.05. As shall be shown, the increased resolution and decreased dissipation parameter had a major beneficial effect on the quantitative comparison between calculation and measurement.

The NACA 4412 calculation was carried out with a grid containing 141 pseudo-azimuthal (streamwise) grid points and 39 pseudo-radial grid points with high streamwise resolution being obtained in the vicinity of the airfoil leading edge and high normal resolution being obtained in the airfoil boundary layer. The streamwise grid spacing in the leading edge region was approximately .002 chords and the radial grid spacing at the airfoil surface was approximately 10^{-5} chords.

Calculations were made for flow at four incidences; 7.7 degrees, 10.8 degrees, 12.3 degrees and 13.7 degrees. The calculation at 7.7° was initiated from a uniform flow with a no-slip condition gradually applied by decreasing the velocity over several grid points in the vicinity of the airfoil surface. The calculation was made using the time-conditioning methods suggested in Refs. 66 and 67. It should be noted that the zero lift incidence for the NACA 4412 airfoil is -4° (Ref. 68) and, therefore, the cases considered represent airfoil flow fields at large incidence. Predicted surface pressure distributions for each case are shown in Fig. 26. Although to our knowledge no data are available for comparison at the lower incidence angles, the comparison between data and prediction is excellent for the 13.7 degree case.

A comparison also can be made of the predicted and measured separation points. At the two lower incidences only a small amount of separation was predicted as the boundary layer separation occurred at x/c = .96. However,

at 12.3° incidence the separation point moved upstream to x/c = .82 and at 13.7° it progressed to x/c = .72. This final value is in good agreement with the Coles-Wadcock data which indicated separation at x/c = .70. Although detailed pressure distribution comparisons cannot be made at the lower incidences, lift coefficient comparisons can be made to assess the prediction procedure. A comparison between predicted and measured lift coefficient is shown in Fig. 27 where the data are taken from Abbott and von Doenhoff (Ref. 68) for $Re_c = 3.0 \times 10^6$. Although the predictions and data apply to somewhat different Reynolds numbers, the results should be insensitive to Reynolds number at lower incidences and only become somewhat sensitive as stall is approached. As can be seen in Fig. 27, the comparison is very good.

The final comparisons concern velocity profiles. The Coles-Wadcock data give velocity profiles for both the velocity component parallel to the line connecting the airfoil leading and trailing edge locations and the component normal to this line. The streamwise velocity profiles are compared in Fig. 28, and the normal velocity profiles are compared in Fig. 29. Considering first the streamwise velocity profiles, it should be noted that the velocity is normalized by U_{ref}, the velocity at a specified tunnel location and, therefore, U/U_{ref} does not necessarily approach unity at the edge of the profile. In all cases, however, the predicted and measured edge velocities were in good agreement. Of the profiles compared in Fig. 28, two are taken in the aft region suction surface boundary layer and two in the wake. Both boundary layer profiles (x/c = .642 and x/c = .908) are in a strong adverse pressure gradient region. The predicted velocity profiles are somewhat thicker than the measured profiles and appear somewhat more advanced toward separation. However, the comparison is reasonably good in a qualitative sense. Similarly the wake profiles are affected by the somewhat too large prediction of the suction surface boundary layer thickness, however, the wake development also is reasonably good. Obviously, further investigations concerning both grid resolution (particularly in the streamwise direction) and turbulence and transition modeling may be required if the comparison is to improve. In particular based upon some more recent studies for cascade flows accurate prediction of the transition point are required to obtain accurate predictions of the suction surface boundary layer profile. Comparisons between the predicted and measured normal velocity profiles are given in Fig. 29. Again, the predictions and measurements are in reasonable agreement.

A more comprehensive view of the flow field can be obtained via vector and contour plots. A velocity vector plot of the flow field is shown in Fig. 30 and contours of U-velocity, W-velocity and pressure coefficients are presented in Figs. 31-33. The velocity vector plot clearly shows the flow turning as it passes about the airfoil and the boundary layer build-up on the suction surface. The development of the large W-velocity component in the leading edge region is shown in Fig. 32 and the pressure field is shown in Fig. 33. The leading edge region is shown in detail in Figs. 34-37 which considers the flow in the initial 5% chord region.

NACA 4412 - Grid Resolution and Artificial Dissipation Study

As part of the NACA 4412 study, an effort was undertaken to assess the effects of the artificial dissipation parameter, σ, and grid resolution. As previously discussed, the present prediction procedure utilizes second order central spatial differences and consequently requires addition of artificial dissipation terms to suppress spatial oscillations. The present approach adds a second-order dissipative term in the following manner. During the calculation, the flow field is examined at each grid point and to maintain stability terms of the form

$$\frac{d_x}{\rho^n}\frac{\partial^2\phi}{\partial x^2} \text{ and } \frac{d_y}{\rho^n}\frac{\partial^2\phi}{\partial y^2}$$

are added to the equation. The variable ϕ is taken as ρ in the continuity equation, u in the x-momentum equation and v in the y-momentum equation and n is 1 for the continuity equation and zero for the momentum equations. The factor d_x is taken as the maximum of $\sigma\rho u\Delta x-\mu$ and zero and the factor d_y is taken as the maximum of $\sigma\rho v\Delta y-\mu$ and zero where σ is the artificial dissipation parameter, ρ is density, u and v are velocity components, Δ_x and Δ_y are grid spacing and μ is viscosity. These points are discussed in detail in the artificial dissipation subsection of the present report.

In addition to the calculations for $\sigma = .05$, presented in the previous subsection, NACA 4412 airfoil calculations were also made for $\sigma = .10$ and 0.5. The calculation for $\sigma = 0.10$ was initiated from the $\sigma = .05$ calculation by abruptly changing the value of the dissipation parameter as the solution was restarted. The prediction for $\sigma = .05$ and .10 were nearly identical as shown in Fig. 38. The insensitivity of predicted flow to changes in σ between 0.10 and 0.05 has since been observed in other calculations performed at SRA (e.g.; Refs. 62 and 69). After completing the $\sigma = .10$ calculation, the procedure was restarted with $\sigma = .50$. This calculation proceeded to diverge from the $\sigma = .05$, .10 results and the $\sigma = .50$ calculation was discontinued after fifty time steps although it had not yet converged and was continuing to move farther from the previous solutions. Since these results clearly demonstrate the effort of increasing the artificial dissipation factor to 0.5, no attempt was made to obtain the converged solution. The results of Fig. 38 clearly indicate that for the case considered (i) once $\sigma = .10$ a further decrease to $\sigma = .05$ does not affect the solution, and (ii) a value of $\sigma = .50$ leads to an inaccurate solution and calculations run with this value of artificial dissipation must be regarded as suspect in terms of quantitative results.

The second item considered under the present study concerns grid resolution. The NACA 4412 results presented in the previous subsection were obtained with a highly stretched grid having 141 pseudo-azimuthal grid points and 39 pseudo-radial grid points. The grid was stretched so as to obtain maximum radial resolution near the airfoil surface (the grid spacing here was 10^{-5} chords), and maximum streamwise resolution in the leading edge region (the grid spacing here being .002 chords). For the grid resolution study, the calculation at 7.7 degrees incidence was repeated for two new grid sizes. In each case, the pseudo-radial grid was kept the same (39 points) since it is felt that this grid is required due to the presence of the Heimenz layer in the leading edge region and the laminar sublayer on the mid-chord and trailing edge regions. However, the streamwise grid requirements are somewhat less definite and consequently the 7.7° incidence calculation was repeated for 81 and 51 streamwise grid points. In each case, the relative stretch was kept the same as used for the 141 grid point cases. The calculations for the three cases showed no significant differences. The surface pressures were nearly identical with some slight smearing of the

suction peak for the 81 and 51 point calculations. However, the predicted lift coefficients only varied by + 3 per cent and the skin friction coefficients were also in very close agreement. Therefore, for the 7.7° incidence case, a 51 x 39 grid appeared to be adequate.

The 7.7° incidence case is not a severe test since the flow is reasonably well behaved in this case. Therefore, a second study was made for a case at 12.3° incidence. In this case, a converged surface pressure distribution was obtained with the 141 x 39 grid and the results are shown in Fig. 39. However, when the calculation was repeated for a 51 x 39 grid, the surface pressure distribution would not converge and a nonconverged result is shown in Fig. 39. Obviously, in this more demanding case at higher incidence, 51 pseudo-azimuthal grid points are inadequate.

High Incidence Dynamic Stall Calculation - NACA 0012 Airfoil

The final case considered is that of an NACA 0012 airfoil in dynamic stall. The calculation was run against the data of St. Hilaire, Carta, Fink and Jepson (Refs. 70 and 71). The case chosen was case 51.005 for a NACA 0012 airfoil oscillating in pitch. The free stream Reynolds number was 2.08×10^6, the free stream Mach number was 0.30, the reduced frequency was 0.125, the mean incidence was 12°, and the oscillation amplitude was 8°. A converged calculation was first obtained for an airfoil at 4° incidence; this result is compared with the data of Gregory and O'Reilly (Ref. 72) in Fig. 40. As can be seen, the comparison for this steady calculation is very good. A comparison between predicted and measured lift and moment coefficients is presented in Figs. 41 and 42. In regard to the lift coefficient agreement is reasonably good on the upstroke, however, the measured lift stall appears to occur before the calculated lift stall. The dotted portion of the line represents that portion of the calculation for which it was necessary to increase the artificial dissipation factor to 0.5 as will be discussed subsequently. During stall, the measured lift was less than that calculated. However, the agreement appears to be qualitatively reasonable for this case. Considering next the moment coefficient comparison, the agreement between calculation and measurement again is qualitatively good.

Although instructive, the comparison of measured and calculated coefficients only gives a comparison of integrated quantities. Relatively small differences in pressure distributions can lead to significant differences in lift coefficient and large differences in moment coefficients. Obviously, more insight can be gained via a comparison of the pressure distributions. Such distributions are presented in Figs. 43-50. Three comparisons during the upstroke are shown in Figs. 43 and 44. As can be seen, the agreement is very good. The data were reconstructed from the Fourier coefficients given by St. Hilaire and Carta (Ref. 72). The third measured data point on the pressure surface ($x/c \approx .066$) gave very erratic results and was not plotted for most of the comparisons. The excellent comparisons shown in Figs. 43 and 44 give evidence to the time-accurate calculation for the surface pressure.

Figure 45 presents a comparison at $\alpha = 17.7°$, $\dot{\alpha} > 0$. This is near the incidence where stall would first be inferred fom the lift and moment curves of Figs. 41 and 42. The figure shows some discrepancy between predicted and measured values as the data present some evidence of a vortex being shed on the suction surface leading edge. The discrepancy increases in Fig. 46 where the data clearly indicate stall. The plateau in the calculation on the suction surface, $x/c \approx .15$, seems to indicate a vortex being initiated. Furthermore, the calculated maximum suction peak at $\alpha = 19.5°$, Fig. 46, is considerably less than that at $\alpha = 17.7°$, Fig. 45. Based upon the plateau and the drop in suction peak, the calculated distribution at 19.5° appears to be beginning the stall process. This agrees with the normal force and moment coefficients of Figs. 41 and 42. The data at 19.5° is presented with the calculation at $\alpha = 19.9°$, $\dot{\alpha} > 0$ in Fig. 47. Although these are at different values of α, they represent pressure distributions at approximately the same incremental time after stall is initiated; distributions are remarkably similar. Figures 45-47 indicate that although the calculation predicts stall to occur after the measured incidence, once stall occurs the calculated and measured pressure distributions become quite similar. The major discrepancy in the calculated and measured values may lie in the prediction of vortex initiation. This in turn is influenced by turbulence and transition modelling.

Comparisons over the downstroke are given in Figs. 48-50. Obviously, the basic trends are in agreement as a strong qualitative comparison is shown between the calculation and the measured data. Overall, the detailed pressure distributions show good agreement with data and present a more favorable comparison than would appear from the integrated coefficients presented in Figs. 41 and 42. Although surface pressure comparisons obviously do not represent the entire story, these results indicate substantial agreement between calculation and measurement for this very difficult test case.

Velocity vector plots and vorticity contour plots are presented in Figs. 51-54. The results are qualitatively similar to those obtained for previous cases. During much of the upstroke, the velocity field remains well behaved and the vorticity is confined to the immediate region of the airfoil surface. However, near α_{max} the flow field changes dramatically as a large clockwise vortex appears on the suction surface. This is evident in both the vector plot, Fig. 51 and the vorticity plot Fig. 54. Also, note the appearance of the trailing edge counterclockwise vorticity. This phenomenon has been noted and discussed in detail by Robinson and Luttges in a study of airfoils in pitch (Ref. 74). By $\alpha = 18.3°$, $\dot{\alpha} < 0$ the leading edge vortex has clearly broken away and the trailing edge vortex of opposite sign has increased in size and is moving somewhat upstream. This is demonstrated more clearly in the vorticity contour plot. By $\alpha = 16.5°$, $\dot{\alpha} < 0$ the vortices are tending to interact and begin to move downstream. This process also has been discussed by Robinson and Luttges. During the initial portion of the downstroke the flow is a very complex one with interacting shed vortices of opposite sense. The grid used concentrates resolution near the airfoil; however, during this portion of the downstroke, the complex vortex interaction occurs in a region removed from the airfoil where grid resolution is relatively coarse. The calculation encountered stability problems which almost surely could have been solved by increased resolution in this region. However, generation of such a grid and the subsequent calculation was beyond the scope of the present effort and, therefore, the problem was addressed by increasing the value of σ to 0.5 over a portion of the downstroke as shown in Figs. 41 and 42. Finally, by $\alpha = 9.5°$, $\dot{\alpha} < 0$ the flow has fully recovered.

CONCLUSIONS

A numerical procedure for calculating steady and unsteady airfoil flow fields has been developed, demonstrated and documented under the present contract effort. The procedure solves the full time-dependent, compressible Navier-Stokes equations via an alternating direction implicit (ADI) method. The calculations are performed on a highly stretched grid which places the first grid point off the airfoil in the viscous sublayer. No slip conditions are applied at solid boundaries. The calculation has been run extensively with a mixing length turbulence model. Although not detailed in the present report, calculations have also been run with a two equation model for an NACA 0012 airfoil at 6° incidence. The procedure is capable of calculating steady solutions using a matrix preconditioning technique which allows rapid convergence over a Mach number range between virtually incompressible and transonic. Unsteady flows which require transient accuracy, can be made for $M > 0.15$.

The procedure has been used for several calculations including steady flows about an NACA 0012 airfoil at zero and modest incidence and flow about an NACA 4412 airfoil at modest to high incidence. In all cases excellent agreement between calculated and measured pressure distributions was shown. High incidence unsteady calculations were made for an NACA 0012 airfoil at 19° which showed good agreement with available data. Calculations of an airfoil in pitch below the stall angle also showed good agreement with data. Finally, a calculation was made for an airfoil in deep dynamic stall, $4° \leq \alpha \leq 20°$. This represents a very difficult case which contains dynamic effects, large scale separation and multiple interacting shed vortices. Considering the difficulty of the case, the agreement between calculated and measured pressure distribution was very good.

In regard to boundary layer velocity profiles, the only comparison considered under this effort focused upon suction surface boundary layer on the aft section of a NACA 4412 airfoil. The calculated profiles agreed reasonably well with those measured, however, some discrepancies were apparent. Based upon other efforts at SRA the reason for the discrepancy appears to be due to the calculated transition location and prediction of transition location remains a subject of current investigation.

The calculation procedure gives very rapid convergence for cases in which a steady flow is sought. For the range of Mach numbers considered, $.01 \leq M_\infty \leq .5$ convergence is obtained within 70 time steps independent of M_∞. It is anticipated that this convergence property would remain through the transonic region. The present code is a scalar code which requires 15 secs/time step for 5600 grid points on the CYBER 203. This translates into approximately 1000 secs/converged solution. Further code speed-up could reduce this run time by a factor of 10-20. For unsteady flow where transients must be resolved between 400 and 700 time steps are required per cycle.

In summation, the code developed represents a powerful tool for calculating steady and unsteady airfoil flow fields. The calculations run to date indicate good agreement with pressure data even for the very demanding dynamic stall case. Agreement with velocity profile data although reasonable may require further efforts concentrating upon turbulence and transition modelling.

REFERENCES

1. McCroskey, W.J. and Philippe, J.J.: Unsteady Viscous Flow on Oscillating Airfoils, AIAA Paper 74-182, 1974.

2. McCroskey, W.J., Carr, L.W. and McAlister, K.W.: Dynamic Stall Experiments on Oscillating Airfoils, AIAA Journal, Vol. 14, No. 1, January 1976, pp. 57-63.

3. Parker, A.G.: Force and Pressure Measurements on an Airfoil Oscillating through Stall, J. Aircraft, Vol. 13, No. 10, October 1976, pp. 823-827.

4. Proceedings of the AGARD Conference on Unsteady Aerodynamics, AGARD CP-227, September 1977.

5. Saxena, L.S., Fejer, A.A. and Morkovin, M.V.: Features of Unsteady Flows Over Airfoils. Proceedings of AGARD Conference on Unsteady Aerodynamics, September 1977.

6. Philippe, J.J.: Le Decrochage Dynamique. Un Example D'Interaction Forte Entre Ecoulements Visqueux Et Non-Visqueux. Proceedings of AGARD Conference on Unsteady Aerodynamics, September 1977.

7. McCroskey, W.J.: Some Current Research on Unsteady Fluid Dynamics - 1976 Freeman Scholar Lecture, J. Fluids Eng., Vol. 99, March 1977, pp. 8-39.

8. Carta, F.O.: A Comparison of the Pitching and Plunging Response of an Oscillating Airfoil, NASA CR-3172, 1979.

9. Kreskovsky, J.P., Shamroth, S.J. and Briley, W.R.: A Numerical Study of the Unsteady Leading Edge Separation Bubble on an Oscillating Airfoil. Computer Methods in Applied Mechanics and Engineering, Vol. 11, No. 1, April 1977, pp. 39-56.

10. Shamroth, S.J. and Kreskovsky, J.P.: A Weak Interaction Study of the Viscous Flow About Oscillating Airfoils, NASA CR-132425, 1974.

11. Briley, W.R. and McDonald, H.: Numerical Prediction of Incompressible Separation Bubbles, J. Fluid Mech., Vol. 69, Part 4, 1975, pp. 631-656.

12. Mehta, U.B. and Lavan, Z.: Starting Vortex, Separation Bubble and Stall: A Numerical Study of Laminar Unsteady Flow about an Airfoil, J. Fluid Mech., Vol. 67, 1975, pp. 227-256.

13. Lugt, H.J. and Haussling, H.J.: Laminar Flow about an Abruptly Accelerated Elliptic Cylinder at 45° Incidence, J. Fluid Mech., Vol. 65, 1974, pp. 711-734.

14. Mehta, U.B.: Dynamic Stall of an Oscillating Airfoil, Proceedings of AGARD Conference on Unsteady Aerodynamics, September 1977.

15. Wu, J.C. and Sampath, S.: A Numerical Study of Viscous Flow About an Airfoil. AIAA Paper 76-337, 1976.

16. Wu, J.C., Sampath, S. and Sankar, N.L.: A Numerical Study of Viscous Flows Around Airfoils, Proceedings of AGARD Conference on Unsteady Aerodynamics, September 1977.

17. Wu, J.C. and Thompson, J.F.: Numerical Solutions of Time-Dependent Incompressible Navier-Stokes Equations Using an Integro-Differential Formulation, Computers and Fluids, Vol. 1, 1973, pp. 197-215.

18. Kinney, R.B. and Cielak, Z.M.: Analysis of Unsteady Viscous Flow Past an Airfoil: Part I - Theoretical Development, AIAA Journal, Vol. 15, No. 12, December 1977, pp. 1714-1719.

19. Cielak, Z.M. and Kinney, R.B.: Analysis of Unsteady Viscous Flow Past an Airfoil: Part II - Numerical Formulation and Results, AIAA Journal, Vol. 16, No. 2, February 1978, pp. 105-110.

20. Lugt, H.J. and Haussling, H.J.: The Acceleration of Thin Cylindrical Bodies in a Viscous Fluid, Journal of Appl. Mech., Vol. 45, 1978, pp. 1-6.

21. Thames, F.C., Thompson, J.F., Mastin, C.W. and Walker, R.L.: Numerical Solutions for Viscous and Potential Flow about Arbitrary Two-Dimensional Bodies Using Body Fitted Coordinate Systems, Journal of Comp. Phys., Vol. 24, 1977, pp. 245-273.

22. Hodge, J.K. and Stone, A.L.: Numerical Solution for Airfoils Near Stall in Optimized Body Fitted Curvilinear Coordinates, AIAA Paper 78-284, 1978.

23. Verhoff, A.: Numerical Solution of Subsonic Inviscid Interacting Flows, AFFDL-TR-76-64, July 1976.

24. MacCormack, R.W.: The Effect of Viscosity in Hypervelocity Impact Cratering, AIAA Paper No. 69-354, 1967.

25. Diewert, G.S.: Recent Computation of Viscous Effects in Transonic Flow, Proceedings of the Fifth International Conference on Numerical Methods in Fluid Dynamics, Springer-Verlag, New York, 1976.

26. Levy, L.L., Jr.: An Experimental and Computational Investigation of the Steady and Unsteady Transonic Flow Fields about an Airfoil in a Solid Wall Test Channel, AIAA Paper 77-678, 1977.

27. MacCormack, R.W.: An Efficient Explicit-Implicit Characteristic Method for Solving the Compressible Navier-Stokes Equations, SIAM-AMS Proceedings of the Symposium on Computational Fluid Dynamics, 1977.

28. Gibeling, H.J., Shamroth, S.J. and Eiseman, P.R.: Analysis of Strong-Interaction Dynamic Stall for Laminar Flow on Airfoils. NASA CR-2969, April 1978.

29. Briley, W.R. and McDonald, H.: Solution of the Multidimensional Compressible Navier-Stokes Equations by a Generalized Implicit Method. J. Comp. Physics, Vol. 24, No. 4, August 1977, p. 372.

30. Sankar, N.L. and Tassa, Y.: Reynolds Number and Stability Effects on Dynamic Stall of an NACA 0012 Airfoil. AIAA Paper No. 80-0010, 1980.

31. El Refaee, M.M., Wu, J.C. and Likoudis, C: Solution of the Compressible Navier-Stokes Equations Using the Integral Method. AIAA Journal, Vol. 20, March 1982, pp. 356-362.

32. Steger, J.L.: Implicit Finite Difference Simulation of Flow About Arbitrary Two-Dimensional Geometries. AIAA Journal, Vol. 16, 1978, pp. 679-686.

33. Thompson, J.F., Thames, F.C. and Mastin, C.W.: Automatic Numerical Generation of Body Fitted Curvilinear Coordinate System for Field Containing Any Number of Arbitrary Two-Dimensional Bodies. J. Comp. Physics, Vol. 15, 1974, pp. 299-319.

34. Shamroth, S.J. and Gibeling, H.J.: A Compressible Solution of the Navier-Stokes Equations for Turbulent Flow About an Airfoil. NASA CR-3183, 1979. (See also AIAA Paper 79-1543).

35. Shamroth, S.J. and Gibeling, H.J.: Analysis of Turbulent Flow About an Isolated Airfoil Using a Time-Dependent Navier-Stokes Procedure. Presented at AGARD Conference on Boundary Layer Effects on Unsteady Airfoils. AGARDograph 296, 1980.

36. Shamroth, S.J.: A Turbulent Flow Navier-Stokes Analysis for an Airfoil Oscillating in Pitch. IUTAM Symposium on Turbulent Shear Flows, Springer-Verlag, New York, 1981.

37. Tassa, Y. and Sankar, N.L.: Dynamic Stall of an Oscillating Airfoil in Turbulent Flow Using Time-Dependent Navier-Stokes Solver. IUTAM Symposium on Turbulent Shear Flows. Springer-Verlag, New York 1981.

38. Sankar, N.L. and Tang, W.: Numerical Solution of Unsteady Viscous Flow Past Rotor Sections, AIAA Paper 85-0129, 1985.

39. Haussling, H.J.: Body Fitted Coordinates for Accurate Numerical Solution of Multibody Flow Problems. Journal of Comp. Phys., Vol. 30, 1979, pp. 107-124.

40. Eiseman, P.R.: Coordinate Generation with Precise Controls over Mesh Properties. J. Comp. Physics, Vol. 47, 1982, pp. 331-351.

41. McVittie, G.C.: A Systematic Treatment of Moving Axes in Hydrodynamics. Proceedings of the Royal Society A, 1965, pp. 285-300.

42. Walkden, F.: The Equations of Motion of a Viscous, Compressible Gas Referred to an Arbitrarily Moving Coordinate System. Royal Aircraft Establishment, Technical Report No. 66140, April 1966.

43. Thomas, P.D. and Lombard, C.K.: Geometric Conservation Law and Its Application to Flow Computations on Moving Grids. AIAA Journal, Vol. 17, 1979, pp. 1030-1037.

44. Hindman, R.G.: Generalized Coordinate Forms of Governing Fluid Equations and Associated Geometrically Induced Errors. AIAA Journal, 20, October 1982, pp. 1359-1367.

45. Shamroth, S.J., McDonald, H. and Briley, W.R.: Prediction of Cascade Flow Fields Using the Averaged Navier-Stokes Equations. Journal of Engineering for Gas Turbines and Power. Vol. 106, April 1984, pp. 383-390.

46. Shamroth, S.J., McDonald, H. and Briley, W.R.: A Navier-Stokes Analysis for Transonic Flow Through a Cascade, Final Report under Contract N00019-79-C-0558, SRA Rpt. R81-920007-F, 1962.

47. Shamroth, S.J., McDonald, H. and Briley, W.R.: Application of a Navier-Stokes Analysis to Transonic Cascade Flow Fields. ASME Paper No. 82-GT-235, 1982.

48. Weinberg, B.C., Yang, R.J., McDonald, H. and Shamroth, S.J.: Calculation of Two- and Three-Dimensional Transonic Cascade Flow Fields. ASME Paper 85-GT-66, 1985.

49. Shamroth, S.J.: Calculation of Steady and Oscillating Airfoil Flow Fields via the Navier-Stokes Equations. AIAA Paper 84-0525, 1984.

50. Schlichting, H.: Boundary Layer Theory, McGraw-Hill, New York, c. 1960.

51. Launder, B.E. and Spalding, D.B.: The Numerical Computation of Turbulent Flows. Computer Methods in Applied Mechanics and Engineering, Vol. 3, 1974, pp. 269-289.

52. Launder, B.E. and Spalding, D.B.: Mathematical Models of Turbulence, Academic Press, New York, 1972.

53. Jones, W.P. and Launder, B.E.: The Prediction of Laminarization with a Two-Equation Model of Turbulence, International Journal of Heat and Mass Transfer, Vol. 15, 1972, pp. 301-314.

54. Jones, W.P. and Launder, B.E.: The Calculation of Low Reynolds Number Phenomena with a Two-Equation Model of Turbulence, International Journal of Heat and Mass Transfer, Vol. 16, 1973, pp. 1119-1130.

55. Lindemuth, L. and Killeen, J.: Alternating Direction Implicit Techniques for Two-Dimensional Magnetohydrodynamic Calculations. Journal of Computational Physics, Vol. 13, 1979, pp. 181-208.

56. Briley, W.R. and McDonald, H.: On the Structure and Use of Linearized Block Implicit Schemes. Journal of Computational Physics, Vol. 34, January 1980, pp. 54-73.

57. Douglas, J. and Gunn, J.E.: A General Formulation of Alternating Direction Methods. Numerische Math., Vol. 6, 1964, pp. 428-453.

58. Briley, W.R., Buggeln, R.C. and McDonald, H.: Computation of Laminar and Turbulent in 90 Degree Square Duct and Pipe Bends Using the Navier-Stokes Equations. Final Report under Contract N00014-81-C-0377, SRA Rpt. R82-920009-F, 1982.

59. Briley, W.R. and McDonald, H.: Computation of Three-Dimensional Horseshoe Vortex Flow Using the Navier-Stokes Equations. Seventh International Conference on Numerical Methods in Fluid Dynamics, 1980.

60. Shamroth, S.J., Gibeling, H.J. and McDonald, H.: A Navier-Stokes Solution for Laminar and Turbulent Flow Through a Cascade of Airfoils. AIAA Paper 80-1426, 1980.

61. McDonald, H., Shamroth, S.J. and Briley, W.R.: Transonic Flows with Viscous Effects. Transonic, Shock and Multidimensional Flows: Advances in Scientific Computing. Academic Press, New York, 1982.

62. Liu, N.-S., Shamroth, S.J. and McDonald, H.: Numerical Solutions of Navier-Stokes Equations for Compressible Turbulent Two/Three Dimensional Flows in the Terminal Shock Region of an Inlet/Diffuser. NASA CR-3723, 1983.

63. Young, W.H., Jr., Meyers, J.F. and Hoad, D.R.: A Laser Velocimeter Flow Survey Above a Stalled Wing, NASA Technical Paper 1266, AVRADCOM Technical Report 78-50, 1978.

64. Grey, L. and Liiva, J.: Two-Dimensional Tests of Airfoils Oscillating Near Stall. Volume II: Data Report. USAAVLABS Rpt. 68-13B, 1968.

65. Coles, D. and Wadcock, A.J.: Flying Hot Wire Study of Flows Past an NACA 4412 Airfoil at Maximum Lift. AIAA Journal, Vol. 17, April 1978, pp. 321-329.

66. McDonald, H. and Briley, W.R.: Computational Fluid Dynamics Aspects of Internal Flows. AIAA Paper 79-1445, 1979.

67. Briley, W.R., McDonald, H. and Shamroth, S.J.: A Low Mach Number Euler Formulation and Application to Time Iterative Schemes. AIAA Journal, Vol. 21, 1983, pp. 1467-1469.

68. Abbott, I.H. and van Doenhoff, A.E.: Theory of Wing Sections, Dover Publ., Inc., New York,c.1959.

69. Liu, N.-S., Shamroth, S.J. and McDonald, H.: Numerical Solution of the Navier-Stokes Equations for Compressible Turbulent Two/Three Dimensional Flows in the Terminal Shock Region of an Inlet/Diffuser. AIAA Paper 83-1892, 1983.

70. St. Hilaire, A.O., Carta, F.O., Fink, M.R. and Jepson, W.D.: The Influence of Sweep on the Aerodynamic Loading of an Oscillating, NACA 0012 Airfoil. Volume I - Technical Report, NASA CR-3092, 1979.

71. St. Hilaire, A.O. and Carta, F.O.: Analysis of Unswept and Swept Wing Chordwise Pressure Data from an Oscillating NACA 0012 Airfoil Experiment. Volume I - Technical Report, NASA CR-3567, 1983.

72. Gregory, N. and O'Reilly, C.L.: Low Speed Aerodynamic Characteristics of NACA 0012 Airfoil Section, Including the Effects of Upper Surface Roughness Simulating Hoarfrost. Aero Report 1308, National Physics Laboratory, 1970.

73. St. Hilaire, A.O. and Carta, F.O.: Analysis of Unswept and Swept Wing Chordwise Pressure Data from an Oscillating NACA 0012 Airfoil Experiment, Vol. II Data Report, NASA CR-165927, 1983.

74. Robinson, M.C. and Luttges, M.W.: Unsteady Flow Separation and Attachment Induced by Pitching Airfoils. AIAA Paper No. 83-0131, 1983.

75. Beam, R.M. and Warming, R.F.: An Implicit Factored Scheme for the Compressible Navier-Stokes Equations. AIAA Journal, Vol. 16, No. 4, April 1978, pp. 393-402.

76. Beam, R.M. and Warming, R.F.: An Implicit Finite Difference Algorithm for Hyperbolic Systems in Conservation Law Form. Journal of Computational Physics, Vol. 22, 1976, pp. 87-140.

77. Beam, R.M. and Warming, R.F.: Alternating Direction Implicit Methods for Parabolic Equations with a Mixed Derivative. SIAM J. Sci. Stat. Comp., Vol. 1, 1980, pp. 131-157.

APPENDIX B - SOLUTION PROCEDURE [58]

Background

The solution procedure employs a consistently-split linearized block implicit (LBI) algorithm which has been discussed in detail in [29, 56]. There are two important elements of this method:

(1) the use of a noniterative formal time linearization to produce a fully-coupled linear multidimensional scheme which is written in "block implicit" form; and

(2) solution of this linearized coupled scheme using a consistent "splitting" (ADI scheme) patterned after the Douglas-Gunn [57] treatment of scalar ADI schemes.

The method is thus referred to as a split linearized block implicit (LBI) scheme. The method has several attributes:

(1) the noniterative linearization is efficient;

(2) the fully-coupled linearized algorithm eliminates instabilities and/or extremely slow convergence rates often attributed to methods which employ ad hoc decoupling and linearization assumptions to identify nonlinear coefficients which are then treated by lag and update techniques;

(3) the splitting or ADI technique produces an efficient algorithm which is stable for large time steps and also provides a means for convergence acceleration for further efficiency in computing steady solutions;

(4) intermediate steps of the splitting are consistent with the governing equations, and this means that the "physical" boundary conditions can be used for the intermediate solutions. Other splittings which are inconsistent can have several difficulties in satisfying physical boundary conditions [56].

(5) the convergence rate and overall efficiency of the algorithm are much less sensitive to mesh refinement and redistribution than algorithms based on explicit schemes or which employ ad hoc decoupling and linearization assumptions. This is important for accuracy and for computing turbulent flows with viscous sublayer resolution; and

(6) the method is general and is specifically designed for the complex systems of equations which govern multiscale viscous flow in complicated geometries. This same algorithm was later considered by Beam and Warming [75], but the ADI splitting was derived by approximate factorization instead of the Douglas-Gunn procedure. They refer to the algorithm as a "delta form" approximate factorization scheme. This scheme replaced an earlier non-delta form scheme [76], which has inconsistent intermediate steps.

Spatial Differencing and Artificial Dissipation

The spatial differencing procedures used are a straightforward adaption of those used in [29] and elsewhere. Three-point central difference formulas are used for spatial derivatives, including the first-derivative convection and pressure gradient terms. This has an advantage over one-sided formulas in flow calculations subject to "two point" boundary conditions (virtually all viscous or subsonic flows), in that all boundary conditions enter the algorithm implicitly. In practical flow calculations, artificial dissipation is usually needed and is added to control high-frequency numerical oscillations which otherwise occur with the central-difference formula.

In the present investigation, artificial (anisotropic) dissipation terms of the form

$$\sum_j \frac{d_j}{h_j^2} \frac{\partial^2 u_k}{\partial x_j^2} \tag{1}$$

are added to the right-hand side of each (k-th) component of the momentum equation, where for each coordinate direction x_j, the artificial diffusivity d_j is positive and is chosen as the larger of zero and the local quantity μ_e (σ $Re_{\Delta x}$-1)/Re. Here, the local cell Reynolds number $Re_{\Delta xj}$ for the j-th direction is defined by

$$Re_{\Delta x_j} = Re \left|\rho u_j\right| \Delta x_j / \mu_e \tag{2}$$

This treatment lowers the formal accuracy to 0 (Δx), but the functional form is such that accuracy in representing physical shear stresses in thin shear layers with small normal velocity is not seriously degraded. This

latter property follows from the anisotropic form of the dissipation and the combination of both small normal velocity and small grid spacing in thin shear layers.

Split LBI Algorithm

Linearization and Time Differencing

The system of governing equations to be solved consists of three/four equations: continuity and two/three components of momentum equation in three/four dependent variables: ρ, u, v, w. Using notation similar to that in [29], at a single grid point this system of equations can be written in the following form:

$$\partial H(\phi)/\partial t = D(\phi) + S(\phi) \tag{3}$$

where ϕ is the column-vector of dependent variables, H and S are column-vector algebraic functions of ϕ, and D is a column vector whose elements are the spatial differential operators which generate all spatial derivatives appearing in the governing equation associated with that element.

The solution procedure is based on the following two-level implicit time-difference approximations of (3):

$$(H^{n+1} - H^n)/\Delta t = \beta(D^{n+1} + S^{n+1}) \quad (1-\beta)\ (D^n + S^n) \tag{4}$$

where, for example, H^{n+1} denotes $H(\phi^{n+1})$ and $\Delta t = t^{n+1} - t^n$. The parameter β ($0.5 \leq \beta \leq 1$) permits a variable time-centering of the scheme, with a truncation error of order $[\Delta t^2, (\beta - 1/2)\ \Delta t]$.

A local time linearization (Taylor expansion about ϕ^n) of requisite formal accuracy is introduced, and this serves to define a linear differential operator L (cf. [29]) such that

$$D^{n+1} = D^n + L^n(\phi^{n+1} - \phi^n) + O(\Delta t^2) \tag{5}$$

Similarly,

$$H^{n+1} = H^n + (\partial H/\partial \phi)^n\ (\phi^{n+1} - \phi^n) + O\ (\Delta t^2) \tag{6}$$

$$S^{n+1} = S^n + (\partial S/\partial \phi)^n\ (\phi^{n+1} - \phi^n) + O\ (\Delta t^2) \tag{7}$$

Eqs. (5-7) are inserted into Eq. (4) to obtain the following system which is linear in ϕ^{n+1}

$$(A - \beta \Delta t\ L^n)\ (\phi^{n+1} - \phi^n) = \Delta t\ (D^n + S^n) \tag{8}$$

and which is termed a linearized block implilcit (LBI) scheme. Here, A denotes a matrix defined by

$$A \equiv (\partial H/\partial \phi)^n - \beta \Delta t \, (\partial S/\partial \phi)^n \tag{9}$$

Eq. (8) has 0 (Δt) accuracy unless $H \equiv \phi$, in which case the accuracy is the same as Eq. (4).

Special Treatment of Diffusive Terms

The time differencing of diffusive terms is modified to accomodate cross-derivative terms and also turbulent viscosity and artificial dissipation coefficients which depend on the solution variables. Although formal linearization of the convection and pressure gradient terms and the resulting implicit coupling of variables is critical to the stability and rapid convergence of the algorithm, this does not appear to be important for the turbulent viscosity and artificial dissipation coefficients. Since the relationship between μ_e and d_j and the mean flow variables is not conveniently linearized, these diffusive coefficients are evaluated explicitly at t^n during each time step. Notationally, this is equivalent to neglecting terms proportional to $\partial \mu_e/\partial \phi$ or $\partial d_j/\partial \phi$ in L^n, which are formally present in the Taylor expansion (5), but retaining all terms proportional to μ_e or d_j in both L^n and D^n.

It has been found through extensive experience that this has little if any effect on the performance of the algorithm. This treatment also has the added benefit that the turbulence model equations can be decoupled from the system of mean flow equations by an appropriate matrix partitioning [56] and solved separately in each step of the ADI solution procedure. This reduces the block size of the block tridiagonal systems which must be solved in each step and thus reduces the computational labor.

In addition, the viscous terms in the present formulation include a number of spatial cross-derivative terms. Although it is possible to treat cross-derivative terms implicitly within the ADI treatment which follows, it is not at all convenient to do so; and consequently, all cross-derivative terms are evaluated explicitly at t^n. For a scalar model equation representing combined convection and diffusion, it has been shown by Beam and Warming [77] that the explicit treatment of cross-derivative terms does not degrade the unconditional stability of the present algorithm. To preserve notational simplicity, it is understood that all cross-derivative terms appearing in L^n are neglected but are

retained in D^n. It is important to note that neglecting terms in L^n has no effect on steady solutions of Eq. (8), since $\phi^{n+1} - \phi^n \equiv 0$, and thus Eq. (8) reduces to the steady form of the equations: $D^n + S^n = 0$. Aside from stability considerations, the only effort of neglecting terms in L^n is to introduce an $0\ (\Delta t)$ truncation error.

Consistent Splitting of the LBI Scheme

To obtain an efficient algorithm, the linearized system (8) is split using ADI techniques. To obtain the split scheme, the multidimensional operator L is rewritten as the sum of three "one-dimensional" sub-operators L_i $(i = 1, 2, 3)$ each of which contains all terms having derivatives with respect to the i-th coordinate. The split form of Eq. (8) can be derived either as in [29, 56] by following the procedure described by Douglas and Gunn [57] in their generalization and unification of scalar ADI schemes, or using approximate factorization. For the present system of equations, the split algorithm is given by

$$(A - \beta\Delta t L_1^n)\ (\phi^* - \phi^n) = \Delta t\ (D^n + S^n) \tag{10a}$$

$$(A - \beta\Delta t L_2^n)\ (\phi^{**} - \phi^n) = A\ (\phi^* - \phi^n) \tag{10b}$$

$$(A - \beta\Delta t L_3^n)\ (\phi^{n+1} - \phi^n) = A\ (\phi^{**} - \phi^n) \tag{10c}$$

where ϕ^* and ϕ^{**} are consistent intermediate solutions. If spatial derivatives appearing in L_i and D are replace by three-point difference formulas, as indicated previously, then each step in Eqs. (10a-c) can be solveby a block-tridiagonal elimination.

Combining Eqs. (10a-c) gives (11)

$$(A - \beta\Delta t L_1^n)\ A^{-1}\ (A - \beta\Delta t L_2^n)\ A^{-1}\ (A - \beta\Delta t L_3^n)\ (\phi^{n+1} - \phi^n) = \Delta t\ (D^n + S^n)$$

which approximates the unsplit scheme (8) to $0\ (\Delta t^2)$. Since the intermediate steps are also consistent approximations for Eq. (8), physical boundary conditions can be used for ϕ^* and ϕ^{**} [29, 56]. Finally, since the L_i are homogeneous operators, it follows from Eqs. (10a-c) that steady solutions have the property that $\phi^{n+1} = \phi^* = \phi^{**} = \phi^n$ and satisfy

$$D^n + S^n = 0 \tag{12}$$

The steady solution thus depends only on the spatial difference approximations used for (12), and does not depend on the solution algorithm itself.

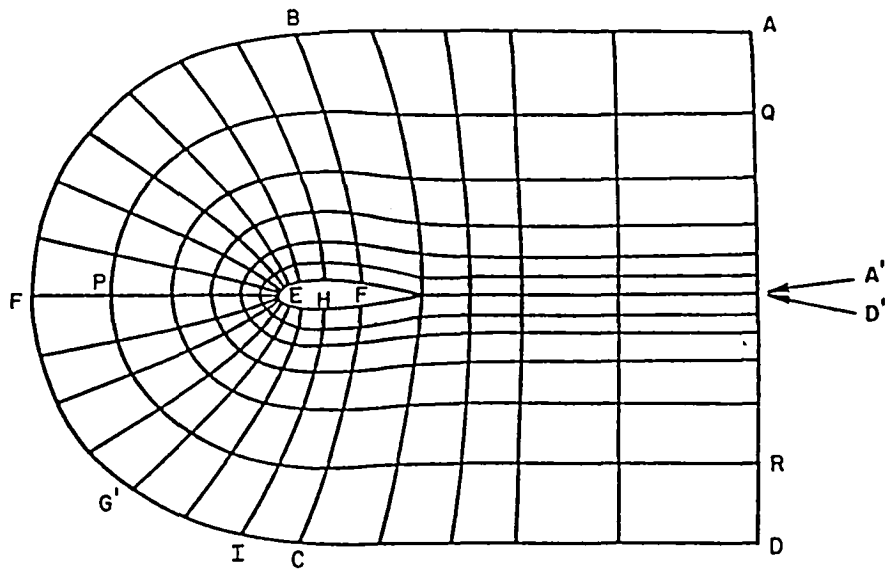

Figure 1 - Sketch of constructive coordinate system.

T = 1.93

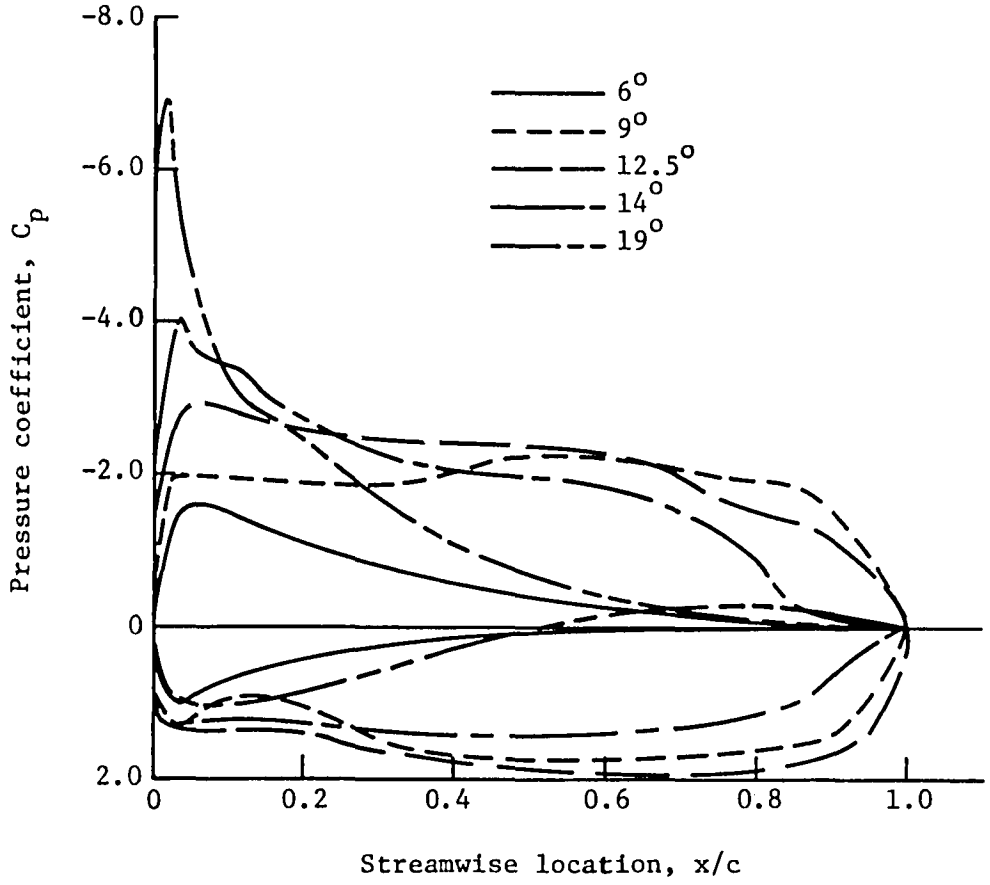

Figure 2 - Pressure coefficient for airfoil in ramp motion.

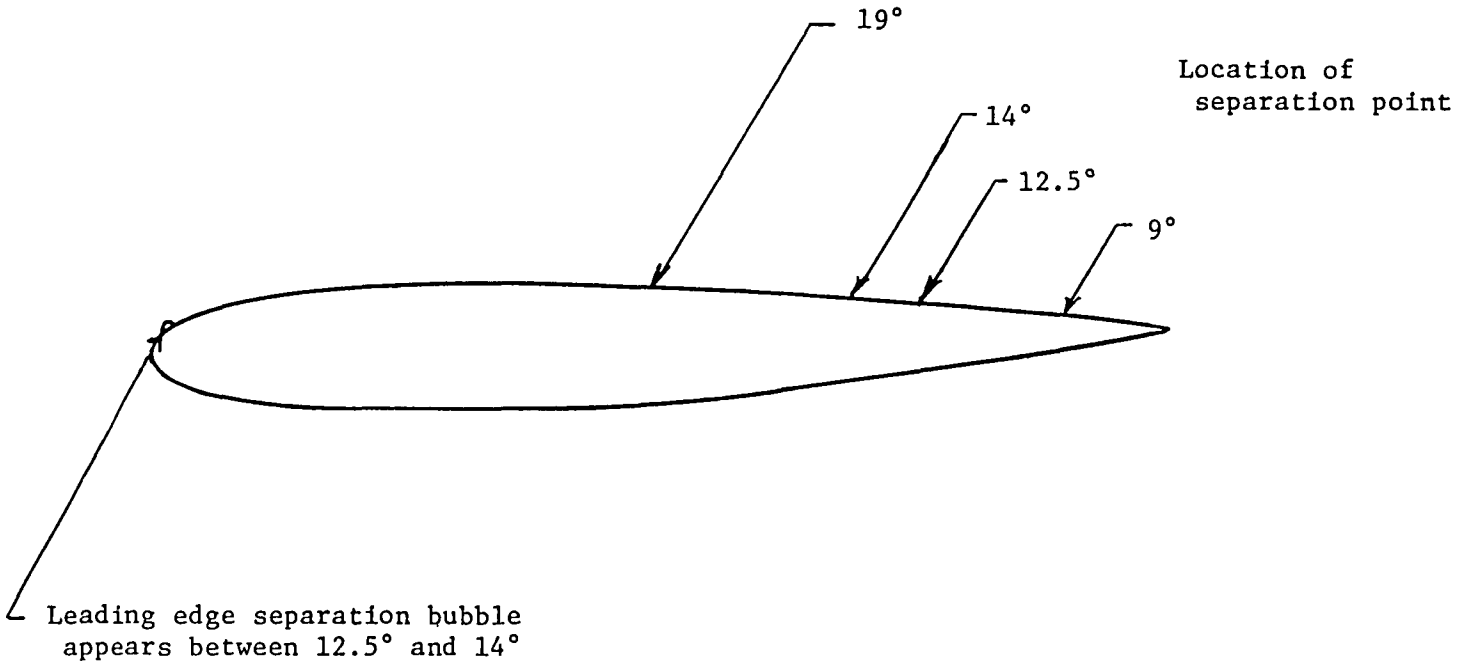

Figure 3 - Location of separation points for airfoil in ramp motion.

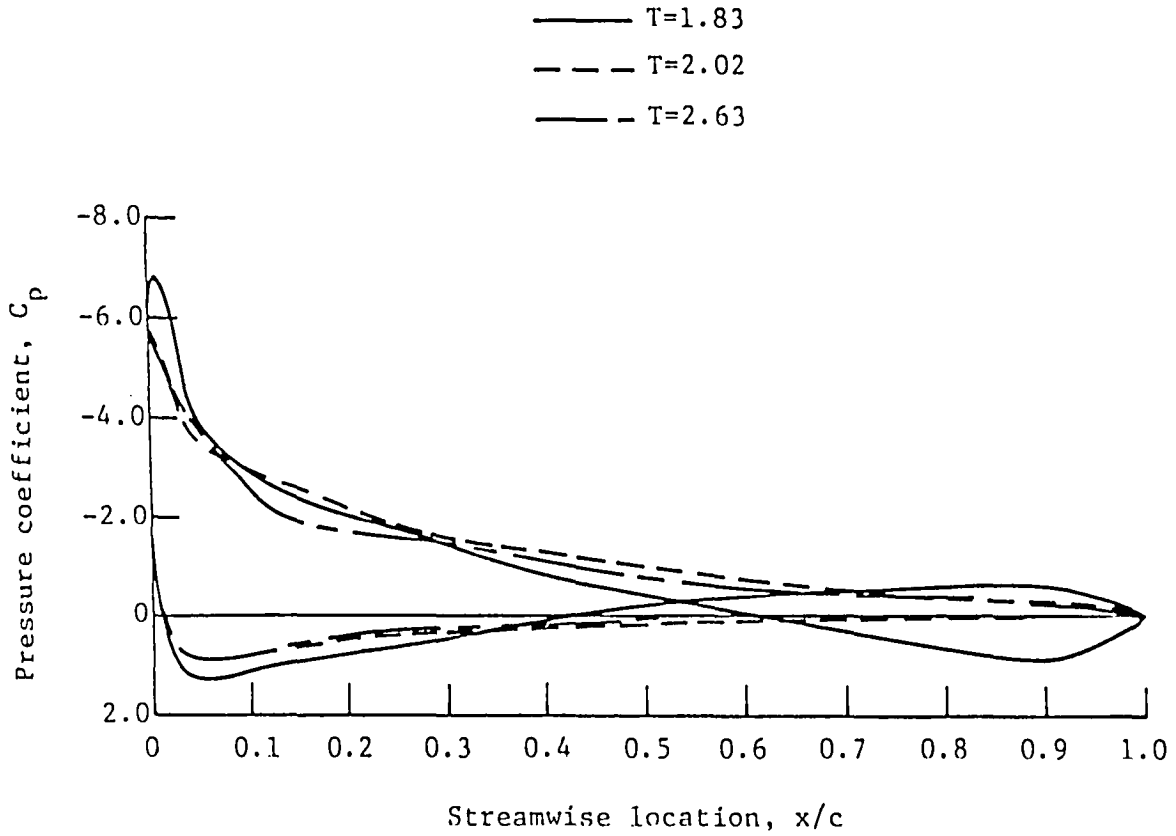

Figure 4 - Pressure distribution for 19^{o} airfoil after cessation of airfoil motion (airfoil motion ceases at T=1.83).

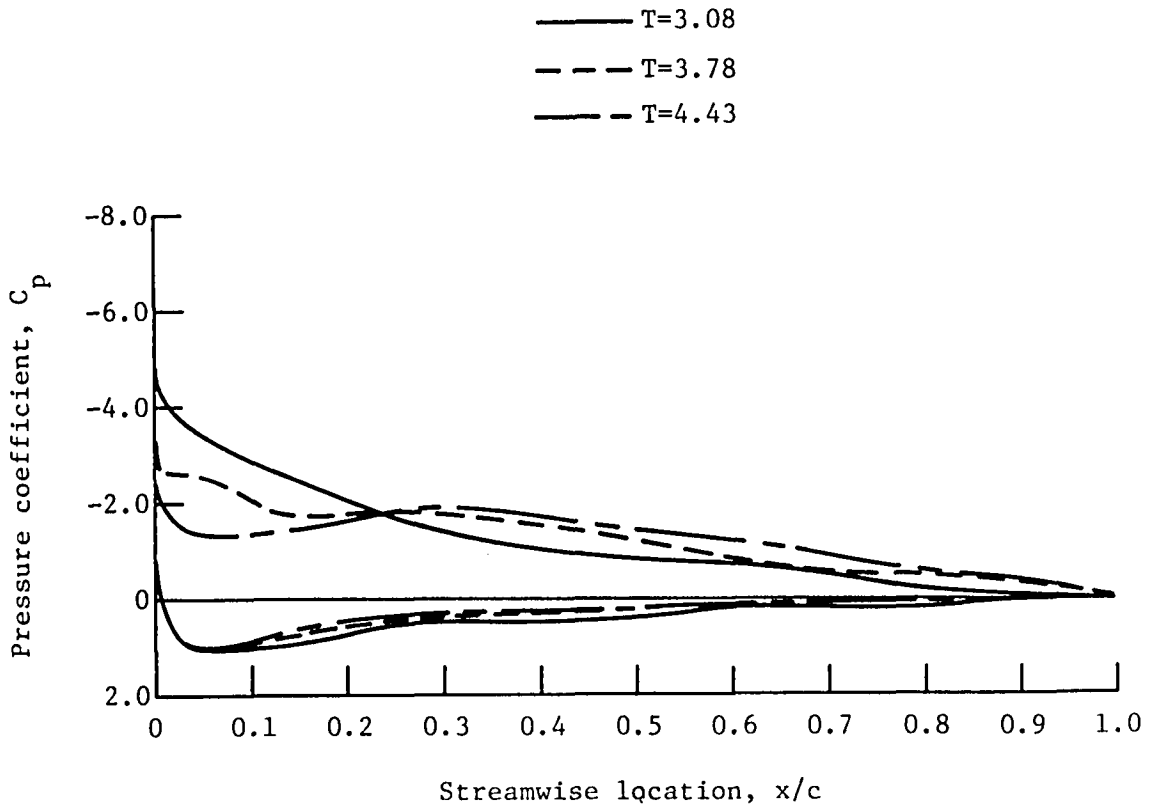

Figure 5 - Pressure distribution for 19^{o} airfoil after cessation of airfoil motion (airfoil motion ceases at T=1.83).

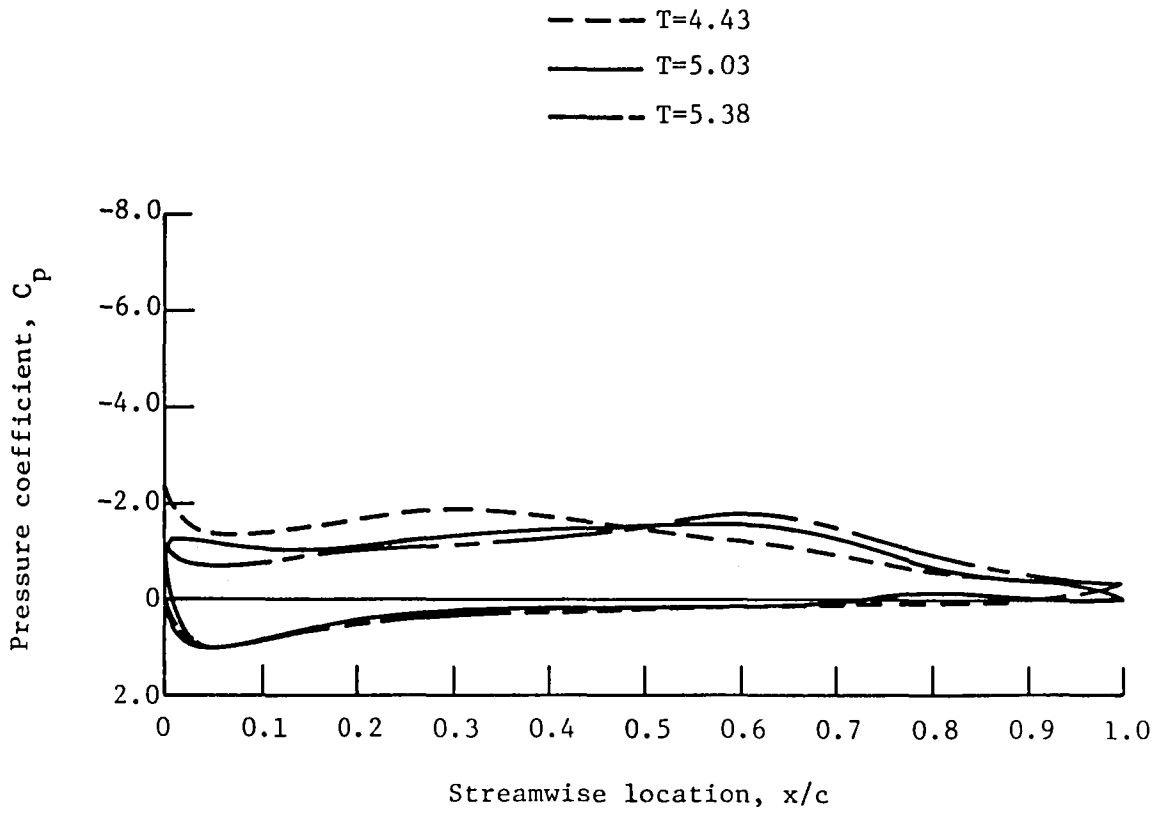

Figure 6 - Pressure distribution for 19^{o} airfoil after cessation of airfoil motion (airfoil motion ceases at T=1.83).

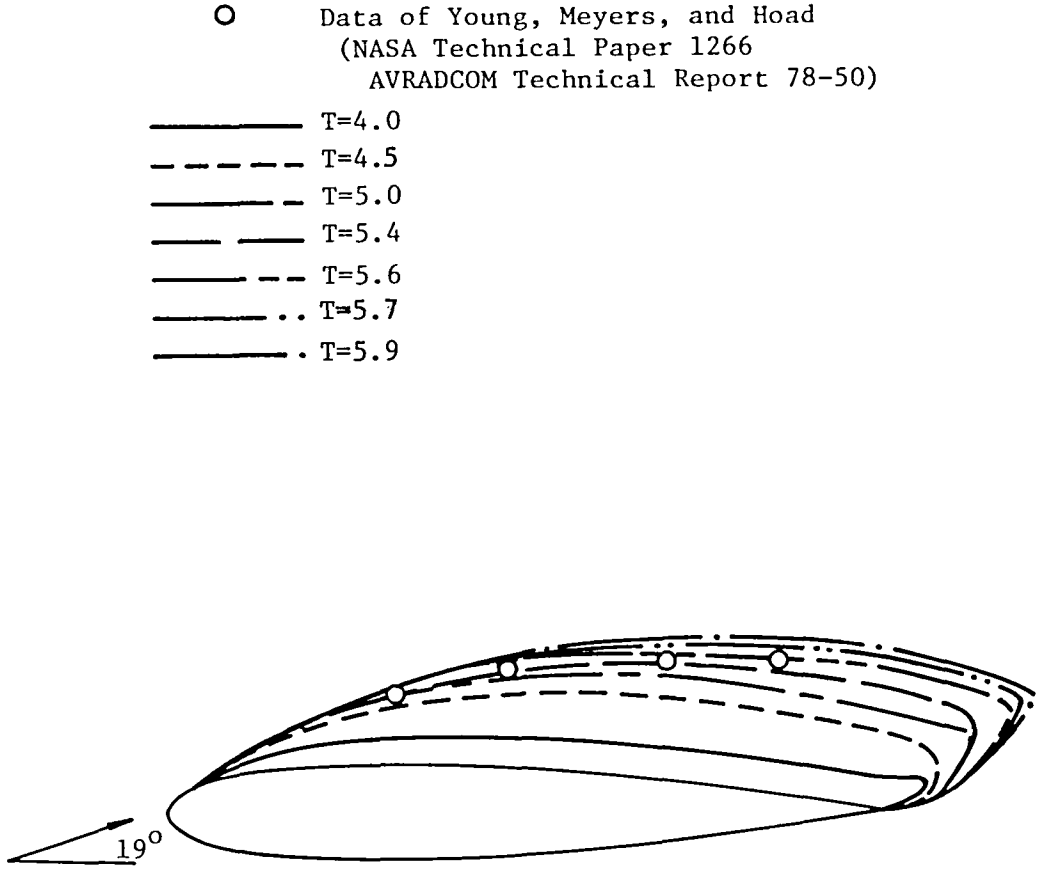

Figure 7 - Development of backflow velocity zone for airfoil at 19°.

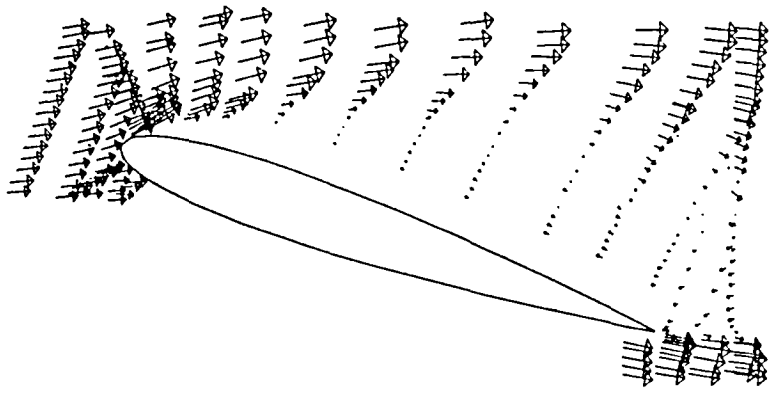

Figure 8 - Experimentally measured velocity field, $\alpha = 19^{o}$.
(Data of Young, Meyers and Hoad)

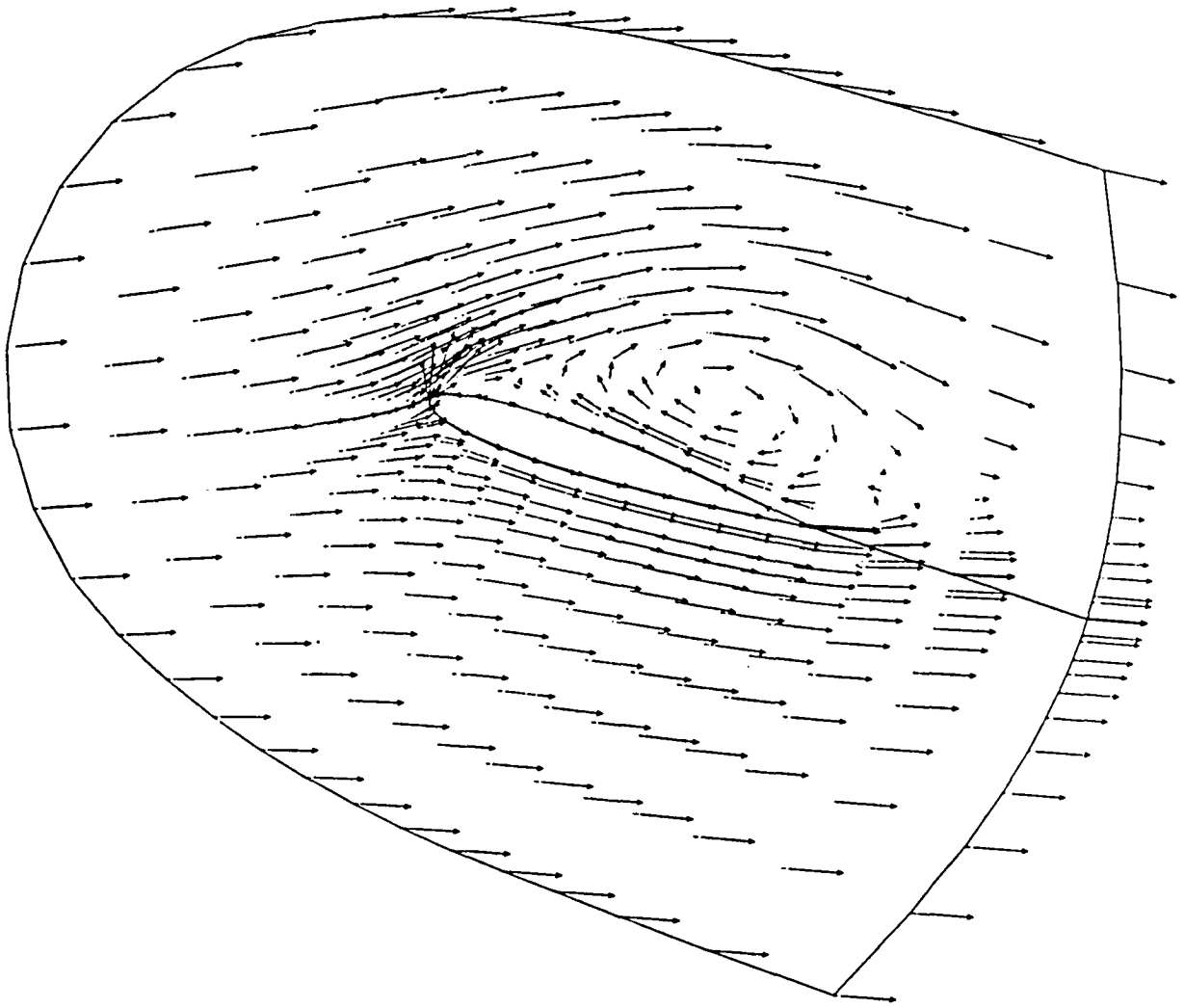

Figure 9 - Computed velocity vector field, $\alpha = 19°$, $t = t_1$.

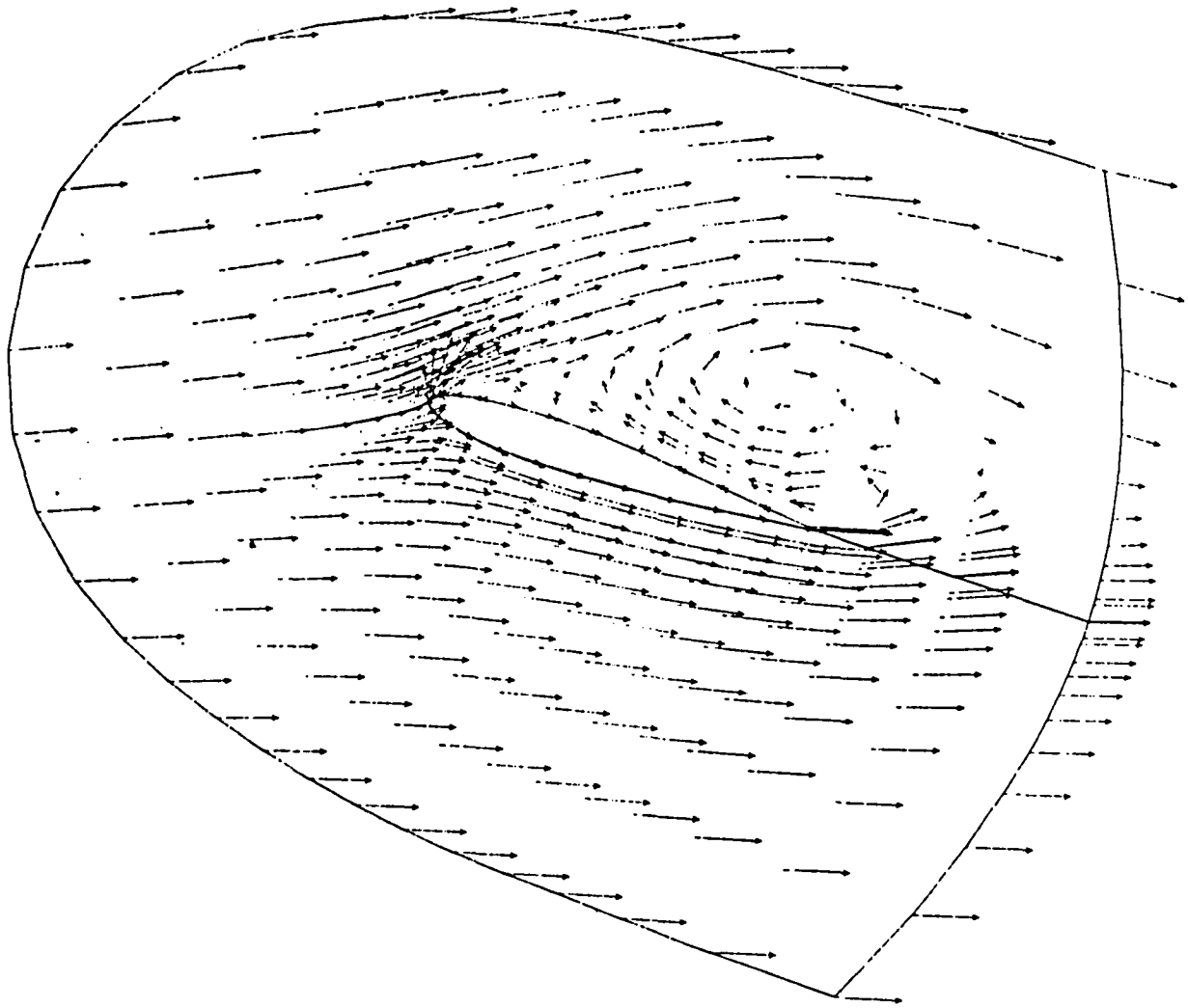

Figure 10 - Computed velocity vector field, $\alpha = 19°$, $t = t_1 + \Delta t$, $\Delta t = 1.0$.

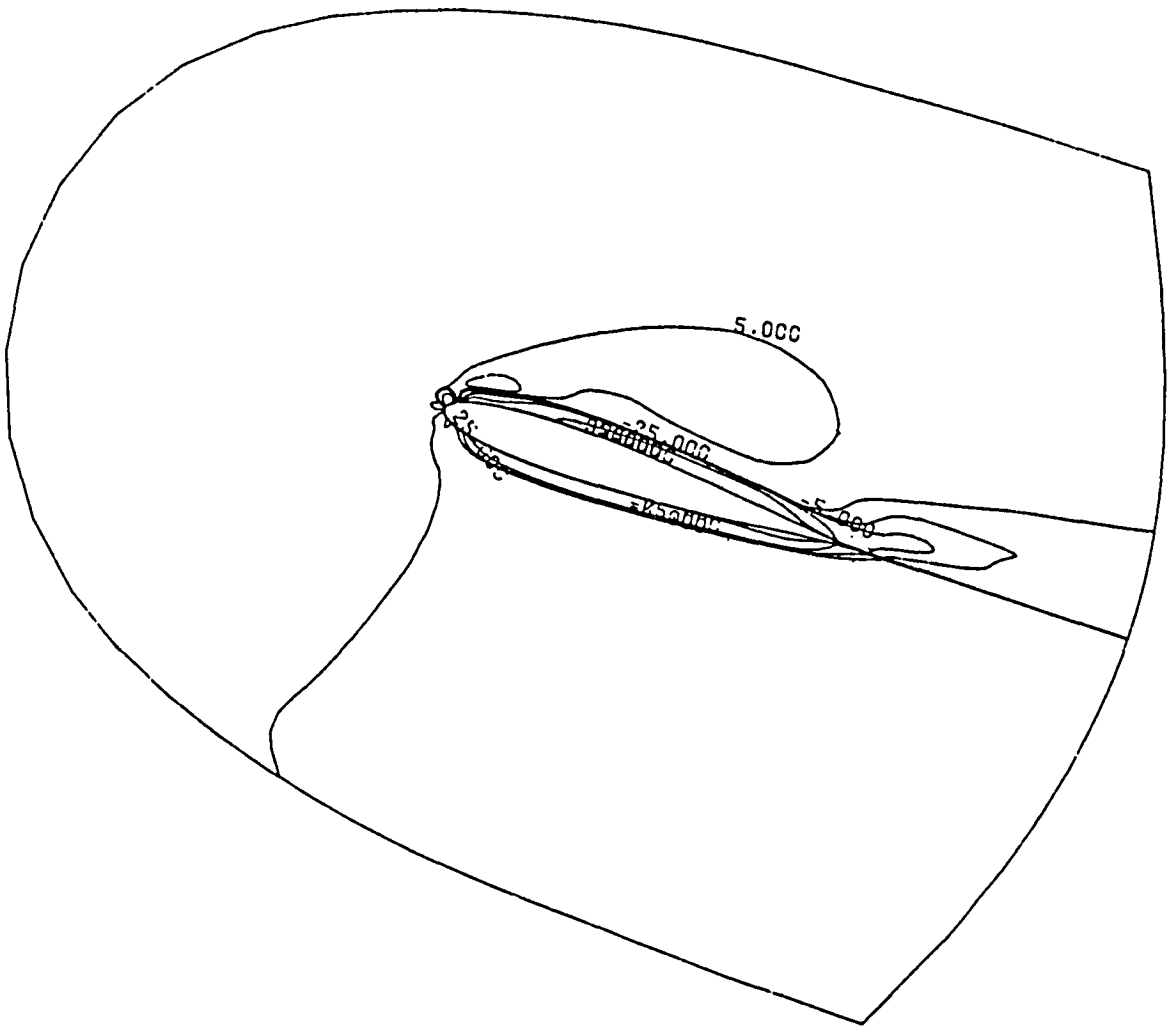

Figure 11 - Vorticity contours, $\alpha = 19°$, $t = t_1$.

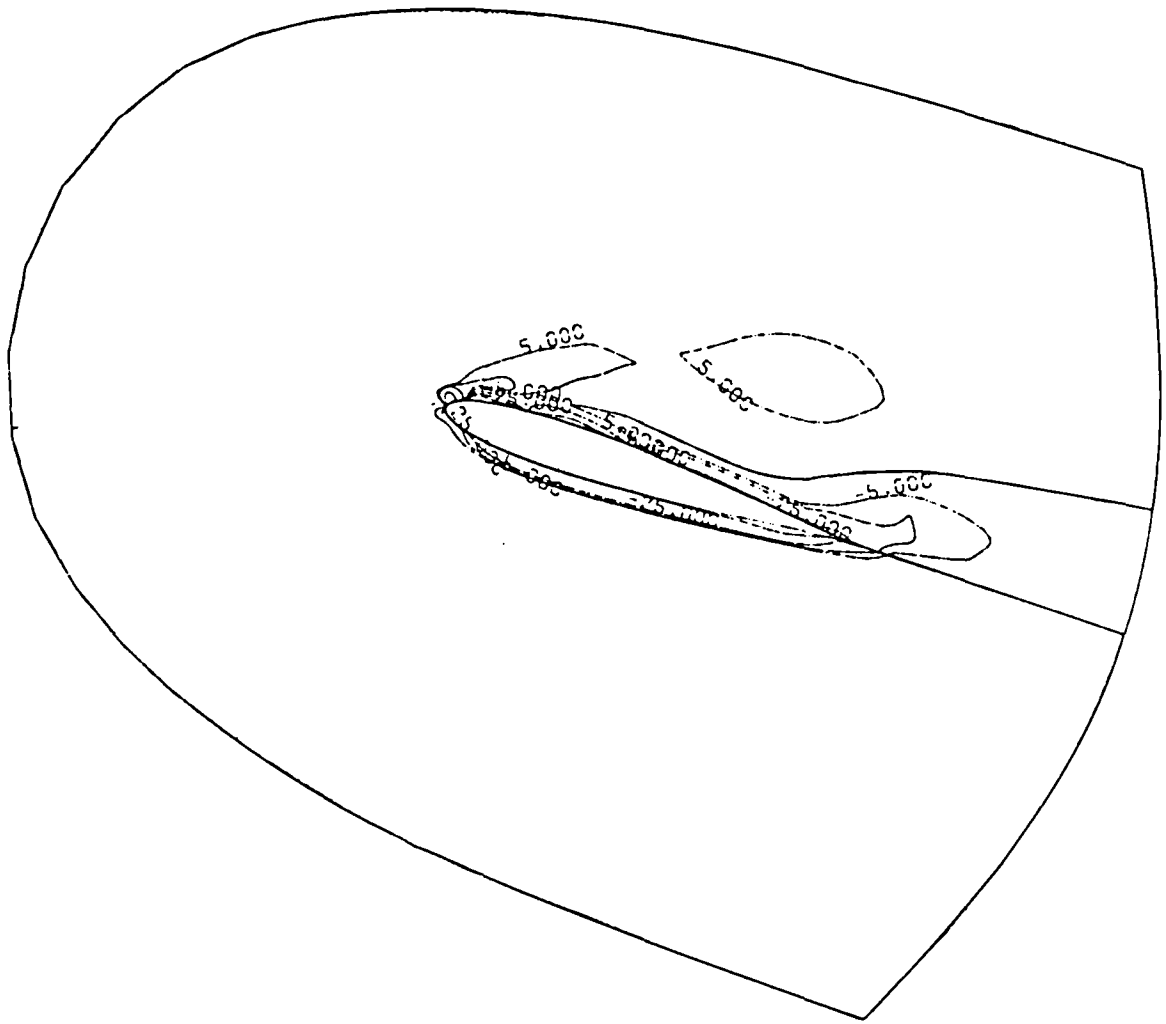

Figure 12 - Vorticity contours, $\alpha = 19°$, $t = t_1 + \Delta t$, $\Delta t = 1.0$.

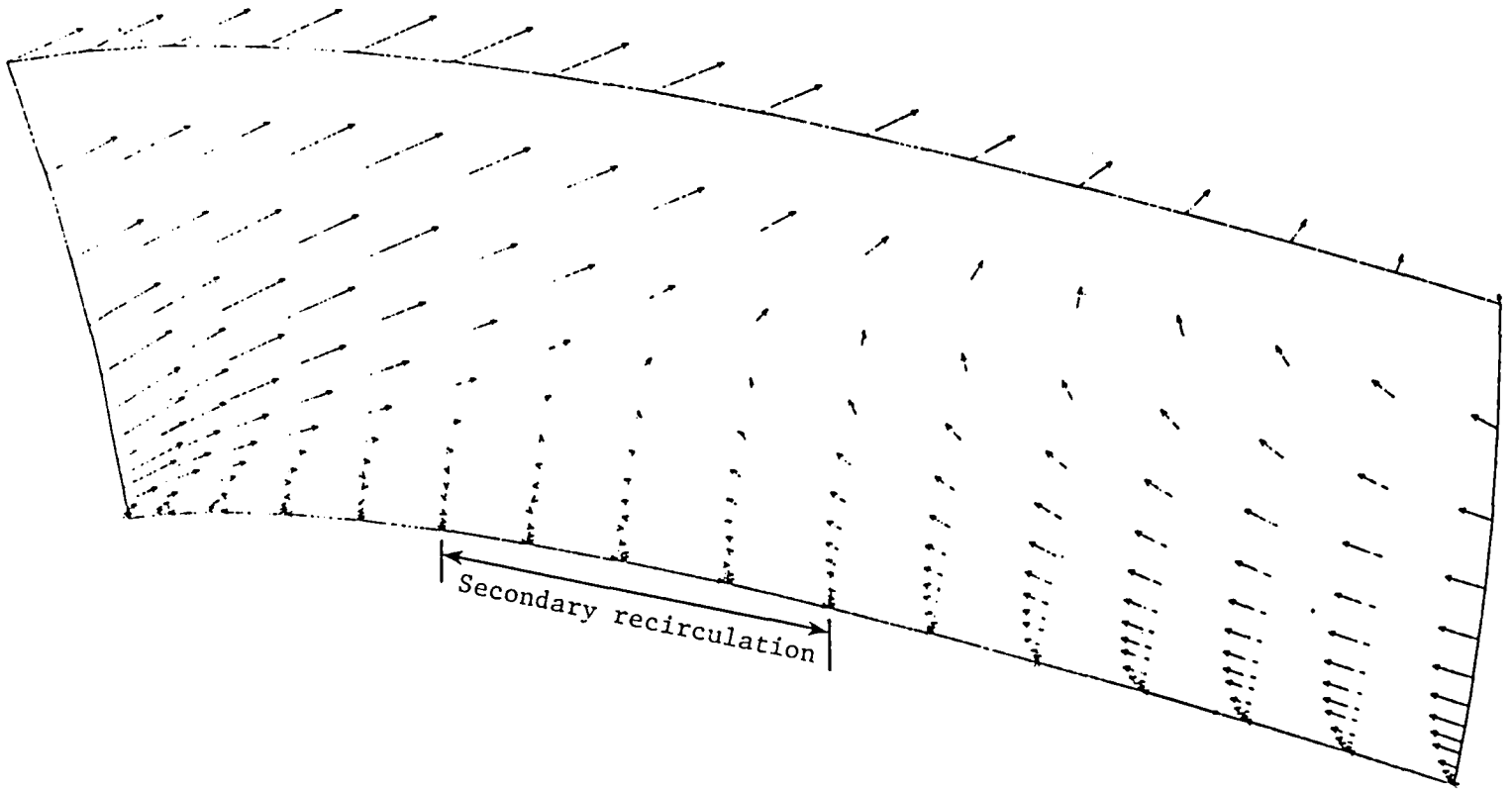

Figure 13 - Velocity vector plot, detail of suction surface, $\alpha = 19°$.

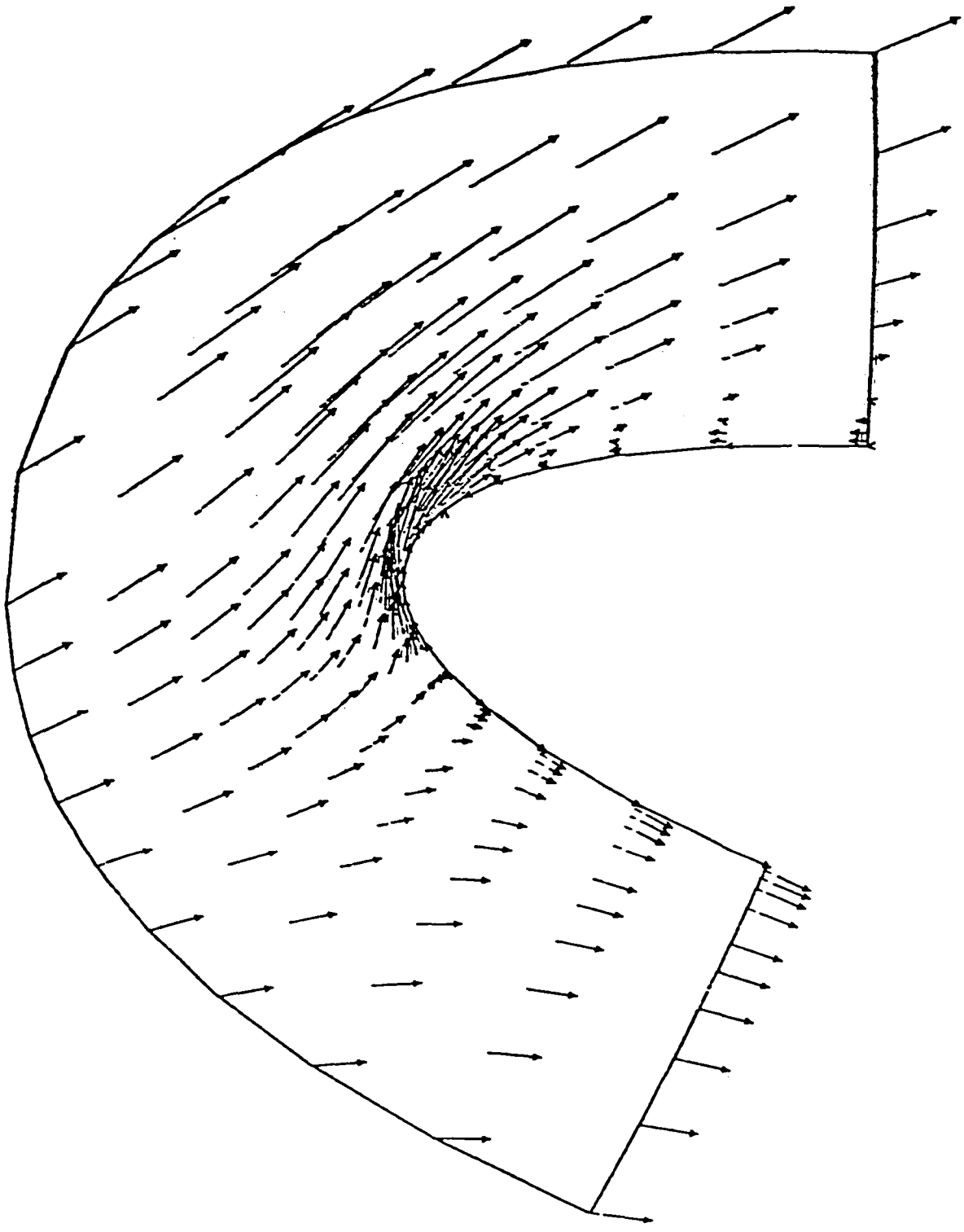

Figure 14 - Velocity vector plot, detail of leading edge region, $\alpha = 19°$

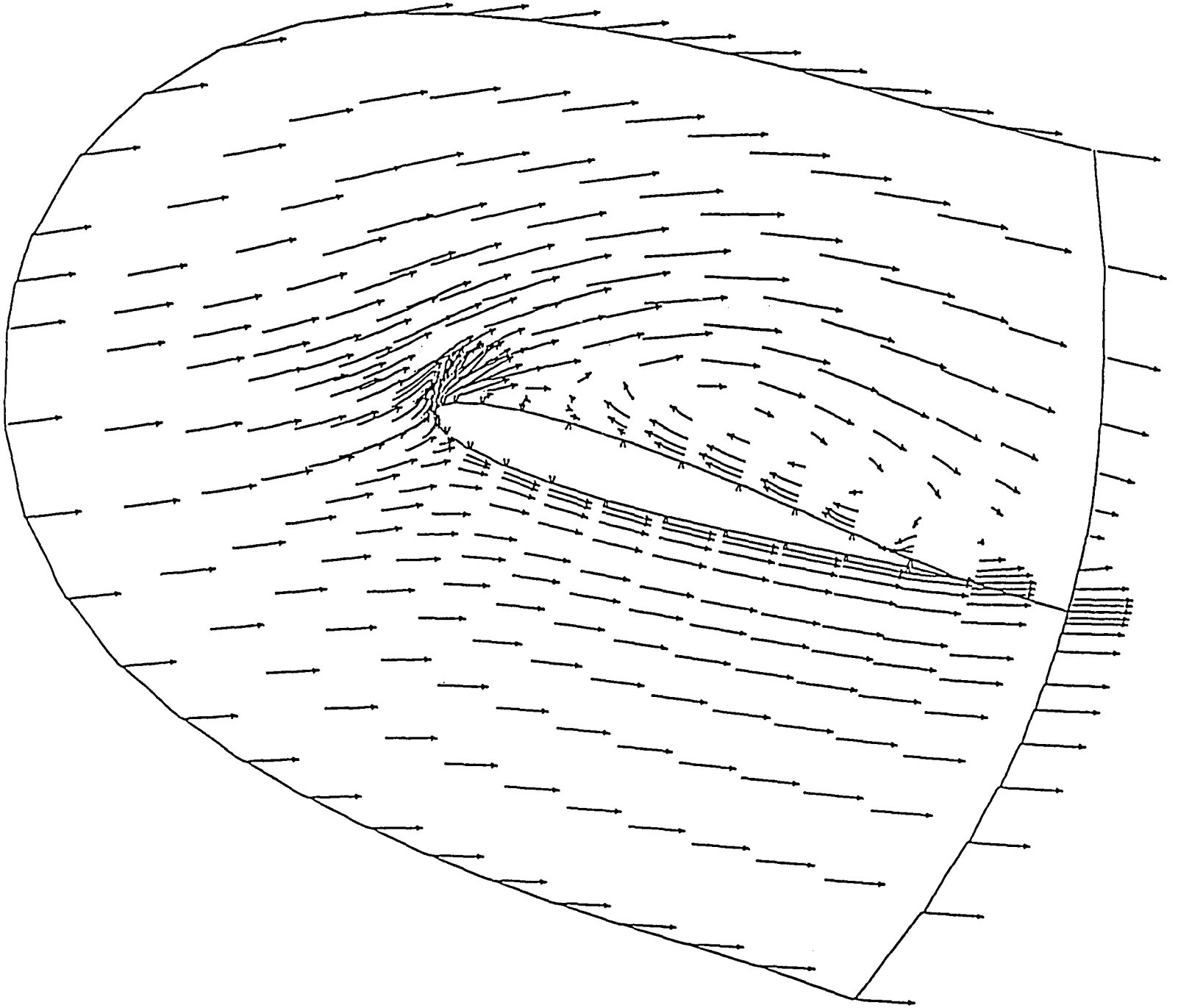

Figure 15 - Computed velocity vector field, $\alpha = 19°$, $M_\infty = .5$.

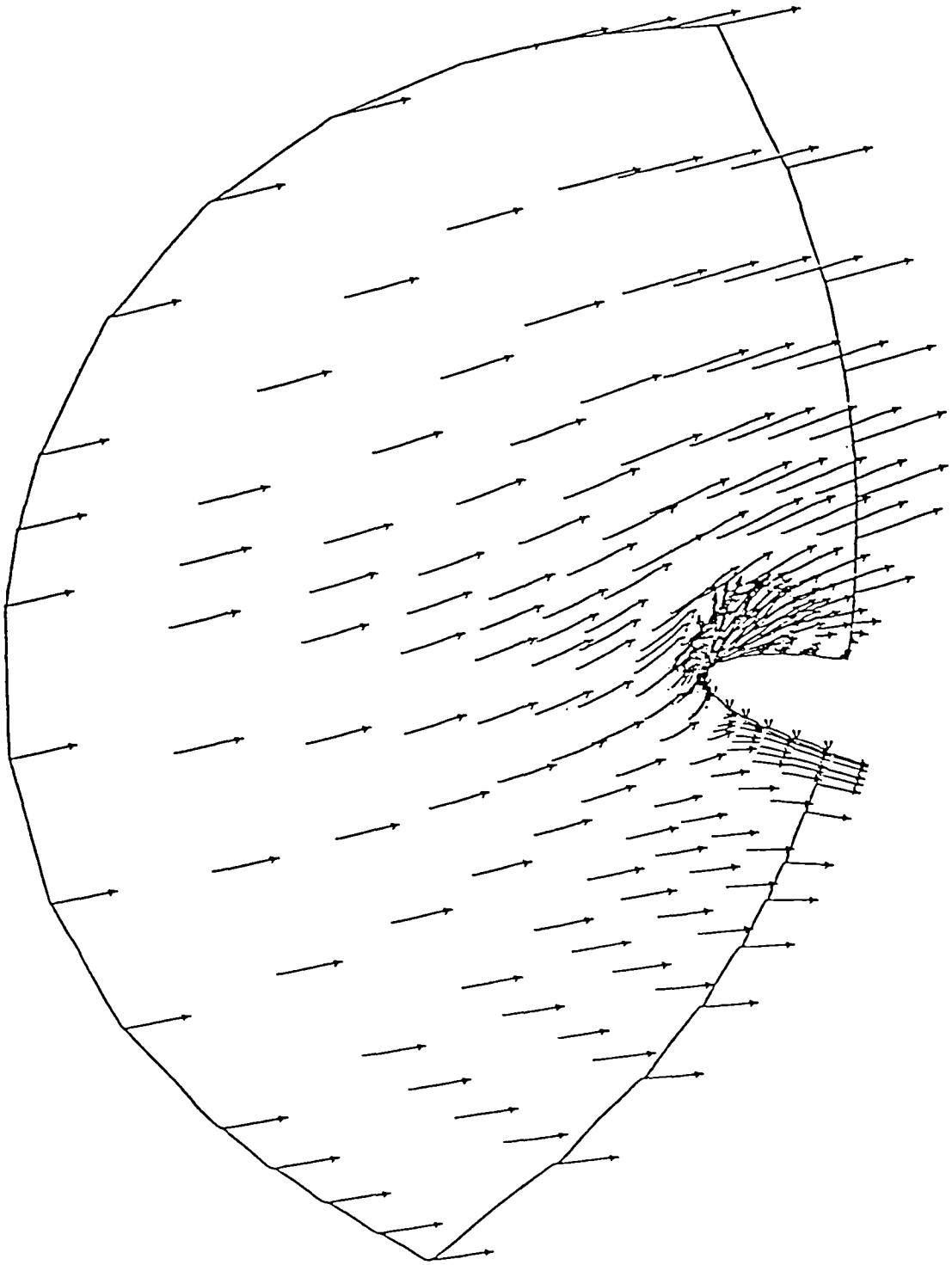

Figure 16 - Computed velocity vector field, $\alpha = 19°$, $M_\infty = .5$.

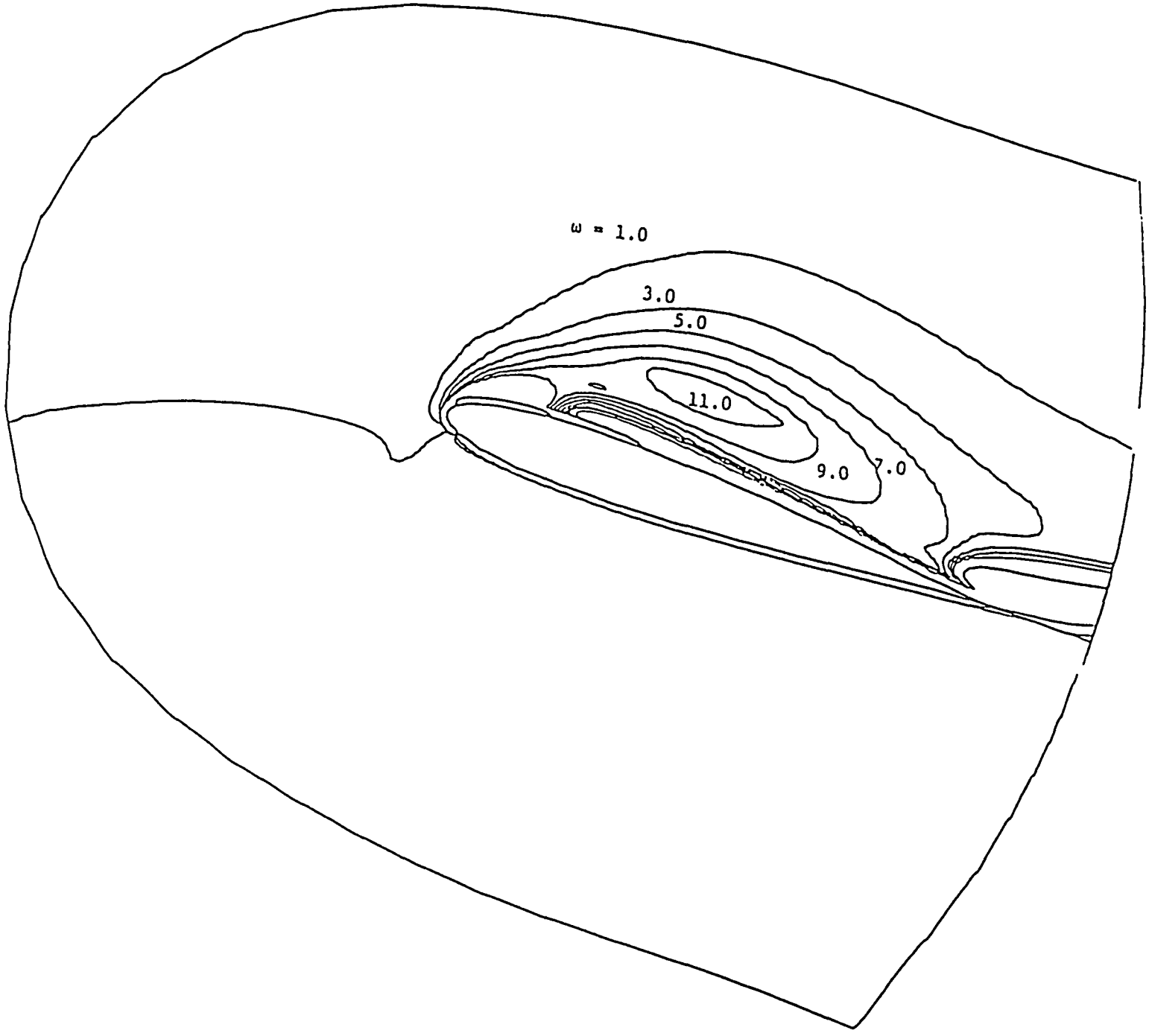

Figure 17 - Vorticity contours, $\alpha = 19°$, $M_\infty = .5$.

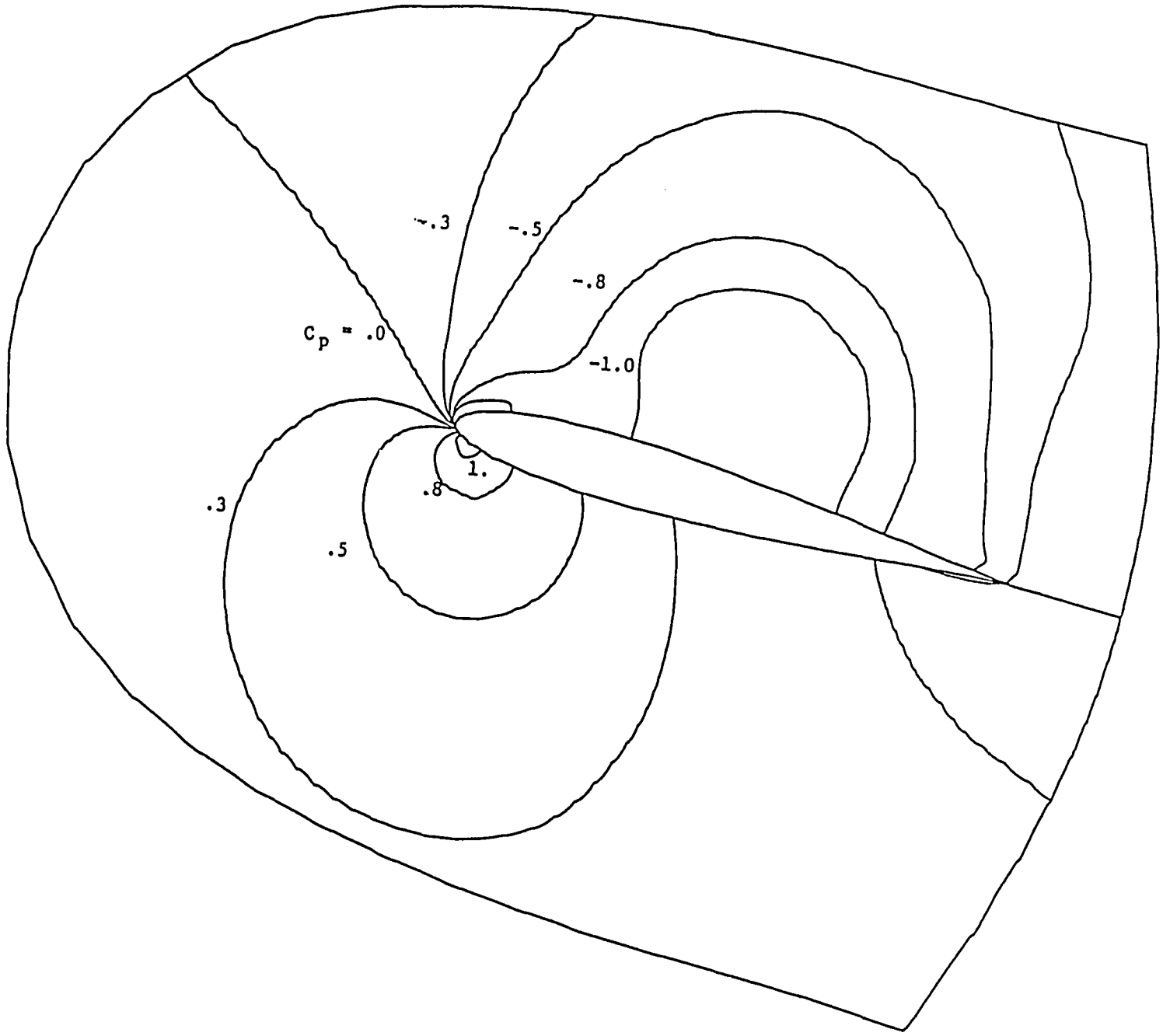

Figure 18 - Static pressure coefficient contours, $\alpha = 19°$, $M_\infty = .5$.

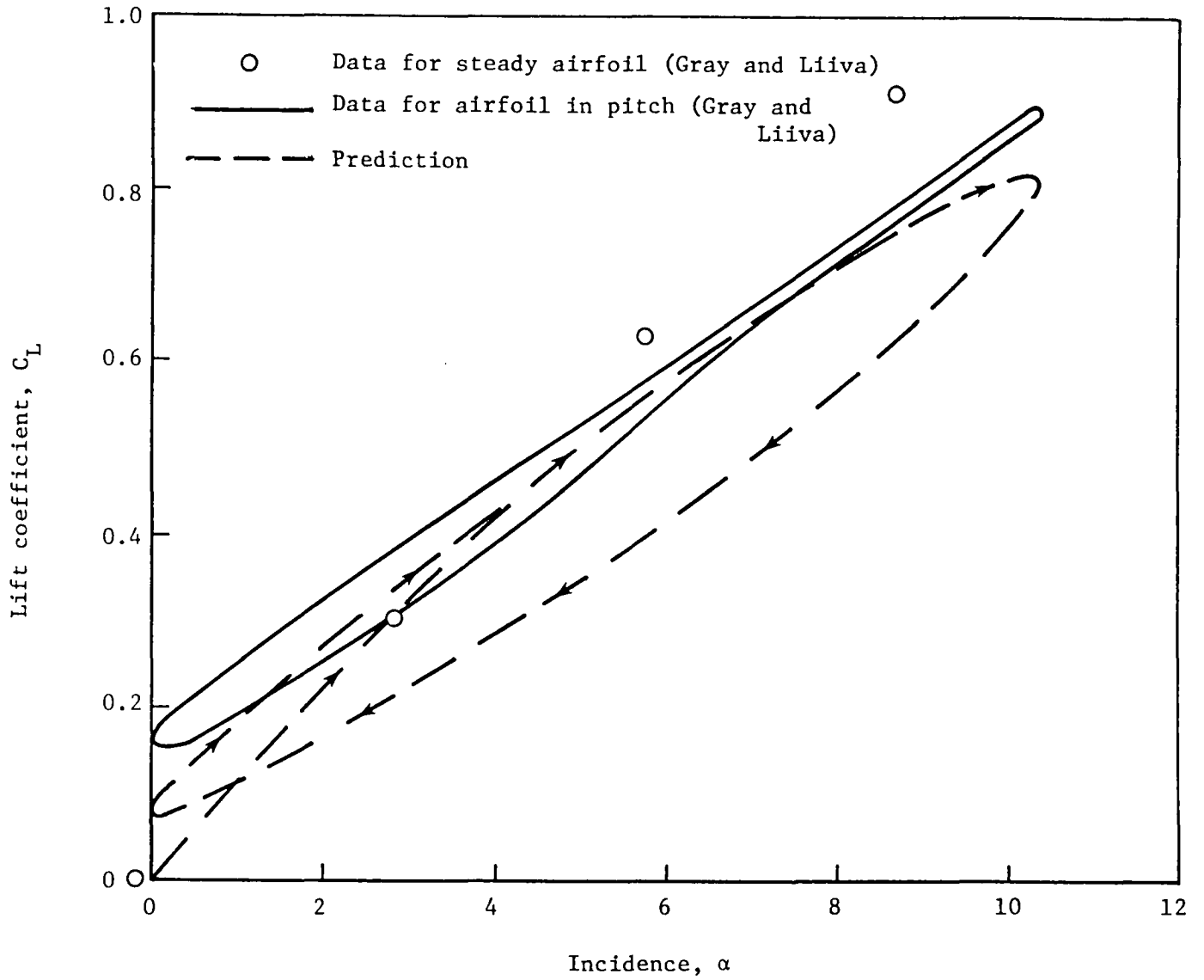

Figure 19 - Lift vs. incidence curve for NACA 0012 airfoil in pitch, k = 0.25.

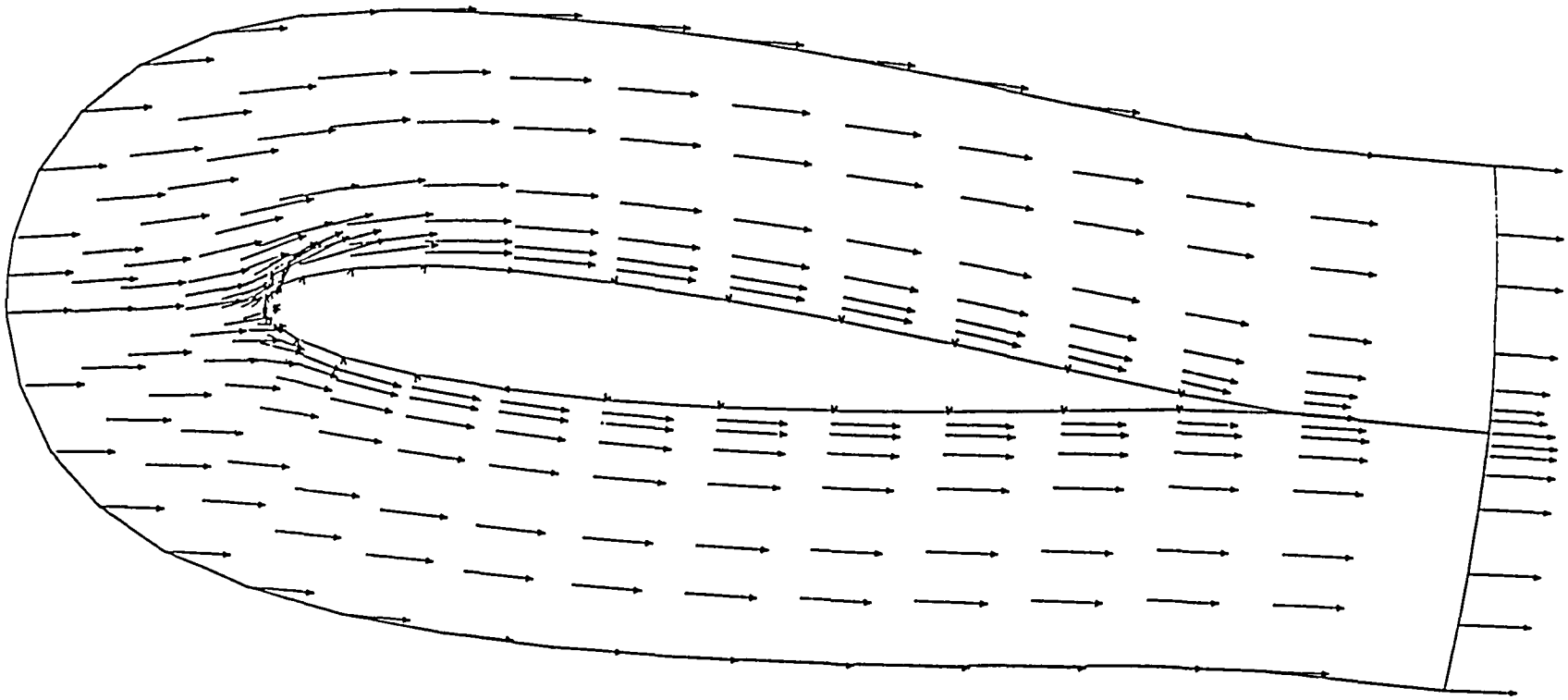

Figure 20 - Velocity field, $\alpha = 5°$, $\dot{\alpha} > 0$.

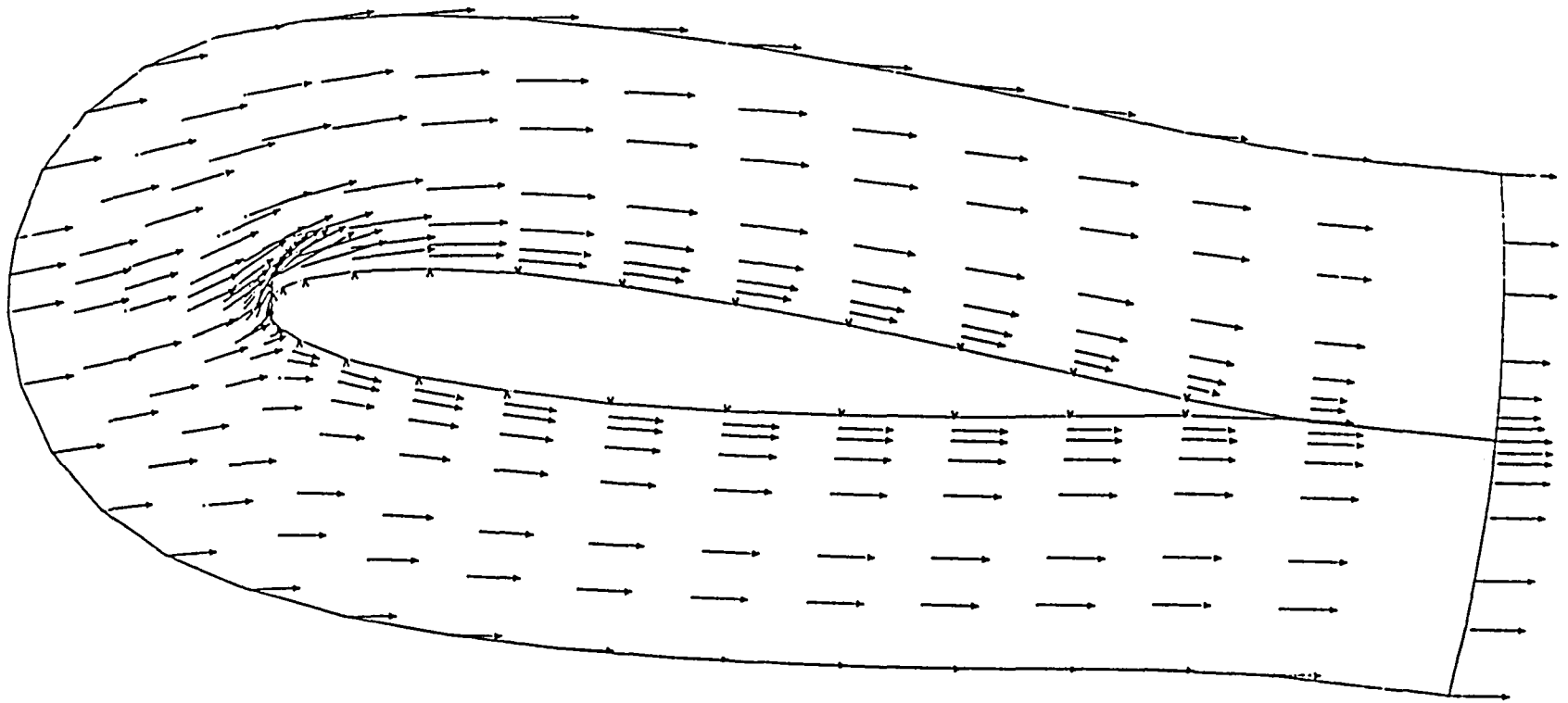

Figure 21 - Velocity field, $\alpha = 10°$, $\dot{\alpha} > 0$.

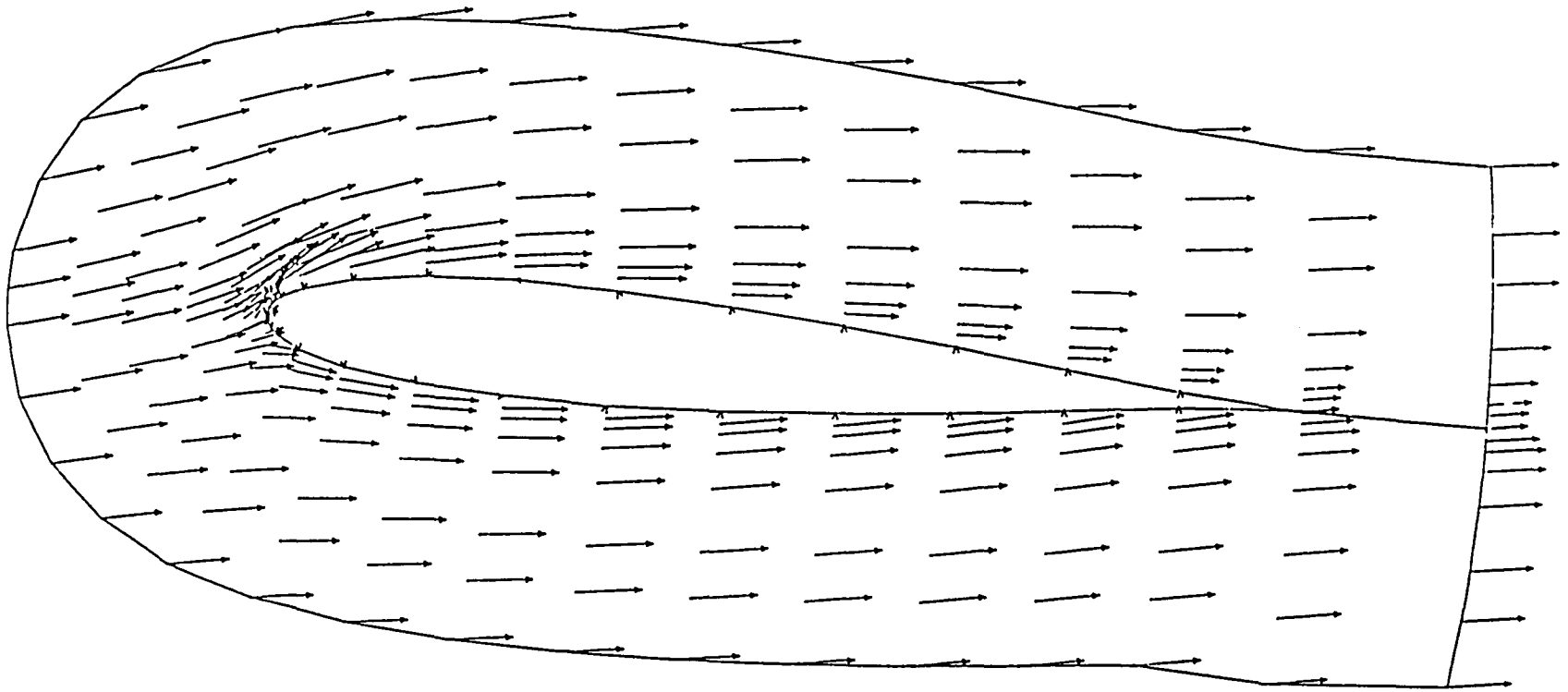

Figure 22 - Velocity field, $\alpha = 5°$, $\dot{\alpha} < 0$.

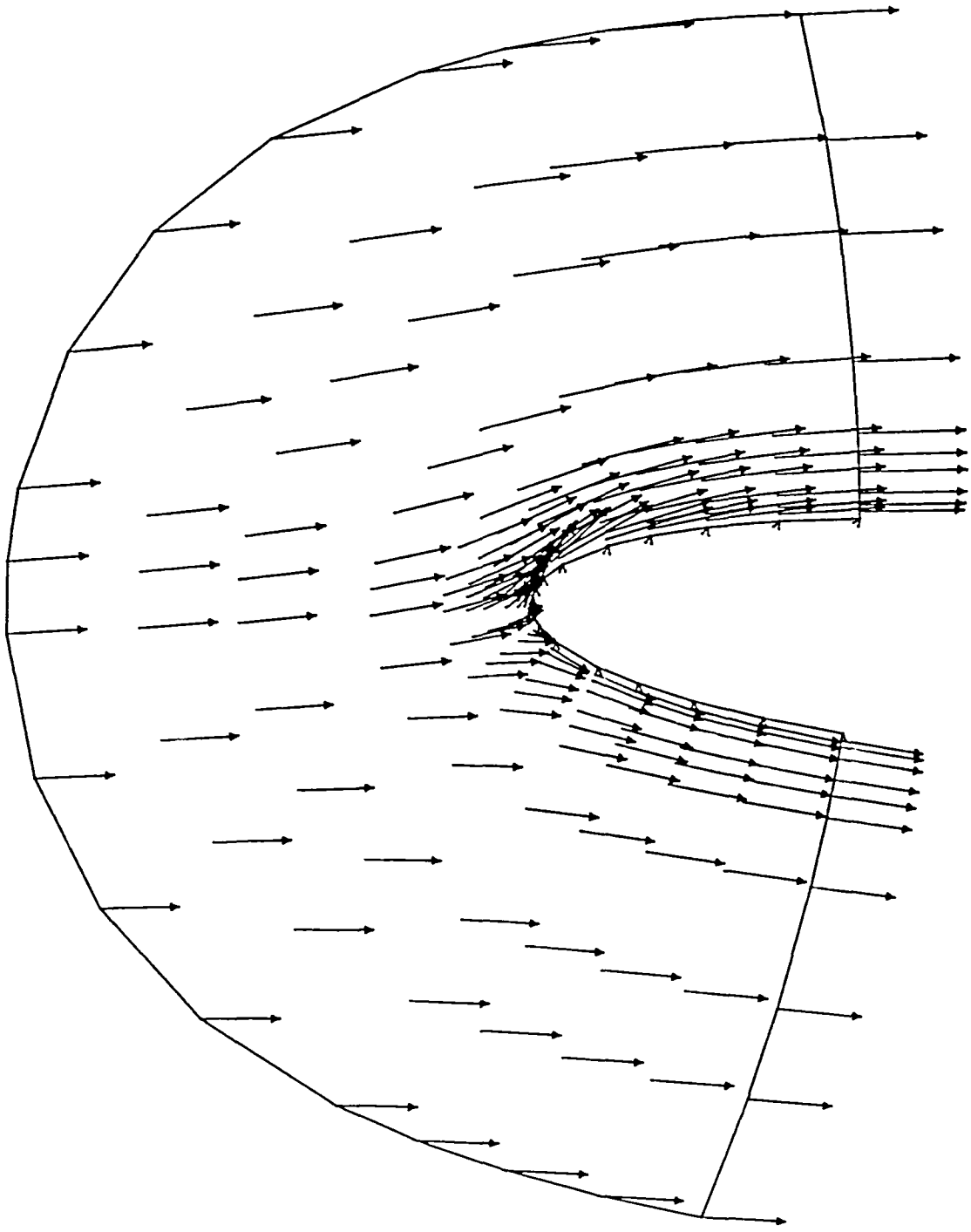

Figure 23 - Velocity field, $\alpha = 5°$, $\dot{\alpha} > 0$.

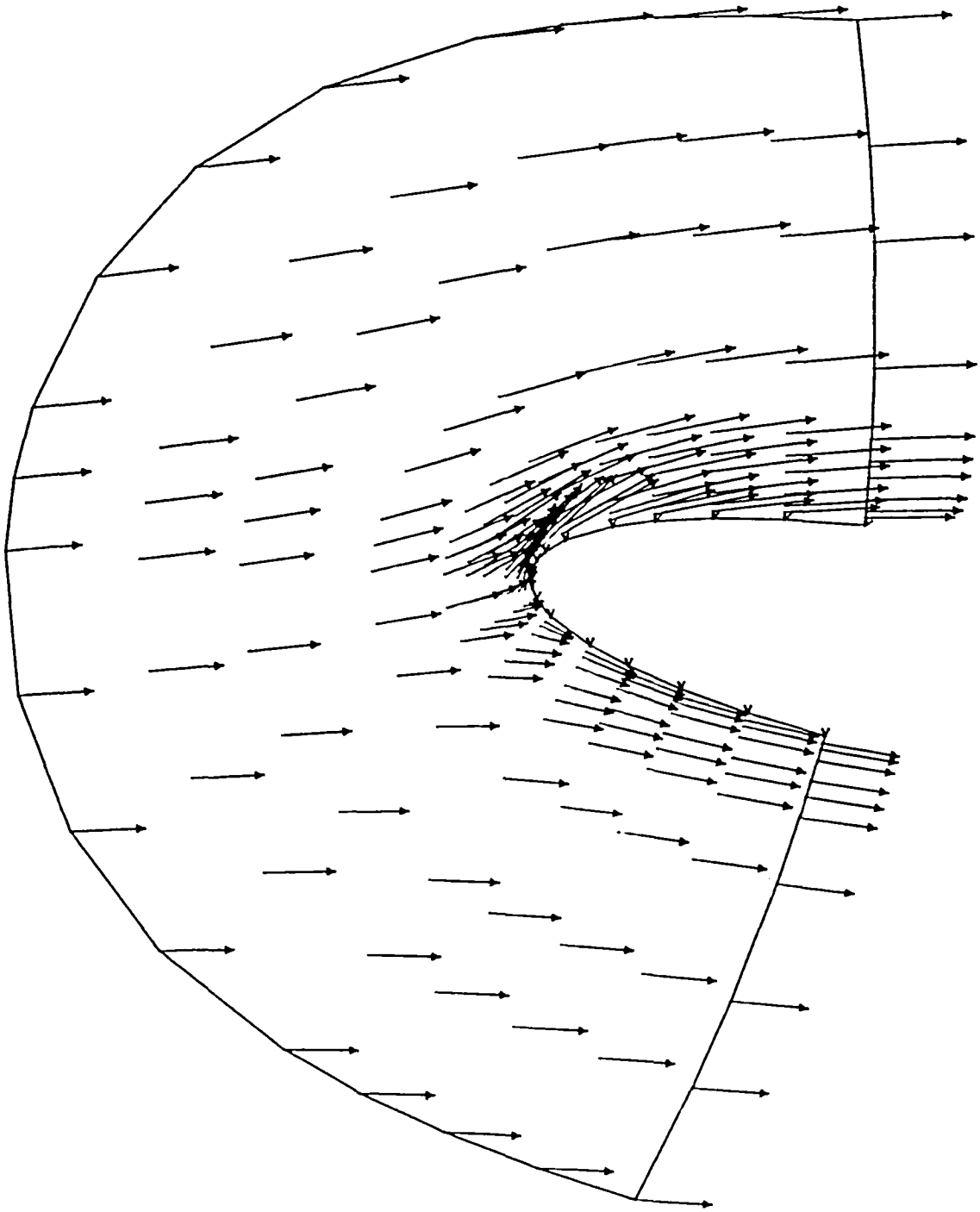

Figure 24 - Velocity field, $\alpha = 10°$, $\dot{\alpha} > 0$.

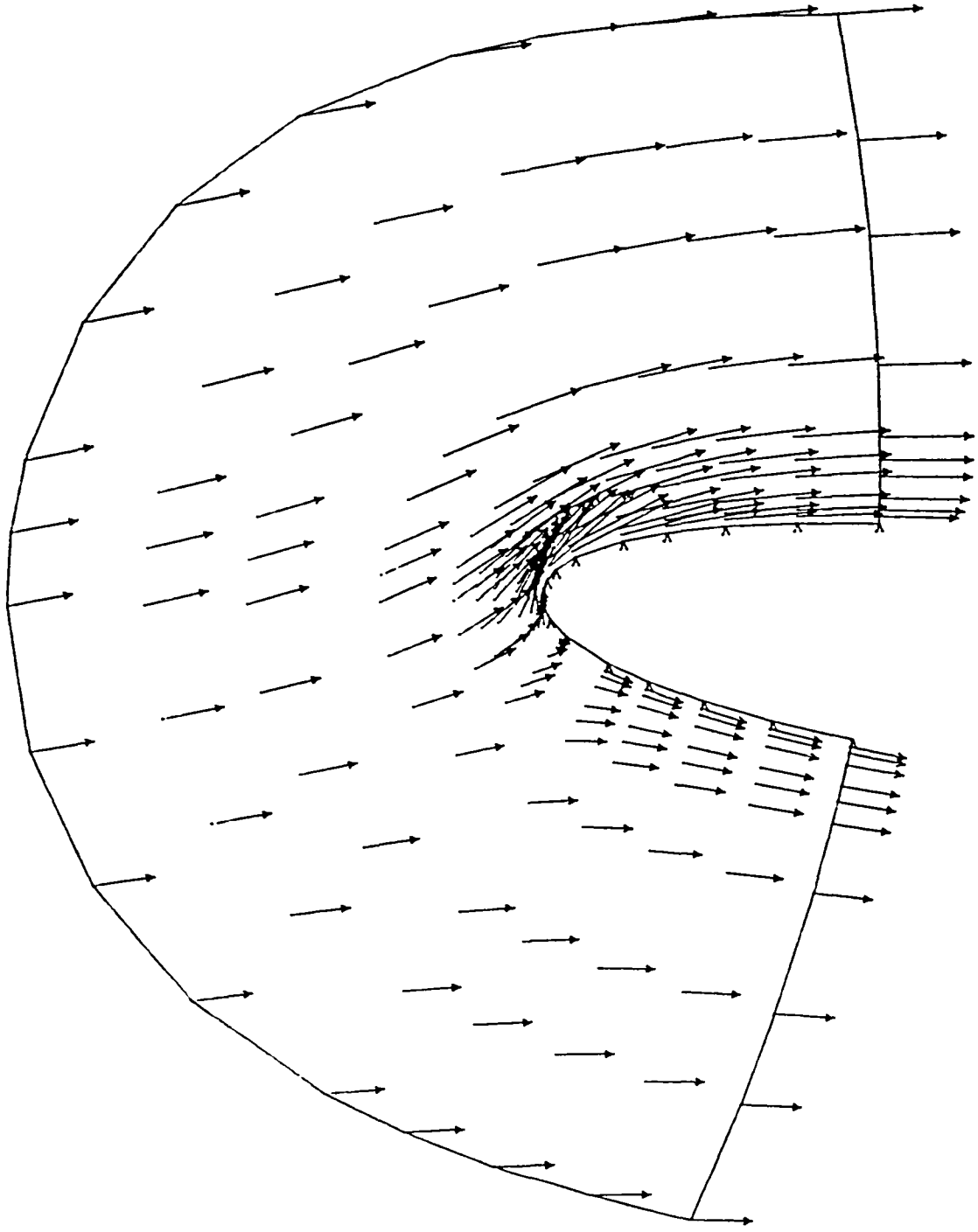

Figure 25 - Velocity field, $\alpha = 5°$, $\dot{\alpha} < 0$.

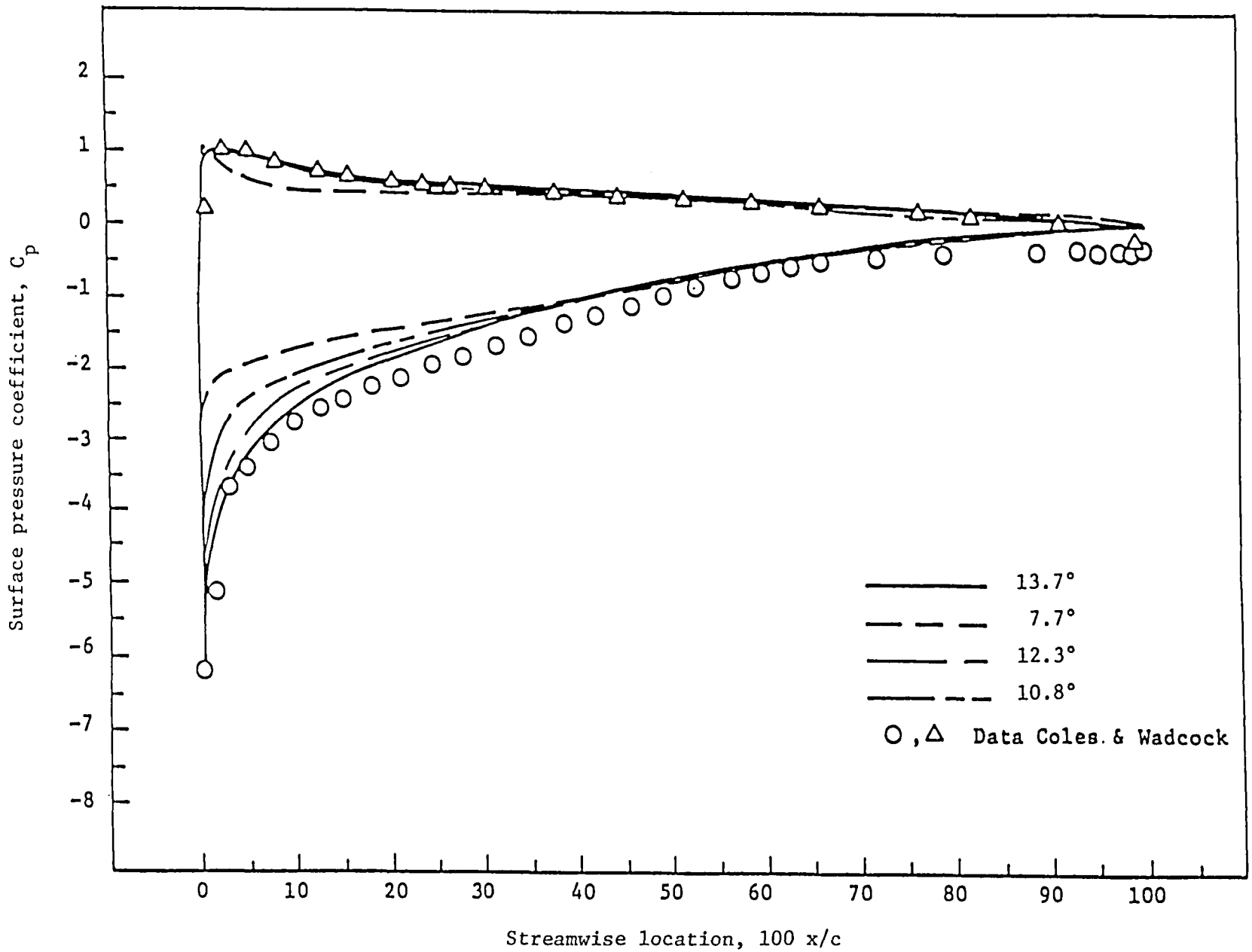

Figure 26 - Prediction of surface pressure distribution for NACA 4412 airfoil at incidence.

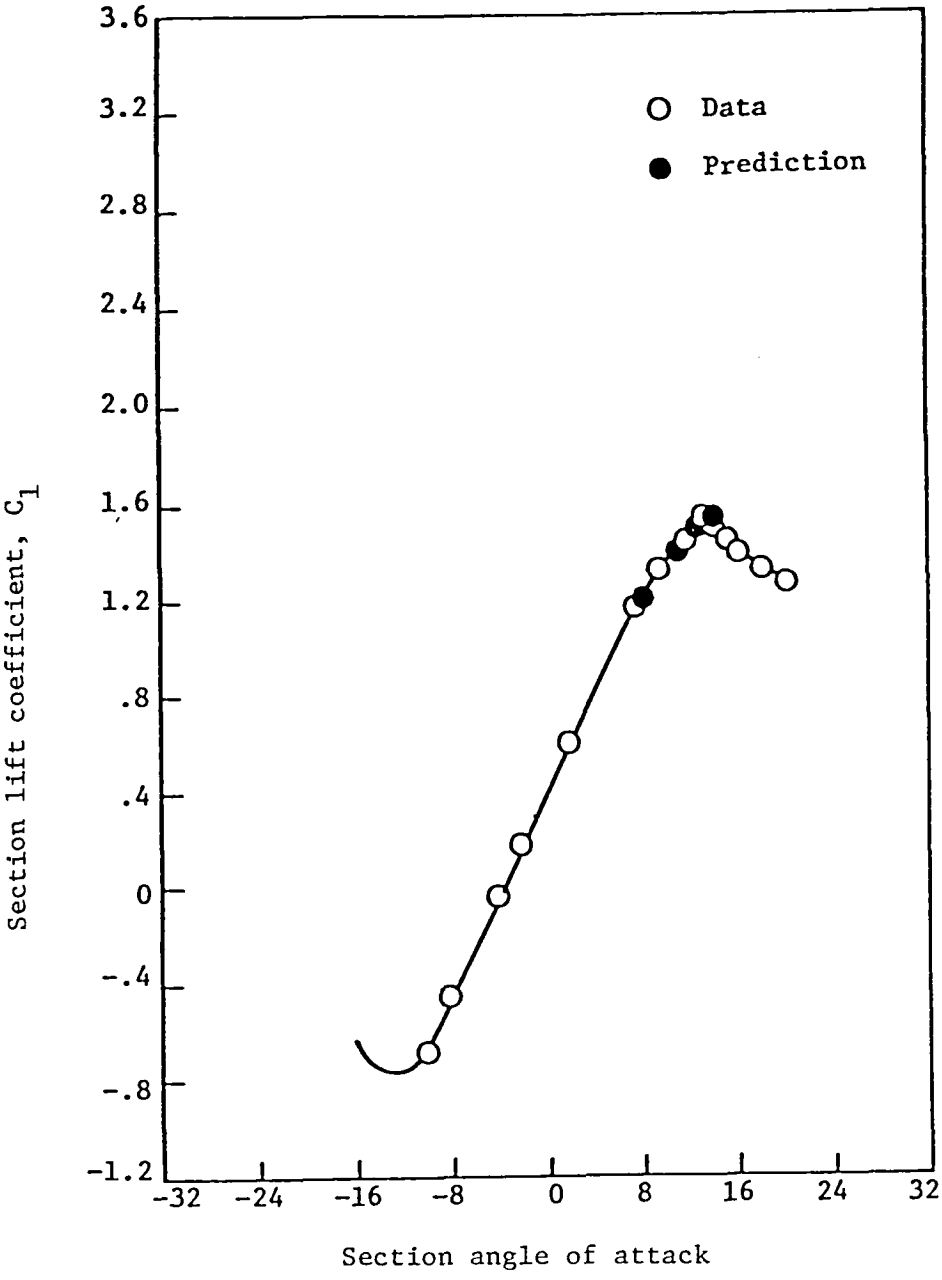

Figure 27 - Comparison of predicted and measured lift coefficient for NACA 4412 airfoil.

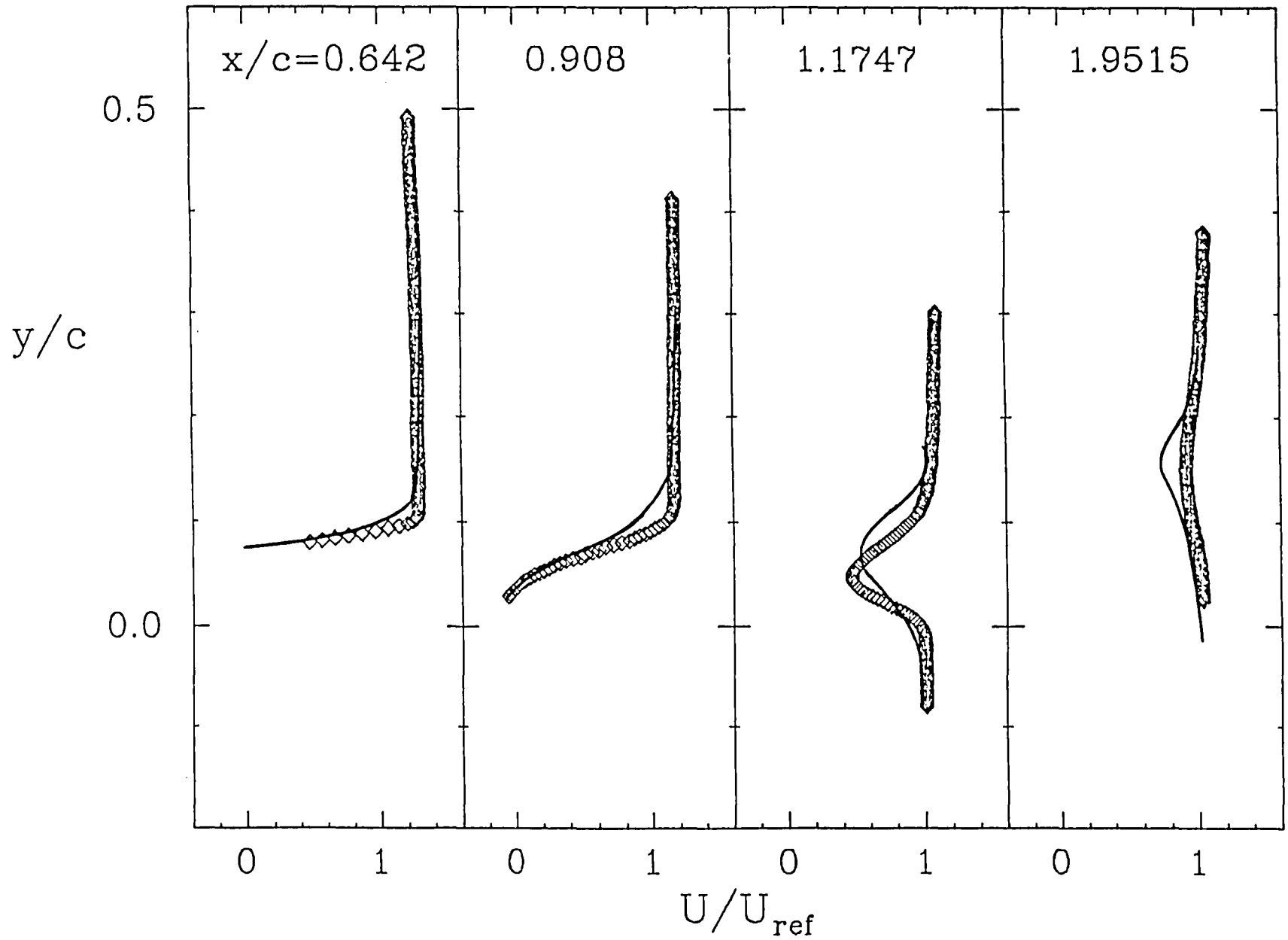

Figure 28 - Boundary layer and wake streamwise velocity profiles for NACA 4412 airfoil.

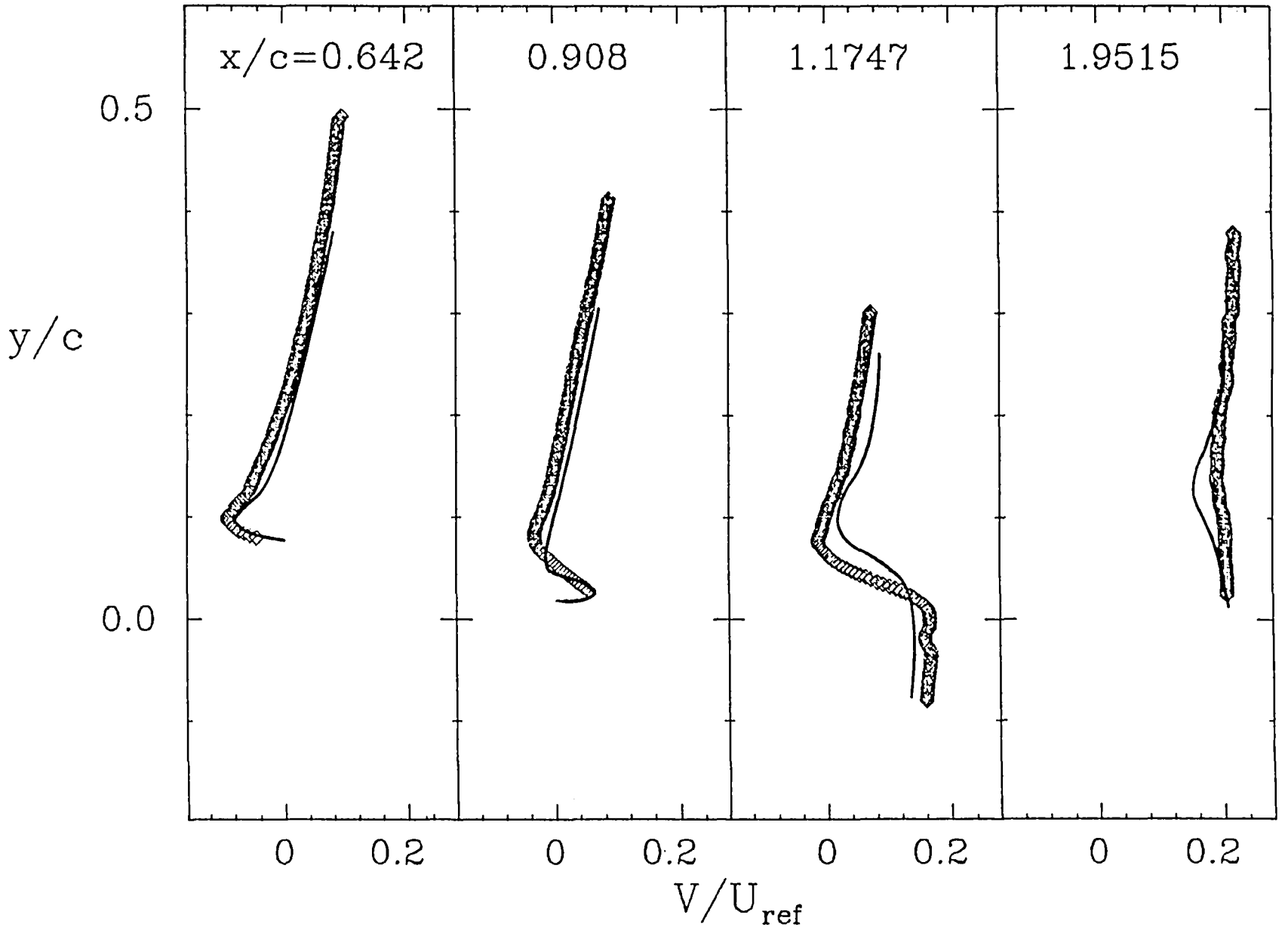

Figure 29 - Boundary layer and wake transverse velocity profiles for NACA 4412 airfoil.

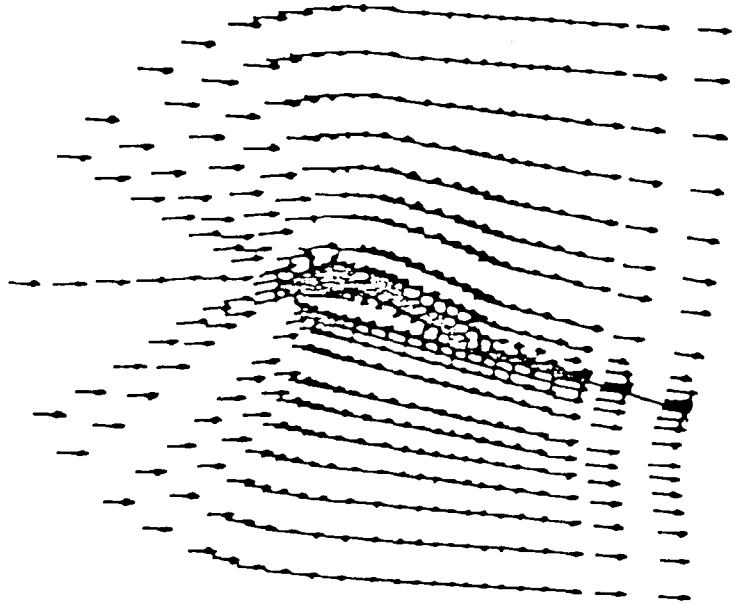

Figure 30 - Vector plot NACA 4412 airfoil, $\alpha = 13.7°$.

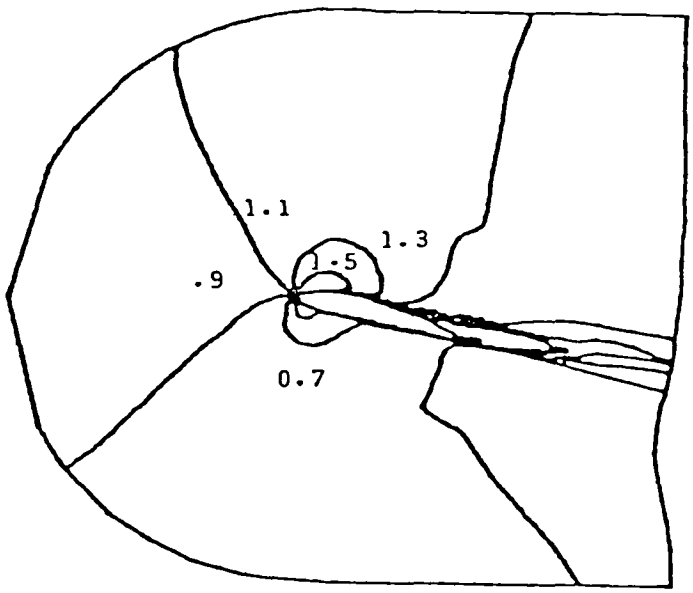

Figure 31 - U-Velocity coefficient, NACA 4412 airfoil, $\alpha = 13.7°$.

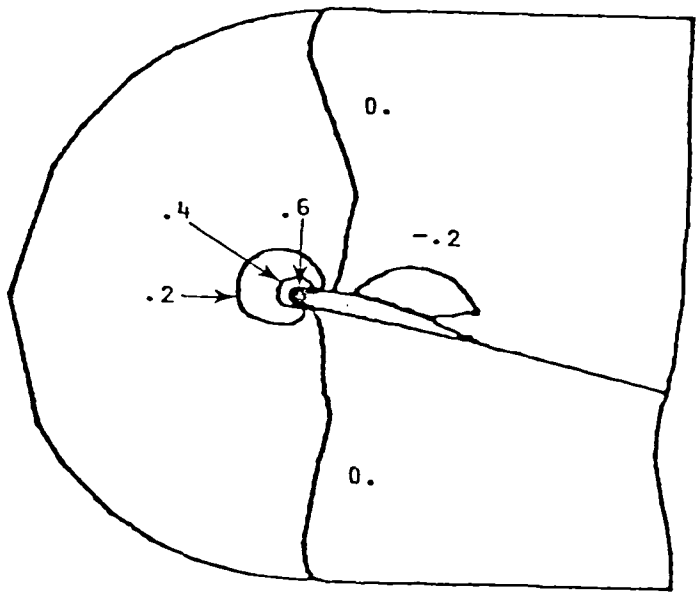

Figure 32 - W-Velocity profile, NACA 4412 airfoil, $\alpha = 13.7°$.

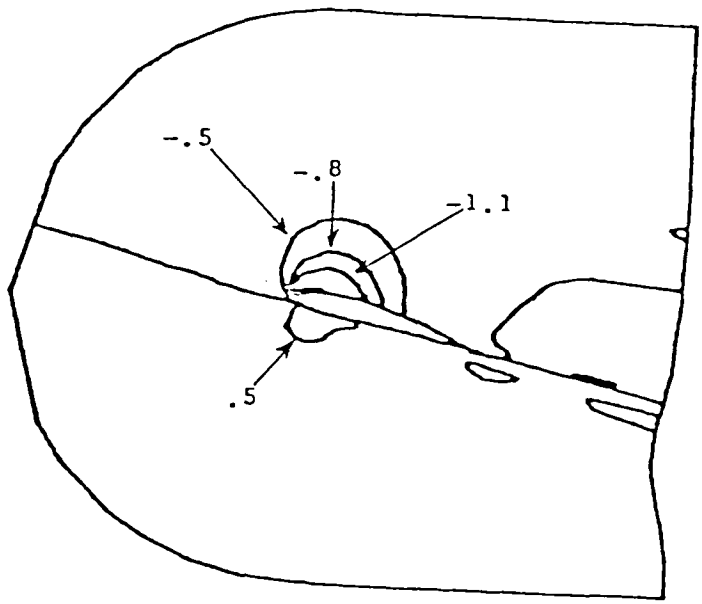

Figure 33 - Pressure coefficient, NACA 4412 airfoil, $\alpha = 13.7°$.

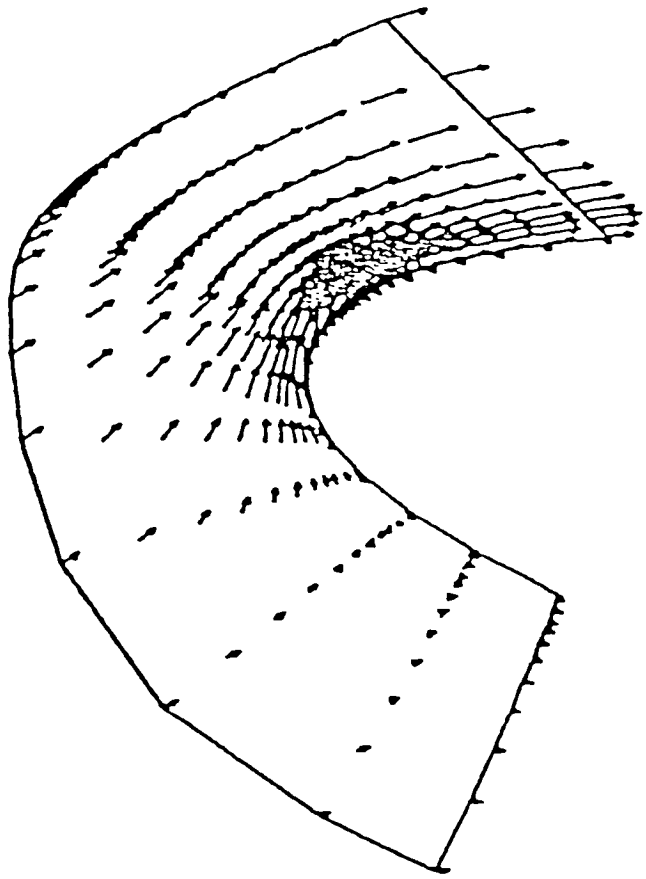

Figure 34 - Vector plot, NACA 4412 airfoil, $\alpha = 13.7°$.

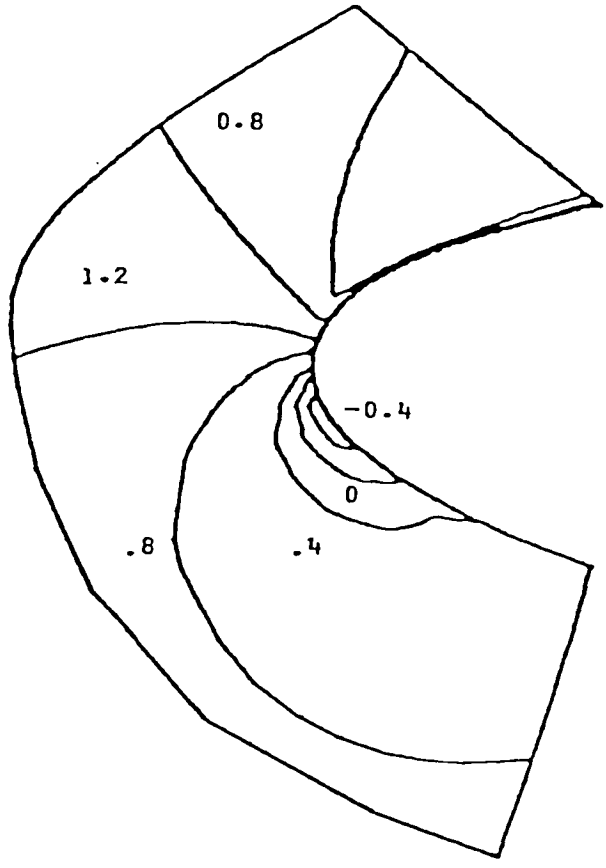

Figure 35 - U-Velocity, NACA 4412 airfoil, α = 13.7°.

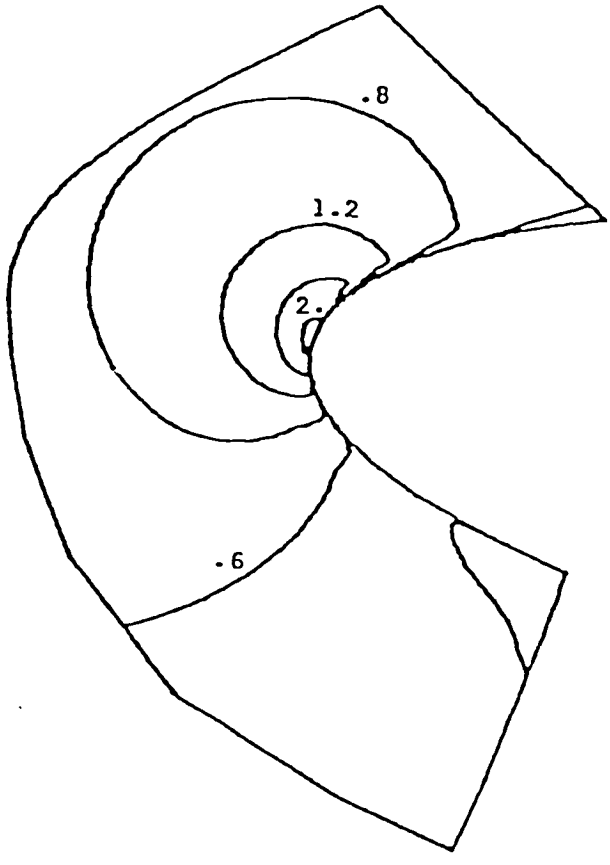

Figure 36 - W-Velocity contours, NACA 4412 airfoil, α = 13.7°.

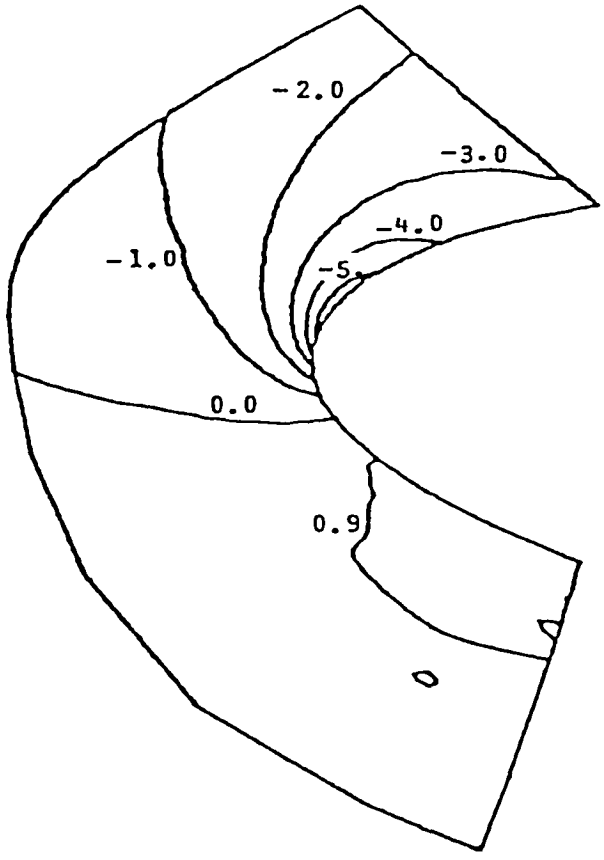

Figure 37 – Pressure coefficient, NACA 4412 airfoil, $\alpha = 13.7°$.

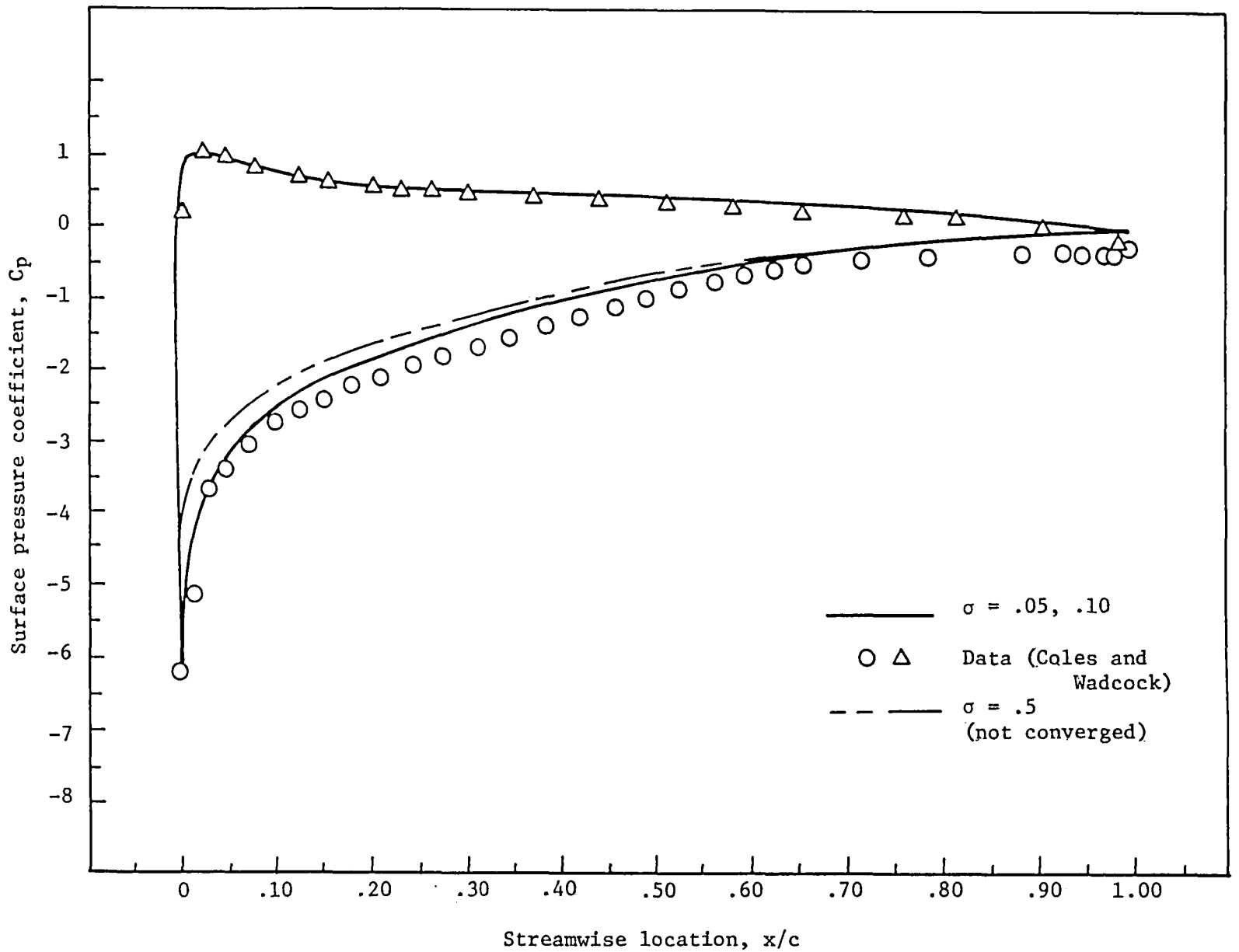

Figure 38 - Effect of dissipation parameter on surface pressure coefficient for NACA 4412 airfoil.

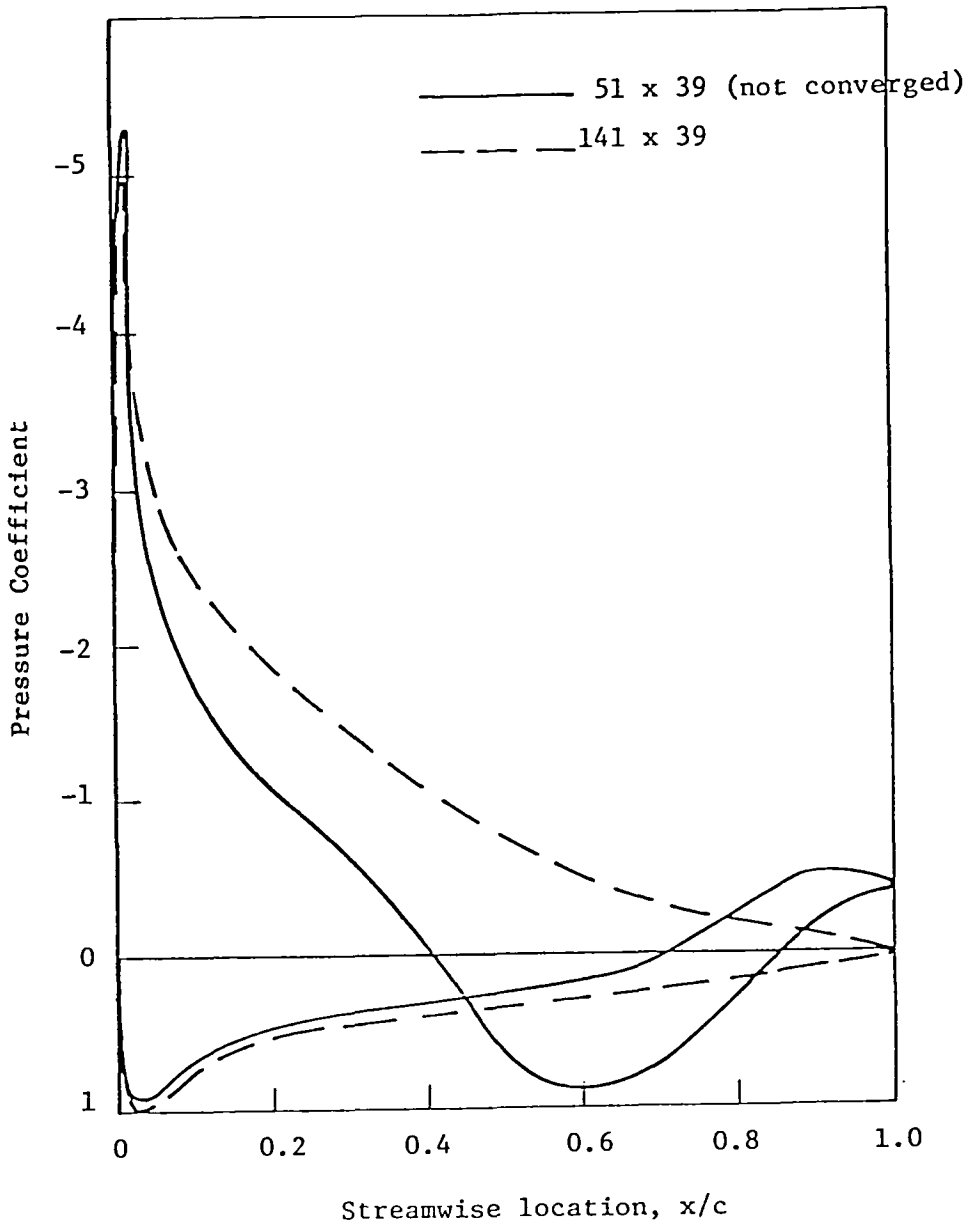

Figure 39 - Grid resolution study. NACA 4412 airfoil at 12.3 degrees incidence.

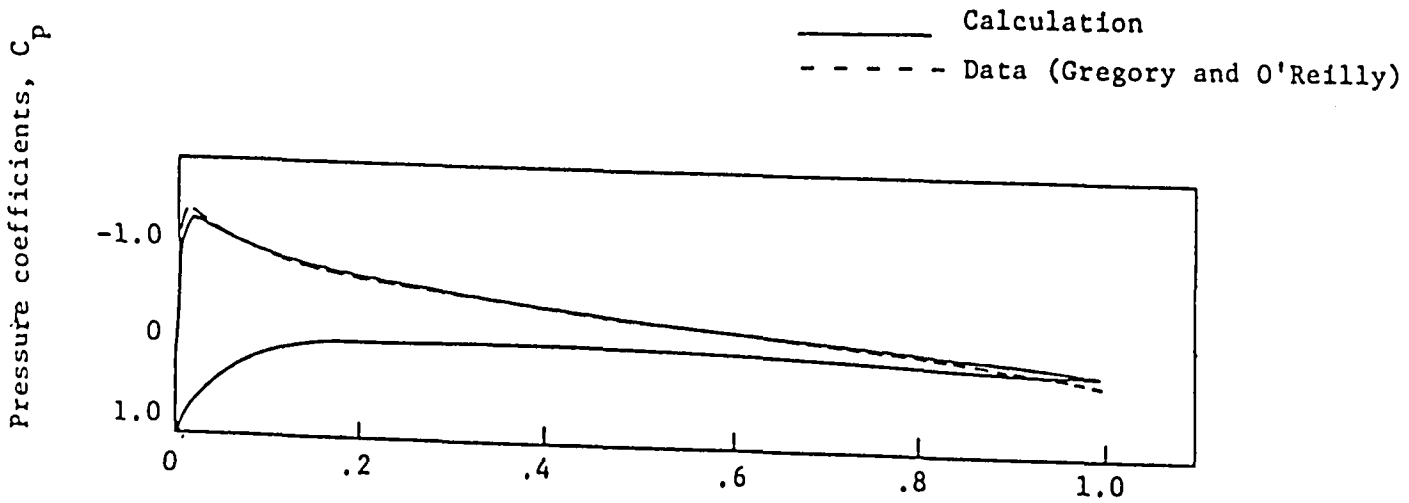

Figure 40 - Comparison of calculated and measured pressure distribution, NACA 0012, $\alpha = 4°$.

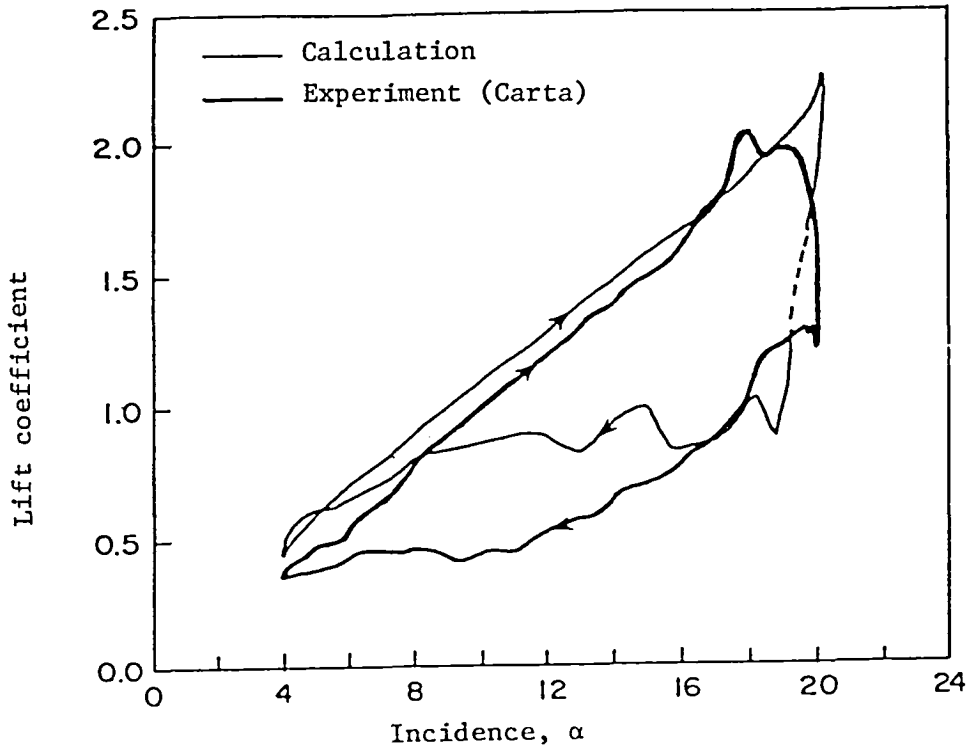

Figure 41 - Lift coefficient - NACA 0012 airfoil.

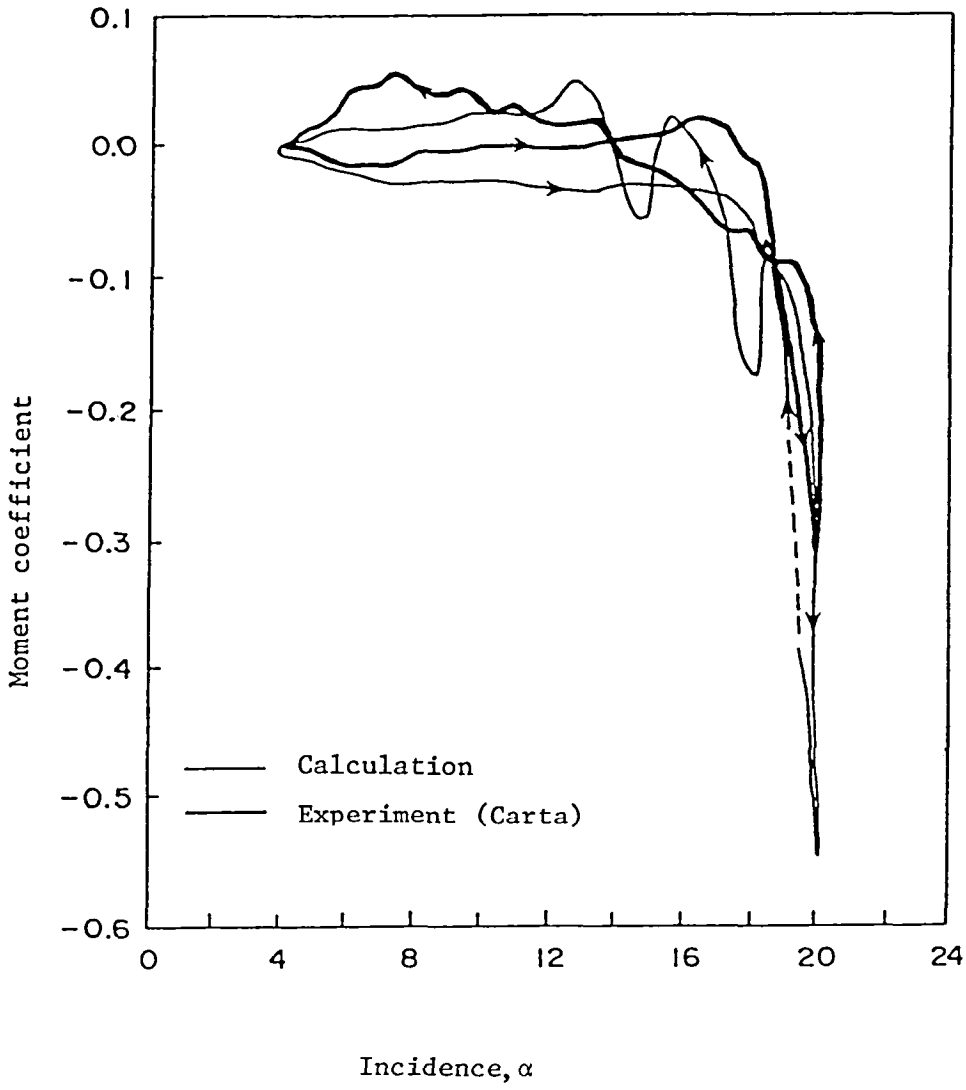

Figure 42 - Moment coefficient - NACA 0012 airfoil.

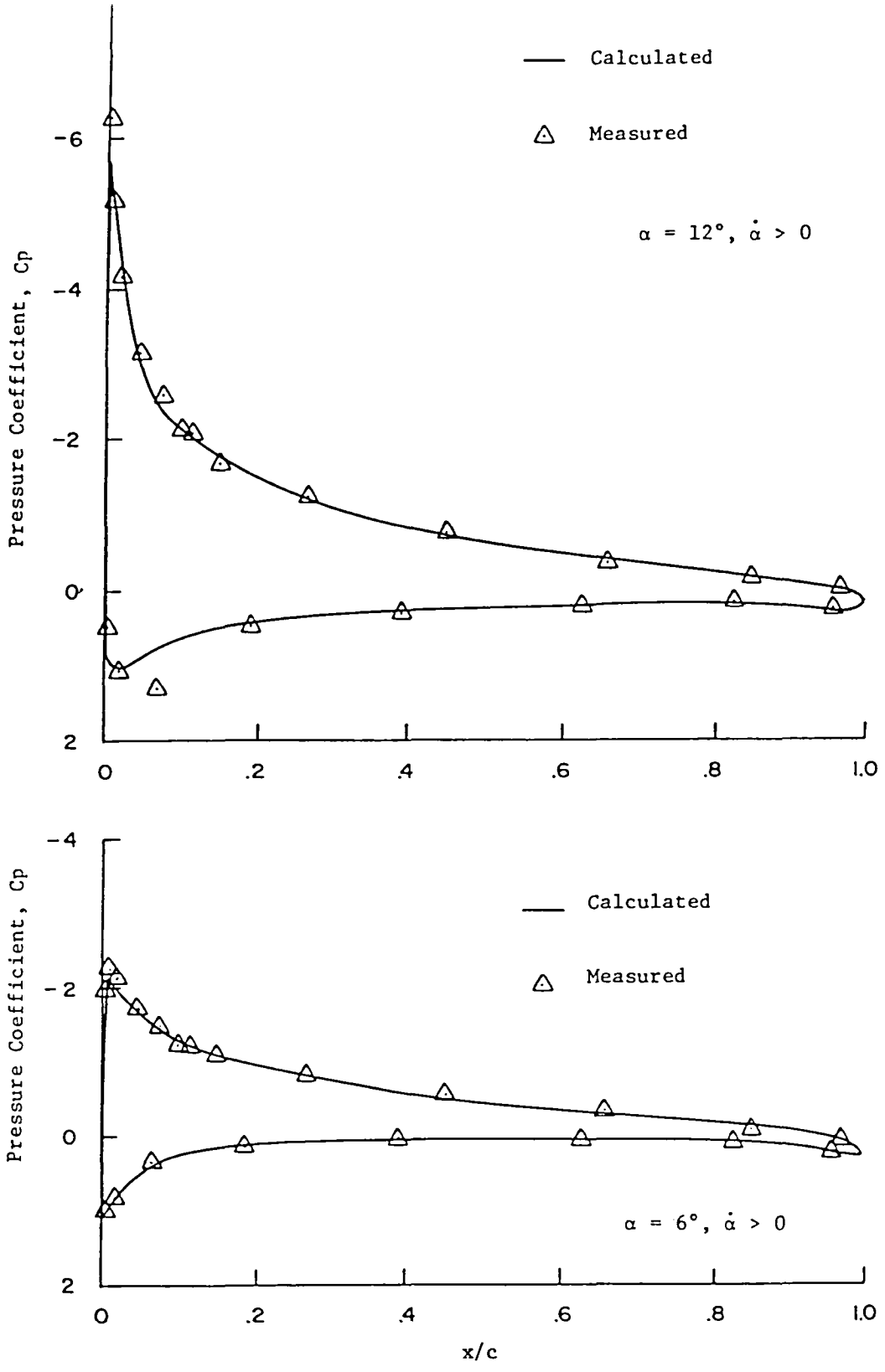

Figure 43 - Pressure coefficient comparison - NACA 0012 airfoil. $\alpha = 6°, 12°, \dot{\alpha} > 0$

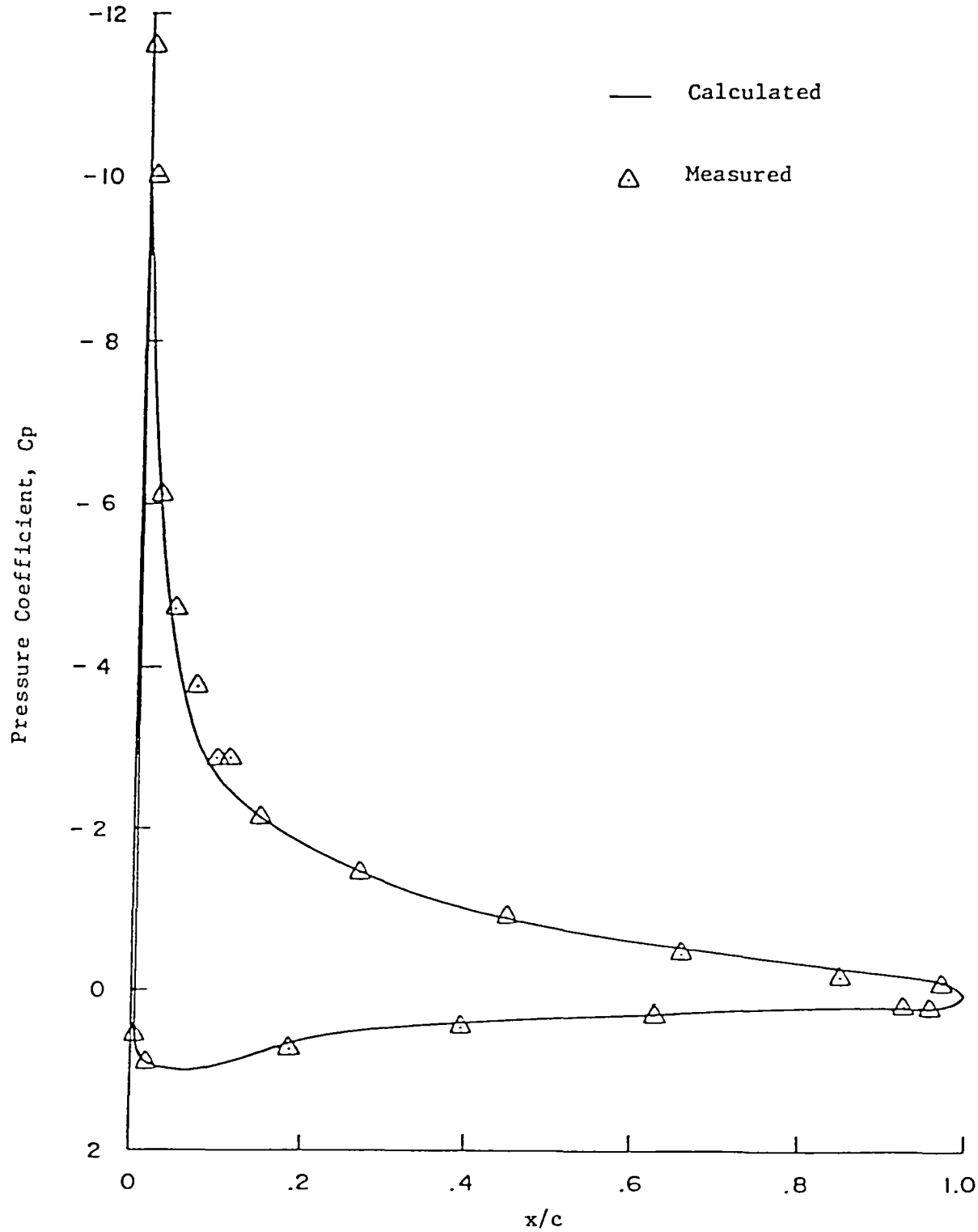

Figure 44 - Pressure coefficient comparison - NACA 0012 airfoil. $\alpha = 15.9°$, $\dot{\alpha} > 0$

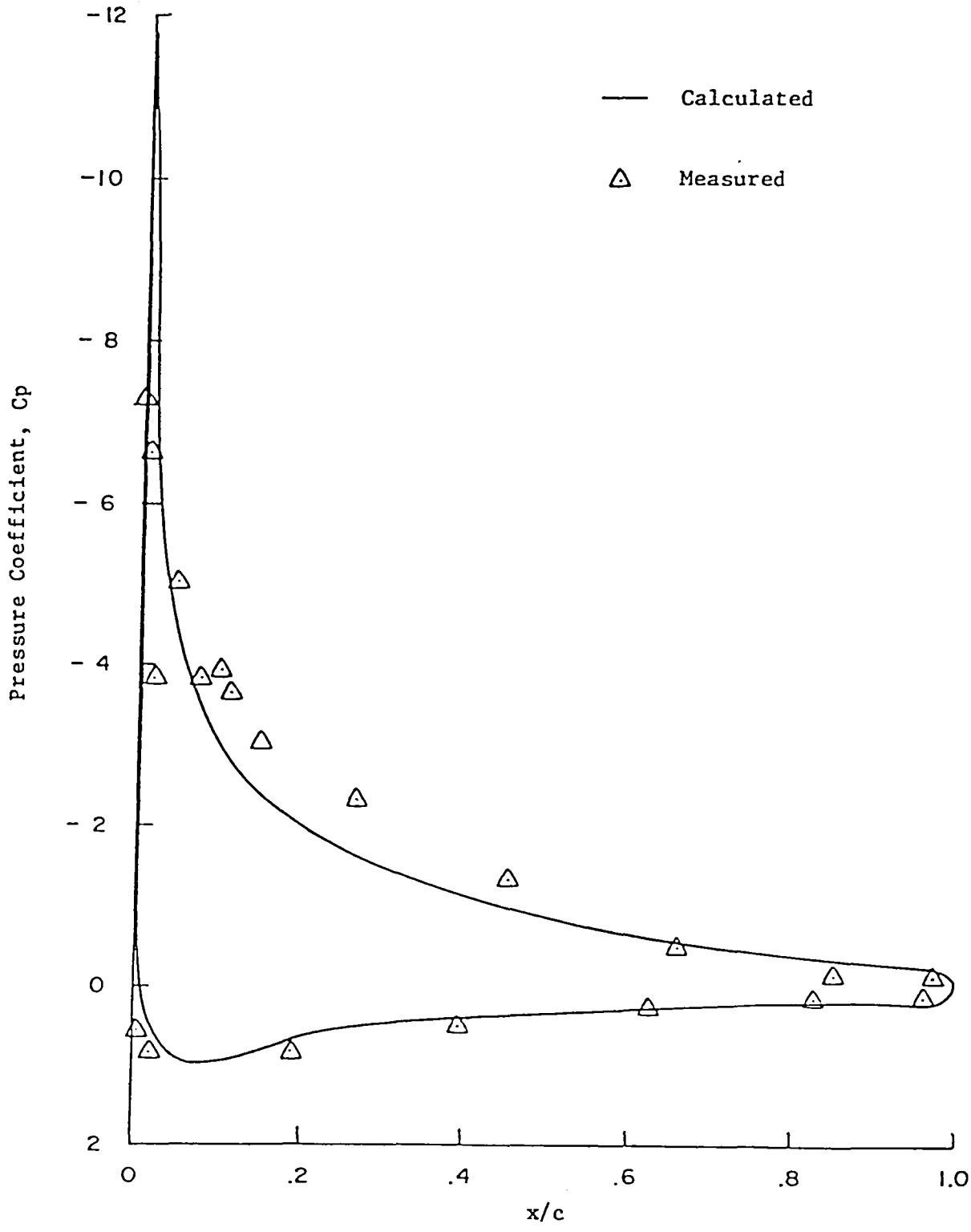

Figure 45 - Pressure coefficient comparison - NACA 0012 airfoil. $\alpha = 17.7°$, $\dot{\alpha} > 0$

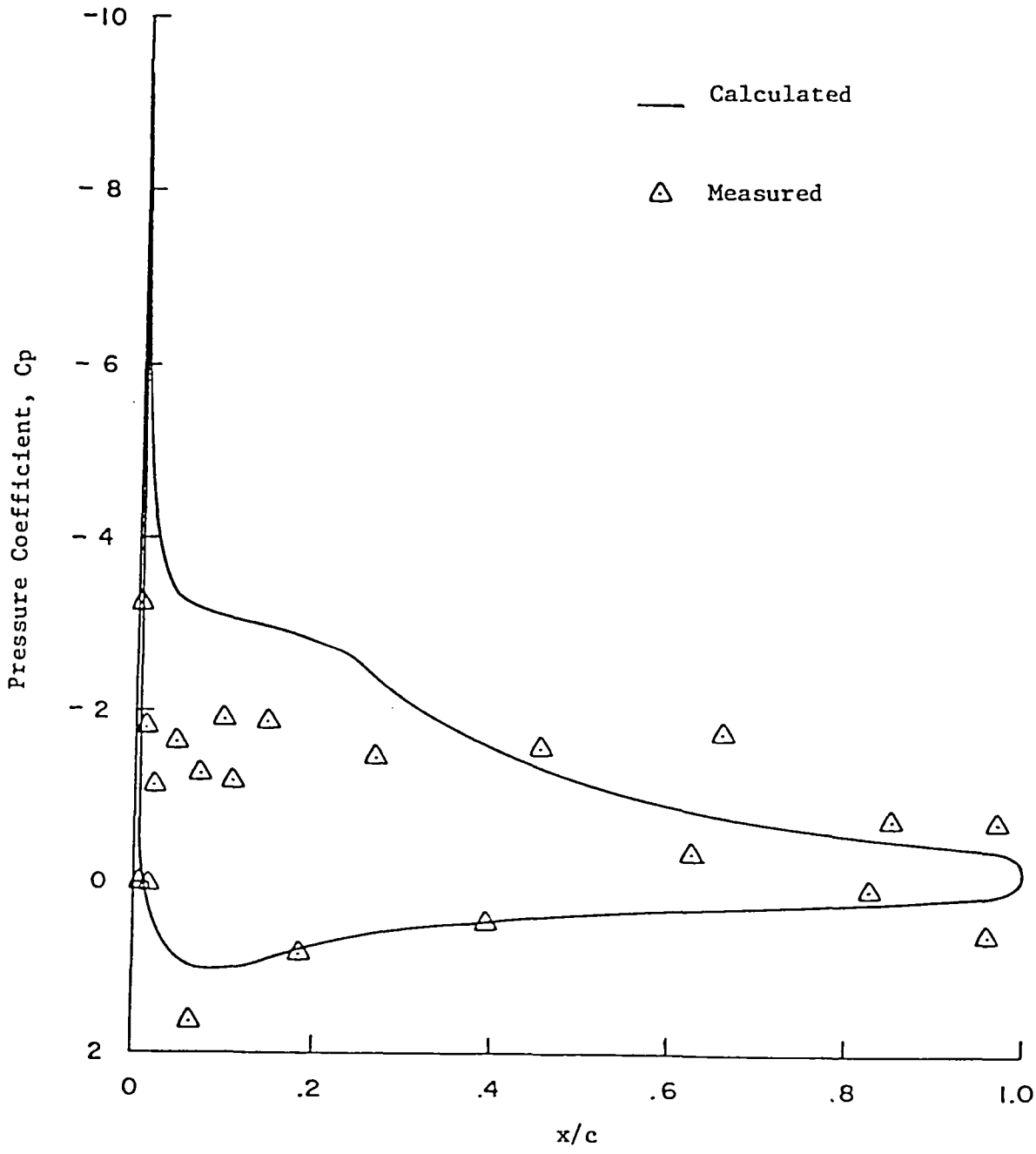

Figure 46 - Pressure coefficient comparison - NACA 0012 airfoil. $\alpha = 19.5°$, $\dot{\alpha} > 0$

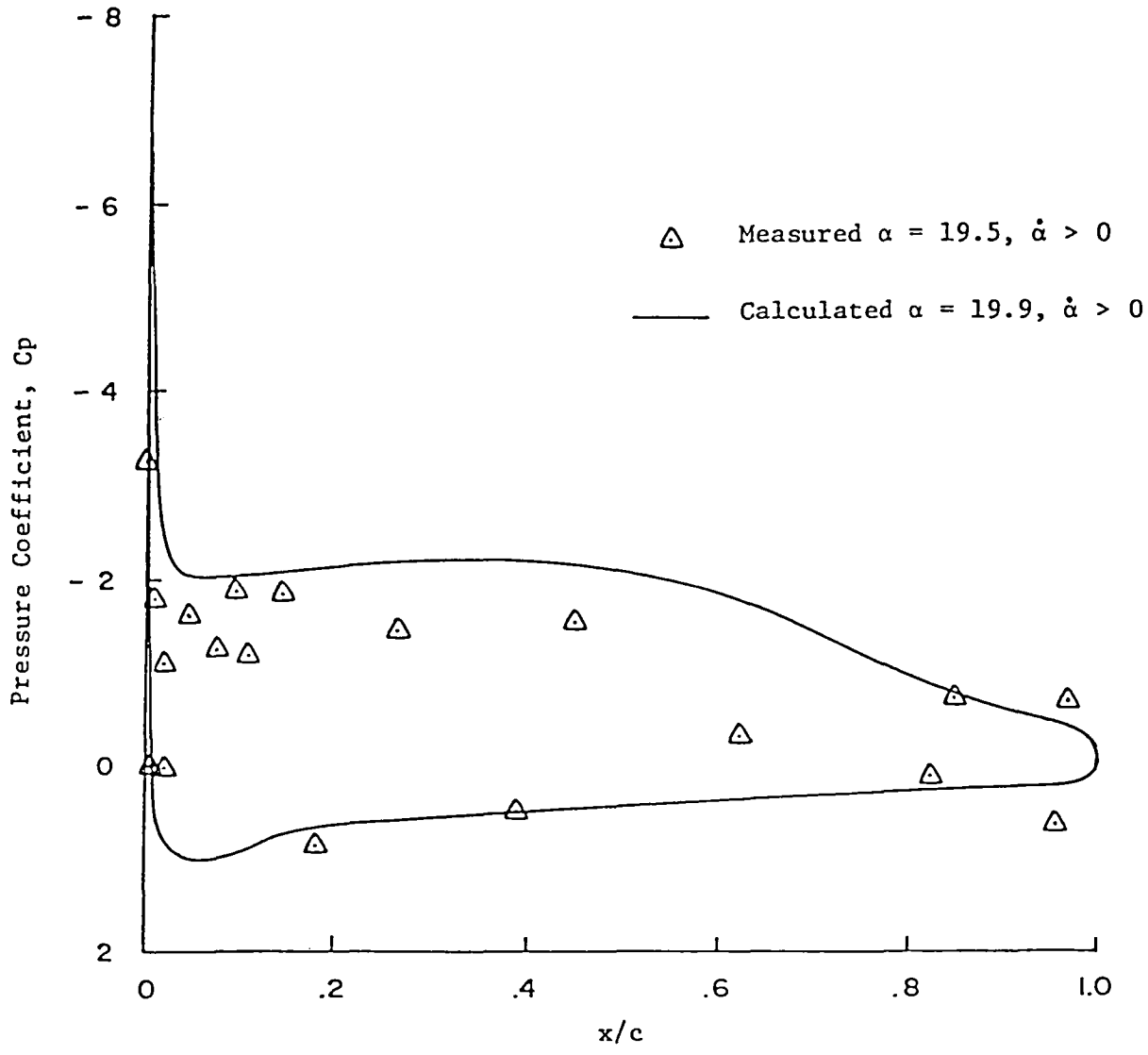

Figure 47 - Pressure coefficient comparisons - NACA 0012 airfoil.

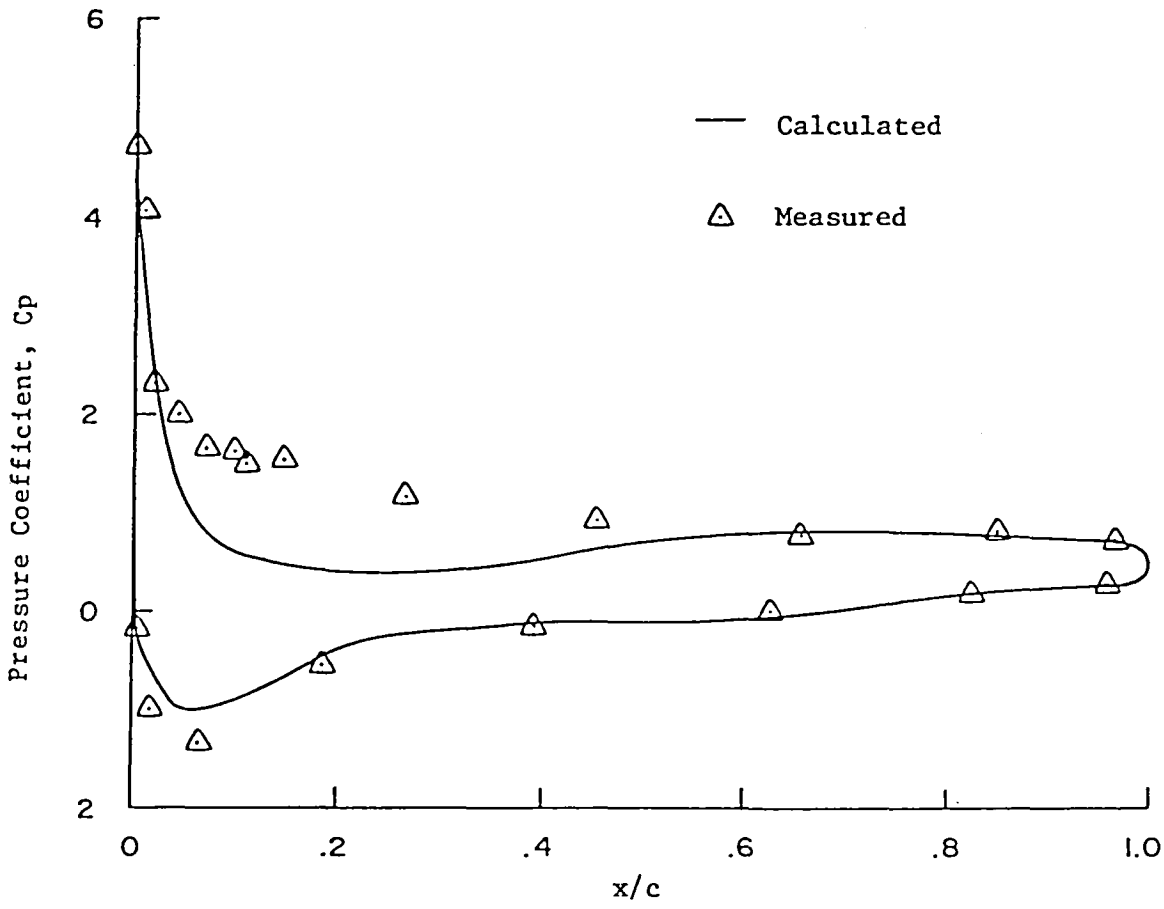

Figure 48 - Pressure coefficient comparison - NACA 0012 airfoil. $\alpha = 18.3°$, $\dot{\alpha} < 0$

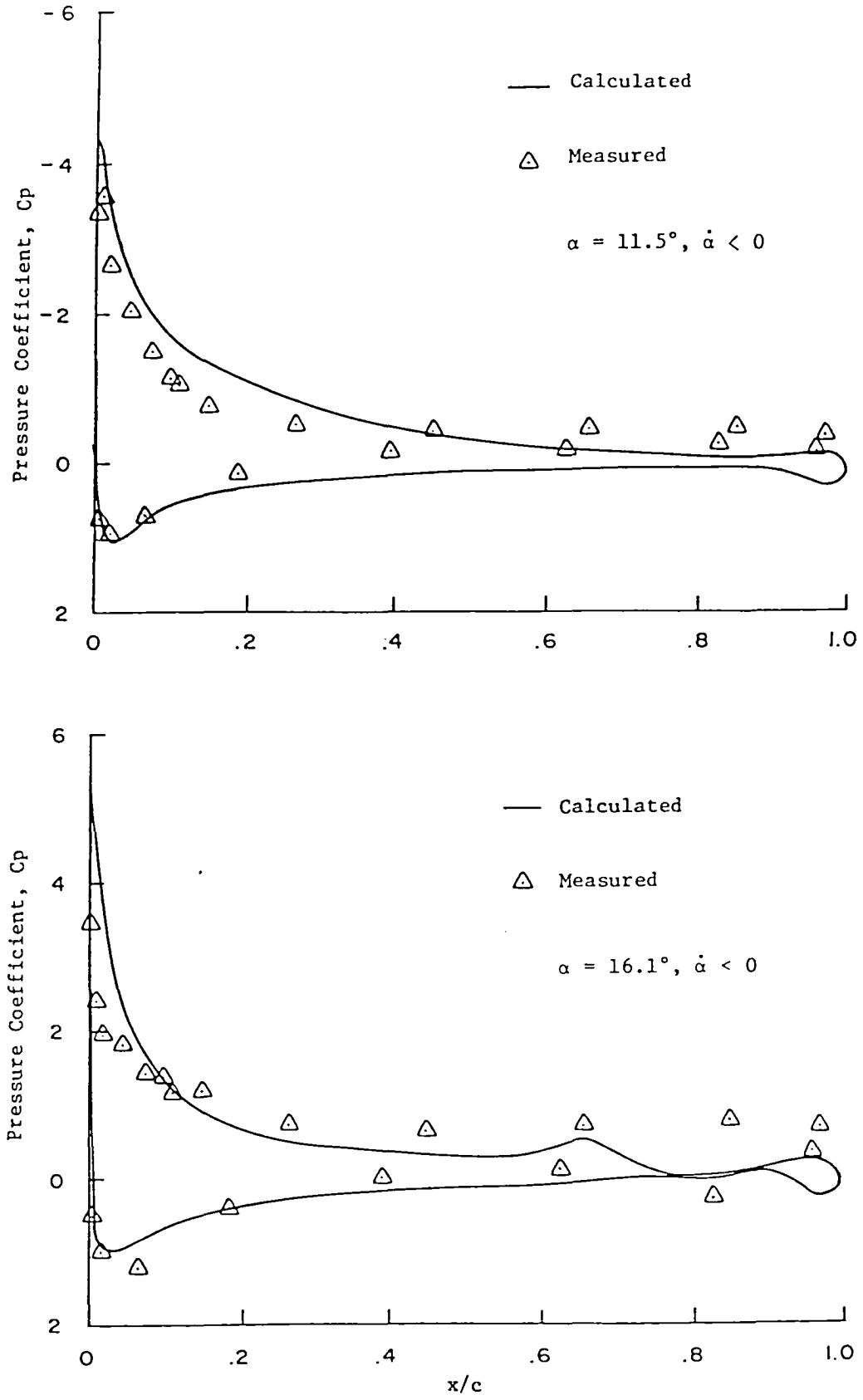

Figure 49 - Pressure coefficient comparison - NACA 0012 airfoil.

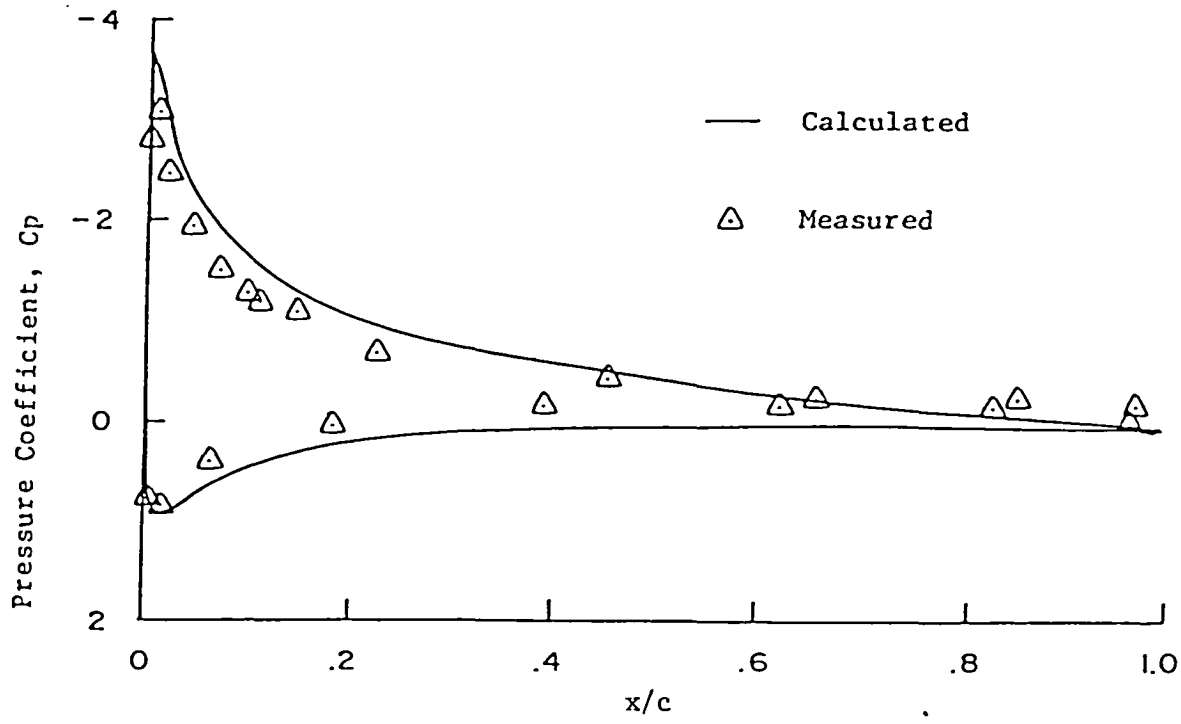

Figure 50 - Pressure coefficient comparison - NACA 0012 airfoil. $\alpha = 8.5°$, $\dot{\alpha} < 0$

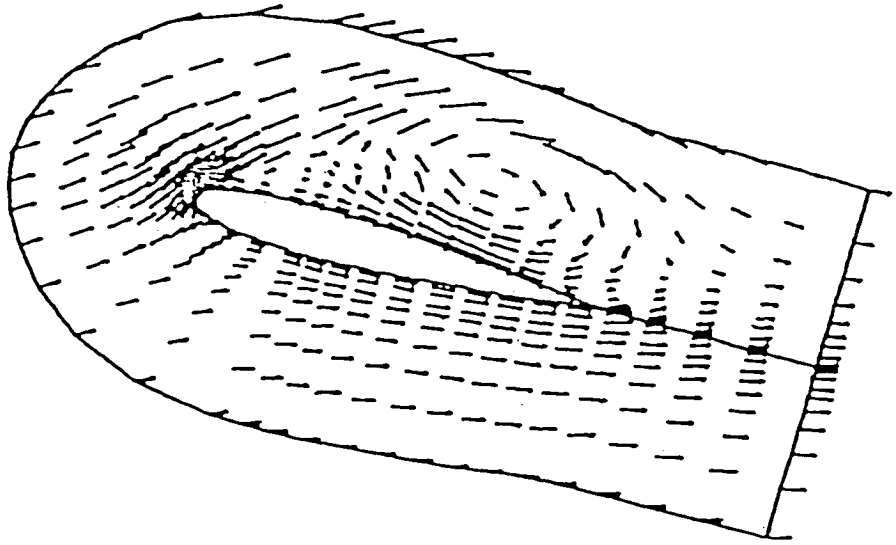

$\alpha = 19.9°, \dot{\alpha} > 0$

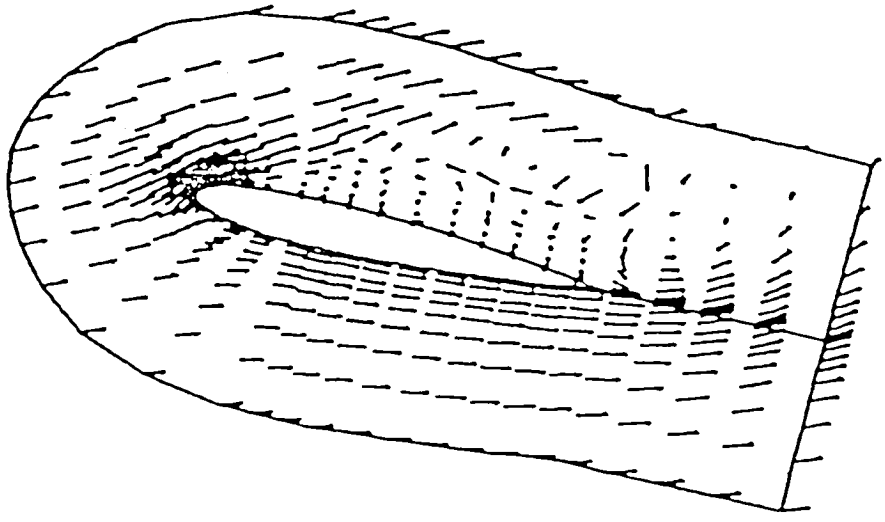

$\alpha = 18.3°, \dot{\alpha} < 0$

Figure 51 - Velocity vector plot - NACA 0012 airfoil.

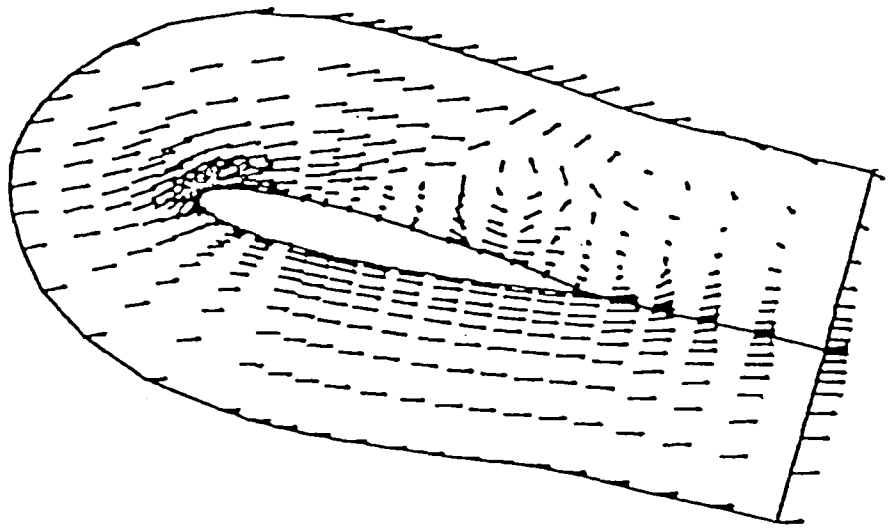

$\alpha = 16.5°, \dot{\alpha} < 0$

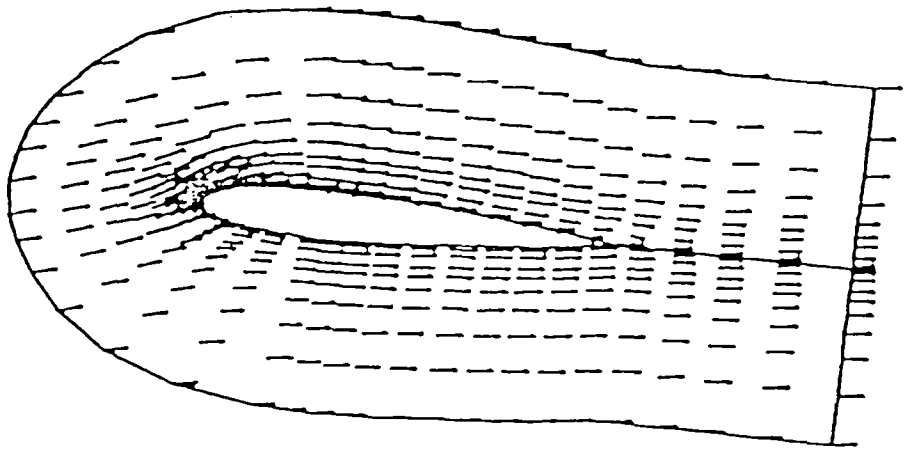

$\alpha = 9.5°, \dot{\alpha} < 0$

Figure 52 - Velocity vector plot - NACA 0012 airfoil.

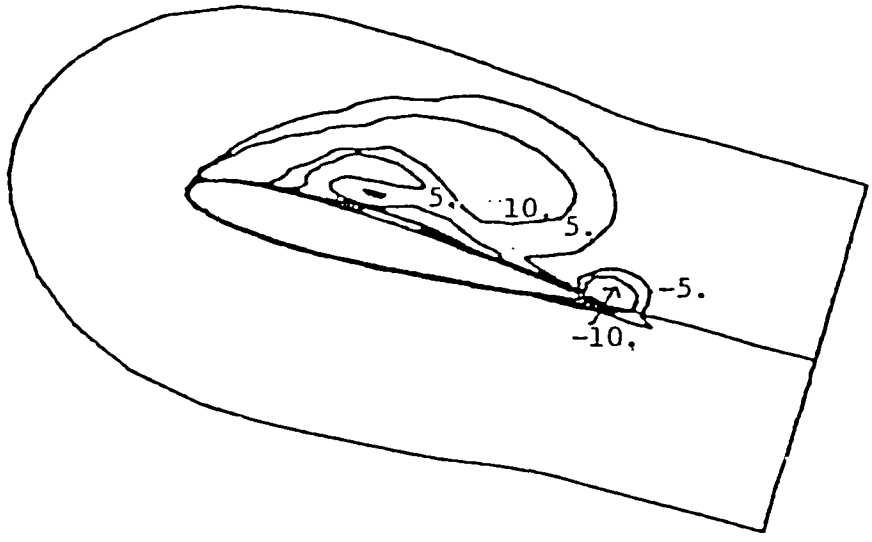

$\alpha = 19.9°$, $\dot{\alpha} > 0$

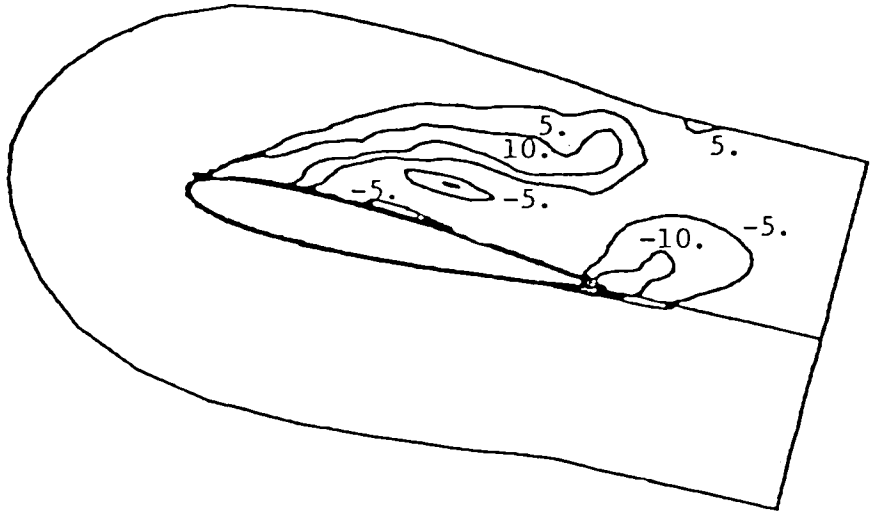

$\alpha = 18.3°$, $\dot{\alpha} < 0$

Figure 53 - Vorticity contours - NACA 0012 airfoil.

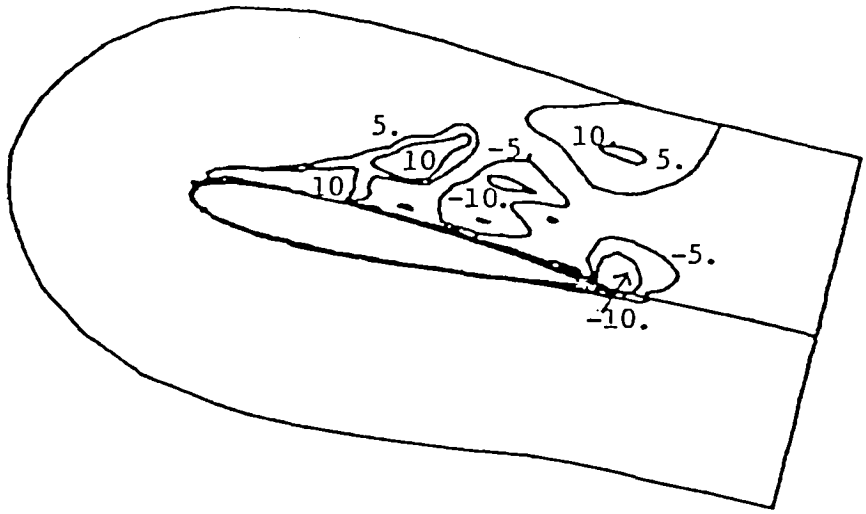

$\alpha = 16.5°, \dot{\alpha} < 0$

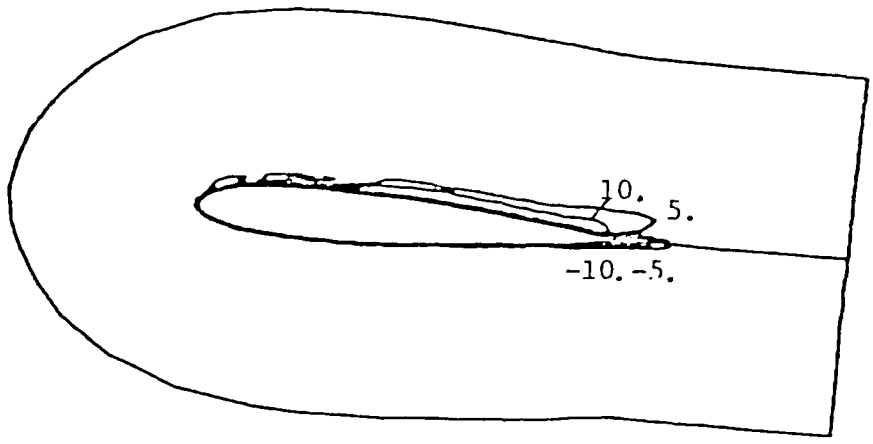

$\alpha = 9.5°, \dot{\alpha} < 0$

Figure 54 - Vorticity contours - NACA 0012 airfoil.

1. Report No.	2. Government Accession No.	3. Recipient's Catalog No.
NASA CR-3899		

4. Title and Subtitle	5. Report Date
CALCULATION OF STEADY AND UNSTEADY AIRFOIL FLOW FIELDS VIA THE NAVIER-STOKES EQUATIONS	August 1985
	6. Performing Organization Code
7. Author(s)	8. Performing Organization Report No.
Stephen J. Shamroth	
9. Performing Organization Name and Address	10. Work Unit No.
Scientific Research Associates, Inc. P.O. Box 498 Glastonbury, Connecticut 06033	11. Contract or Grant No. NAS1-15214
12. Sponsoring Agency Name and Address	13. Type of Report and Period Covered
NASA Langley Research Center Hampton, VA 23665	Contractor Report
	14. Sponsoring Agency Code 505-33-43-09

15. Supplementary Notes

Langley Technical Monitor: James T. Howlett
Final Report

16. Abstract

A compressible time-dependent procedure for the two-dimensional ensemble-averaged Navier-Stokes equations has been applied to the isolated airfoil problem in steady and unsteady flows. The procedure solves the governing equations via the linearized block implicit technique. Turbulence is modeled either via a mixing length or turbulence energy approach. The equations are solved in general non-orthogonal form with no-slip boundary conditions applied at the airfoil surface. Results are presented for airfoils at constant incidence, an airfoil in ramp motion and an airfoil oscillating through a dynamic stall loop. In general, steady converged solutions are obtained within 70 time steps over the range of Mach numbers considered, $0.01 \leq M_\infty \leq 0.5$. Comparisons with measured data show good agreement between computation and measurement.

17. Key Words (Suggested by Author(s))	18. Distribution Statement
Navier Stokes Airfoil analyses Dynamic stall Unsteady flow	Unclassified - Unlimited Subject Category 02

19. Security Classif. (of this report)	20. Security Classif. (of this page)	21. No. of Pages	22. Price
Unclassified	Unclassified	110	A06

For sale by the National Technical Information Service, Springfield, Virginia 22161 NASA-Langley, 1985

National Aeronautics and
Space Administration

Washington, D.C.
20546

BULK RATE
POSTAGE & FEES PAID
NASA Washington, DC
Permit No. G-27